



**BRNO UNIVERSITY OF TECHNOLOGY**

VYSOKÉ UČENÍ TECHNICKÉ V BRNĚ

**FACULTY OF MECHANICAL ENGINEERING**

FAKULTA STROJNÍHO INŽENÝRSTVÍ

**INSTITUTE OF PHYSICAL ENGINEERING**

ÚSTAV FYZIKÁLNÍHO INŽENÝRSTVÍ

**DYNAMICS OF MICROPARTICLES OPTICALLY  
TRAPPED IN VACUUM**

DYNAMIKA MIKROČÁSTIC ZACHYCENÝCH V OPTICKÉ PASTI VE VAKUU

**DOCTORAL THESIS**

DIZERTAČNÍ PRÁCE

**AUTHOR**

AUTOR PRÁCE

**Mgr. Vojtěch Svak**

**ADVISOR**

VEDOUCÍ PRÁCE

**Mgr. Oto Brzobohatý, Ph.D.**

**BRNO 2021**



## ABSTRACT

A microparticle levitating in vacuum only by optical forces constitutes a mechanical system which is extremely well isolated from its environment, including its sources of noise. This unique feature provides the system with outstanding sensitivity on any change of surrounding conditions. We introduce a unique experimental set-up for trapping in vacuum which we built at the Institute of scientific instruments of CAS in Brno. Subsequently we provide an experimental study of mechanical effect of circularly polarized light which, contrary to linearly polarized light, generates non-conservative contribution to the optical force field. We follow by presenting observation of optical binding of two particles in free space in vacuum which has never been realised before and show how the inter-particle interaction can be tuned and characterized. In the end we introduce a promising method for optical force field estimation based on particles stochastic trajectory analysis.

## KEYWORDS

optical trapping, optical levitation, counter-propagating beams, laser induced desorption, optical catapult, optical spin, non-conservative force, optical binding, force field estimation

## ABSTRAKT

Mikročástice levitující ve vakuu pouze za pomoci silových účinků světla představuje mechanický systém, který je extrémně dobře izolován od okolních a jeho zdrojů šumu. Tato unikátní vlastnost poskytuje tomuto systému nevídanou citlivost na změny okolních podmínek. V předkládané práci je popsáno technické řešení experimentální sestavy pro optické chytání ve vakuu, která byla realizována v laboratořích skupiny levitační fotoniky Ústavu přístrojové techniky AVČR v Brně. Dále je prezentována experimentální studie dynamiky částice zachycené v kruhově polarizovaném optickém poli, které generuje nekonzervativní složku pole optické síly. Následuje experimentální pozorování a popis dynamiky dvou opticky vázaných mikročástic ve volném prostoru ve vakuu, což je konfigurace, která nebyla nikdy předtím realizována. Závěrem je představena zcela originální metoda pro odhad silového pole optické pasti založená na analýze stochastické trajektorie zachycené částice.

## KLÍČOVÁ SLOVA

optické chytání, optická levitace, protiběžné svazky, laserem indukovaná desorpce, optický katapult, optický spin, nekonzervativní síla, optická vazba, odhad silového pole

SVAK, Vojtěch. *Dynamics of microparticles optically trapped in vacuum*. Brno, 2021, 85 p. Doctoral thesis. Brno University of Technology, Faculty of Mechanical Engineering, Institute of Physical Engineering. Advised by Mgr. Oto Brzobohatý, Ph.D.



## DECLARATION

I declare that I have written the Doctoral Thesis titled “Dynamics of microparticles optically trapped in vacuum” independently, under the guidance of the advisor and using exclusively the technical references and other sources of information cited in the thesis and listed in the comprehensive bibliography at the end of the thesis.

As the author I furthermore declare that, with respect to the creation of this Doctoral Thesis, I have not infringed any copyright or violated anyone’s personal and/or ownership rights. In this context, I am fully aware of the consequences of breaking Regulation § 11 of the Copyright Act No. 121/2000 Coll. of the Czech Republic, as amended, and of any breach of rights related to intellectual property or introduced within amendments to relevant Acts such as the Intellectual Property Act or the Criminal Code, Act No. 40/2009 Coll., Section 2, Head VI, Part 4.

Brno .....

.....

author’s signature



## ACKNOWLEDGEMENT

I thank my supervisor, Oto Brzobohatý, for his guidance and patience during my studies. He was always there to share his experience and his endless positivity. I thank prof. Pavel Zemánek, who is the most supportive chief. I also thank Stephen Simpson, who was an inexhaustible well of inspiring ideas and who patiently corrected my English and mz math every time I asked him. Finally I thank all Microphotonics team members for their open and helpful attitude.

*The research was supported by the Centre of Excellence for Classical and Quantum Interactions in Nanoworld (GB14-36681G) and ALISI - Centre of Advanced Diagnostic Methods and Technologies (LO1212).*

Brno .....

.....

author's signature





# Contents

<b>1</b>	<b>Introduction</b>	<b>1</b>
<b>2</b>	<b>Experimental set-up</b>	<b>5</b>
2.1	Optical forces . . . . .	5
2.2	Optical set-up . . . . .	7
2.3	Particle tracking . . . . .	9
2.3.1	Split detection by quadrant photo-diode . . . . .	9
2.3.2	Videomicroscopy . . . . .	10
2.4	Particle loading . . . . .	12
2.4.1	Nebulisation . . . . .	12
2.4.2	Laser induced acoustic desorption . . . . .	13
2.5	Vacuum system . . . . .	14
<b>3</b>	<b>Transverse spin forces and non-equilibrium particle dynamics in a circularly polarized vacuum optical trap</b>	<b>17</b>
3.1	Optical Momentum and forces . . . . .	18
3.1.1	Optical momentum . . . . .	18
3.1.2	Optical forces - small particle approximation . . . . .	19
<b>4</b>	<b>Optical binding of microparticles in vacuum</b>	<b>29</b>
4.1	Stochastic dynamics of optically bound matter levitated in vacuum .	29
4.2	Experimental observation of vacuum optical binding of multiple particles . . . . .	41
<b>5</b>	<b>Force estimation from stochastic trajectory</b>	<b>43</b>
5.1	Estimation procedure . . . . .	44
5.2	Conservative force field - 1D case . . . . .	48
5.3	Non-conservative force field - 2D case . . . . .	52
5.4	Distortion of the estimated force caused by additive noise in position measurement . . . . .	56
5.5	Summary . . . . .	68
<b>6</b>	<b>Conclusion</b>	<b>69</b>
	<b>List of acronyms</b>	<b>71</b>
	<b>Bibliography</b>	<b>72</b>
	<b>Publications and other outputs</b>	<b>83</b>



# 1 Introduction

In 1970, Arthur Ashkin published seminal paper showing that it is possible to accelerate and grab micron-sized transparent particles by focused laser beam [1]. Since then, the field of optical micro-manipulation underwent vast development [2]. Optical trapping techniques played important role in research across physical, chemical and biological sciences with applications starting at manipulation with atoms and micro-particles leading to manipulation of living cells [3] or such demanding experiments as measurement of tiny forces between single molecules in various molecular motors [4, 5].

The mostly used optical tool, *optical tweezers* [6], is created by a laser beam tightly focused by a high numerical aperture microscope objective. Such tool, referred to as an optical trap, is capable of trapping and manipulating a single object of size ranging from tens of nanometers to tens of micrometers. Trapping several such objects can be achieved by splitting the original laser beam into several beams by phase grating generated by spatial light modulator (SLM) [7] or by amplitude grating generated by digital micro mirror device (DMD), obtaining so called *holographic optical tweezers*. Another approach to create multiple traps is *time-sharing trapping* [8], where the trapping laser beam is being switched between individual traps so fast that the particles do not have enough time to escape due to Brownian motion. Such speeds are achieved using galvano-optical mirrors or acousto-optic deflectors (AODs). Holographic optical tweezers is the most flexible and all-purpose method for trapping several tens of objects enabling to trap in 3D and even to shape the trapping potential of individual trap. The universality is counterbalanced by several limiting factors, mainly by low trapping efficiency and slow modification of the trapping potential (tens of Hz) compared to time-sharing.

Extensive systems of optical traps can be fabricated by an interference of several laser beams, when each local intensity maximum/minimum constitutes a possible optical trap. Possibility of creating two-dimensional structures of traps on surface via interference field of co-propagating beams was reported [9, 10, 11]. Three-dimensional structure of traps was realised in the standing wave formed by interference of two counter-propagating beams [12, 13, 14, 15]. Notably the magnitude and even the direction of force acting on a particle placed in such structure is very sensitive on the particle size which is elegantly exploited in various techniques of *optical sorting* [16, 17, 18].

All of the experiments listed above manipulates with objects in liquid. Liquid media strongly damp the motion of trapped objects to become overdamped, and the particle inertia does not play any role in observed particle dynamics. Such damping improves the trap stability and makes trapping in liquid relatively straight-

forward. In contrast, trapping particles in low viscosity environment (e.g. air, low pressure) is more challenging, because mechanical noise of the set-up or relative intensity noise of the trapping laser affect the trapping stability. In his pioneering experiments regarding trapping in air [19], A. Ashkin used inverted geometry of optical tweezers [20, 21, 22]. Here, the gravitational force acting on the particle is compensated by radiation pressure of the upward propagating trapping beam. Such a geometry was used for investigation of properties of dust particles, for example size, composition, morphology and phase [23, 24, 25]. Another geometry, which does not employ external force for particle containment, uses two counter-propagating Gaussian beams. It was used for trapping of solid airborne particles [26, 27], study of ice formation [28], for trapping of salt and sugar crystal from solution [29] and for study of optical interaction between several oil droplets in the air [30].

Single particle held in an optical trap behaves as a mechanical oscillator. If it is placed in vacuum, it becomes isolated from the external environment possible which results in very low mechanical damping and high mechanical quality factors of such oscillator. This unique property attracted a lot of attention during the last decades. Researchers thoroughly studied the center-of-mass (CoM) motion of particle trapped in various trap geometries and showed methods how to control it [31, 32, 33]. Extracting energy from the CoM mode and reaching quantum ground state has become one of the main challenges in the field. This so-called *cooling* was successfully implemented [34, 35]. Quantum ground state cooling was reported using already two techniques, the first one being the passive technique using coherent scattering into an optical resonator [36], the second one used active feedback cooling [37]. Further more, librational motion [38], rotation [39, 40] and nonlinear dynamics [41, 42] of this optomechanical system are started to be examined in detail. The ultimate goal of all these studies is to engineer a platform suitable for studying the border between classical and quantum mechanics [43, 44, 45]. Another fascinating area of use is ultra-sensitive force (zeptonewton range,  $10^{-18}$  N) and torque ( $10^{-25}$  Nm range) measurement [46, 47].

The primary goal of my work was to design and develop an experimental apparatus for optical trapping in vacuum based on counter-propagating beams geometry. The essential parts of the developed experimental set-up are described in Chapter 2.

The ability to design and dynamically change the optical forces or to control the stochastic forces opened experimental ways to test fluctuation theorems [48], test information thermodynamics [49] or realize compression stages of heat engines [50]. I utilised the set-up to carry out an experiment studying the mechanical effect of polarisation dependent optical force on a trapped particle. The experiment, which was theoretically proposed by my colleague Stephen Simpson, is presented in

Chapter 3. It shows, compared to the linearly polarised case, that the circularly polarised light generates additional component of the total force on the particle which points in direction perpendicular to the light propagation and is proportional to the trapping power. Although this component is small, it drives the particle out of thermal equilibrium and it can even lead to ejection of the particle from the trap. We believe such optical traps using circularly polarized light are promising testbed for non/equilibrium statistical mechanics.

The ability of our set-up to levitate several particles simultaneously was also exploited. Those particles are coupled via optical forces which is known as *optical binding* [51]. This phenomenon is well examined in overdamped systems using water as ambient medium. On the other hand, the optical binding in vacuum is virtually unexplored and of growing interest due to possible link to quantum entanglement of 'macroscopic' objects [52]. Chapter 4 summarizes experimental observation of dynamics of several optically bound particles trapped in vacuum. Extra attention is paid to the simple case of two bound particles for which we identify normal modes, show the tunability of the interparticle separation and quantify the nonlinear interparticle coupling for various separations.

In Chapter 5 an universal method is introduced, which estimates the optical trap force field exerted on the particle only by evaluating the particles stochastic trajectory. It utilizes a binning approach to calculate local mean velocity and acceleration and it is applicable for arbitrary force field, conservative or non-conservative. The performance of the method is demonstrated on both numerical simulations of stochastic trajectories and experimental data.

I contribution to the presented results mainly by experimental activity. I designed and aligned the experimental setup used in Chapter 3 and part of Chapter 4, including control software development. I performed majority of the experiments and part of the data processing. I was closely involved in discussions on the obtained results. I developed the estimation method presented in Chapter 5 practically on my own. The detailed overview of my contributions is summarized at the end of the thesis.



## 2 Experimental set-up

Compared to frequently used optical traps in water, stable and reliable trapping in low pressure is much more technologically demanding. In water the motion of the optically trapped bead is damped intensively by the surrounding medium. The trapped bead's motion is overdamped, the bead's inertia doesn't play a role and the trap is unlikely to be destabilized by mechanical instability or intensity noise of the trapping beam. The processes of interest are slow enough to be observed by common cameras and of-the-shelf quadrant detectors. The objects to be trapped float freely in the medium and can be trapped by moving the sample stage in the right direction. When the trapped object leaves the trap it is floating nearby the trapping location and can be easily trapped again. None of this is true for trapping in air and low pressure. For vacuum traps few of the traditional techniques can be used and novel techniques of trap design, alignment, sample loading and detection have to be developed. Since the development of the experimental set-up was the main goal of my PhD activity, it is presented in detail in the following paragraphs.

### 2.1 Optical forces

The forces exerted on a particle originate from momentum change of the photons scattered on it. The force acting on a particle located inside a single laser beam is traditionally decomposed into two components - the *gradient force* and the *scattering force*. This custom originates in the Rayleigh approximation of scattering [53, 54], which is used for description of optical forces acting on a particle, which is much smaller than the wavelength of trapping light and which can be described as an induced dipole. The scattering force, commonly known as radiation pressure force, acts in the direction of propagation of light and it pushes the particle out of trap. The gradient force is directed towards the region of highest intensity, provided the particle's refractive index ( $n_{particle}$ ) is higher than that of surrounding medium ( $n_{medium}$ ), and it pulls the particle back to the trap.

Geometric optics can be employed to get an intuition for the origin of the gradient force. Light is treated as a collection of rays which are refracted and reflected on the interface of the particle and the surrounding medium (see Fig. 2.1a). The photons following light ray A are refracted downwards, their direction of propagation is changed, meaning their momentum is changed also. According to Newton's second law of motion, this change in momentum is caused by a force acting on the photons and this force is generated by the material of the particle. According to the Newton's third law, if the particle exerts a force on the photons, the photons exert force on the particle and this force has the same magnitude and opposite direction. So the

refracted photons generate force  $\mathbf{F}_A$  pushing the particle upwards. Similarly light ray B is refracted upwards and generates force  $\mathbf{F}_B$  downwards. Since the intensity of A exceeds the intensity of B, the net force acting on the particle points upwards and the particle is drawn to the region of higher intensity - to the beam axis.

The particle, however, is also propelled forward, partly due to the reflection of light on the particle. In order to compensate for this destabilising force component and achieve stable confinement, A. Ashkin used two mildly focused counter-propagating beams in his first experiments [1]. Later he introduced the *levitation trap*, where the scattering force was counter-acted by gravitational force [55]. The most popular 3D trap uses one tightly focused beam forming so called *optical tweezers* [56]. Such single beam trap is depicted in Fig. 2.1b). The particle is displaced along the optical axes to the right from the focus. Rays C and D are refracted such that they propagate to the right in a more horizontal direction, generating restoring forces  $\mathbf{F}_C$  and  $\mathbf{F}_D$  on the particle pointing to the left towards the focus.

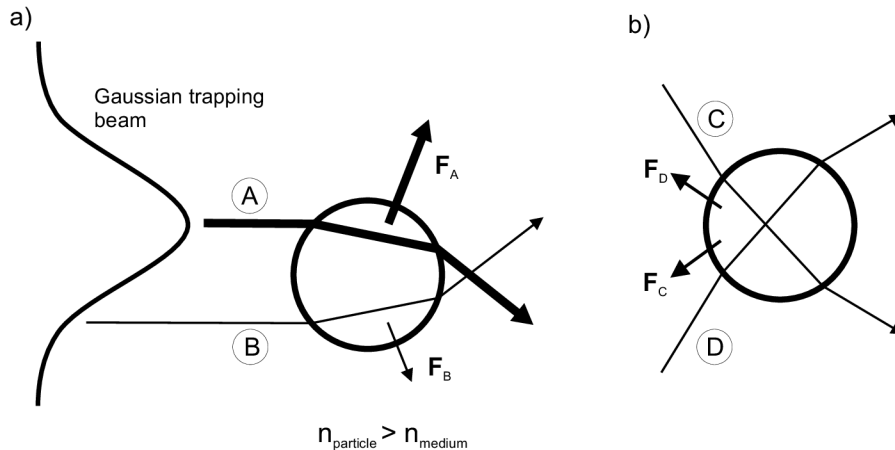


Fig. 2.1: Origin of optical forces using a geometric optics description (see details in the text).

We decided to employ the counter-propagating geometry because of its universality, which gives the opportunity to perform wide range of experiments. In this geometry of beams the axial scattering forces from both beams cancel and only gradient force remains [57]. This configuration, also known as *dual beam* (DB) optical trap, uses two laser beams, which are coaxial, but propagate in opposite directions. To form a trap, the beams are mildly focused (typically  $NA > 0.5$ ) and their foci are overlapped (see Fig. 2.2a,b)). Among the main advantages of DB belong the possibility to trap several objects or observation of trapped object perpendicularly to the beam axes.

Ashkin's original design of DB trap [1] did not employ interference of the counter-propagating beams and thus only one trap was generated (Fig. 2.2a)). When



coherent and interfering light is used, standing wave is created (Fig. 2.2b)), which generates an axial array of many optical traps [12]. With respect to their sub-wavelength dimension, these traps are ideal for trapping of nanoparticles [58, 59, 60] and their transport by so-called *optical conveyor belt* [14, 61, 62]. Fig. 2.2c) shows an image of a microparticle trapped in DB vacuum optical trap I built in labs of the Institute of Scientific Instruments of the CAS in Brno.

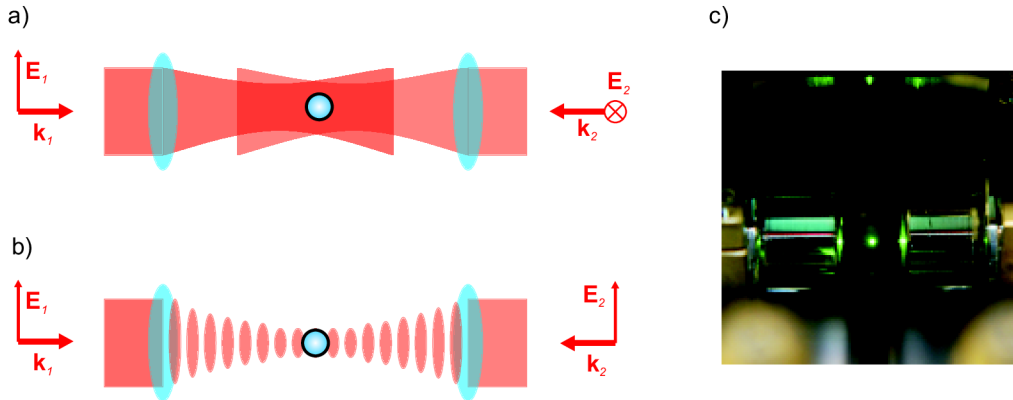


Fig. 2.2: Dual beam optical trap; (a) two counter-propagating beams with perpendicular linear polarisations do not interfere and one trap is created; (b) two counter-propagating beams with parallel polarisations interfere creating standing wave and array of traps; (c) a microparticle trapped DB optical trap in vacuum.

## 2.2 Optical set-up

A schematic of our experimental set-up is provided in Figure (2.3). The low noise laser beam from a Prometheus laser (Coherent) emitting at wavelength of 1064 nm passes, first, through a polarizing beamsplitter PBS1 (Thorlabs PBS203) and then is coupled to a single mode optical fiber (SMOF, SQS 980 HP) for spatial filtering. The trapping power is controlled by rotation of the half-wave plate, PP1 (Thorlabs WPQ05M-1064), in front of PBS1. The output of the SMOF is divided into two beams of equal power and orthogonal linear polarization (LP) by polarizing beamsplitter PBS2 (Thorlabs PBS203). Lenses L3 (AC254-200-A) and L4 (AC254-200-C) constitute a 1/1 beam expander with focus located on dielectric mirror M1 (Thorlabs NB1-K13). For dual beam traps precise overlap of the foci of the counter-propagating beams is critical. Inspection and correction of the overlap inside vacuum chamber is generally complicated and time-consuming procedure. Involving beam expander enables us to assure good foci overlap and compensate mechanical drifts very efficiently. If the expander is adjusted correctly the focal plane of the trap

inside the chamber is conjugated with the mirror M1 plane. This means that good overlap of beams in the M1 plain implies good overlap in the trap plain. Because the mirror surface is not absolutely perfect, it scatters a little portion of the light so the overlap of beams foci in M1 plane can be observed by camera C1 and eventually corrected by tilting the mirror DM1.

Before entering the vacuum chamber, the polarization of one of the beams can be changed from linear to right-hand or left-hand circular (CP) by a quarter-wave plate PP4 (Thorlabs WPQ10M-1064). The linear polarization of the second beam can be first rotated through an arbitrary angle by half-wave plate, PP2 (WPH10M-1064), and subsequently changed from linear to right-hand or left-hand circular polarization by the quarter-wave plate, PP3 (Thorlabs WPQ10M-1064). In the vacuum chamber, the counter-propagating beams are focused by aspheric lenses L1, L2 (Thorlabs C240TME-C) of focal length 8 mm to create a trap with a beam waist of  $w_0 \approx 2.7 \mu\text{m}$ .

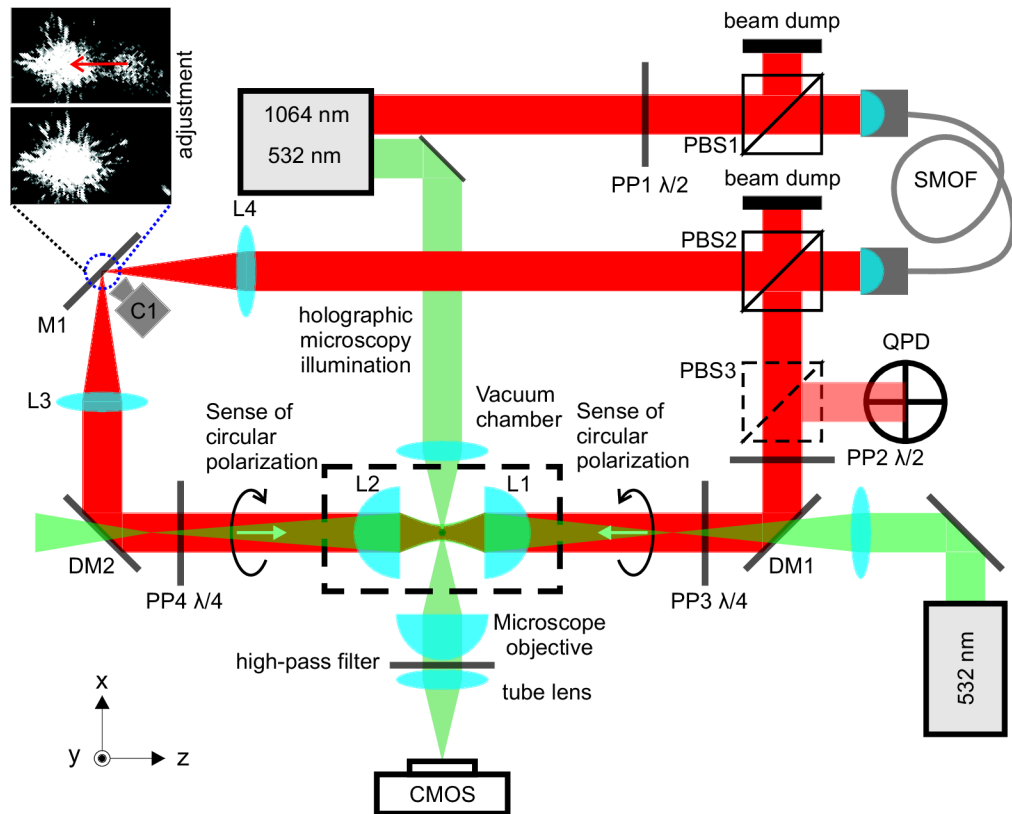


Fig. 2.3: Experimental arrangement.

## 2.3 Particle tracking

### 2.3.1 Split detection by quadrant photo-diode

We employed a detection scheme based on the back focal plane interferometry [63, 64, 65, 66]. A particle positioned in the trapping beam scatters a little portion of the trapping light. Both the scattered light and the unscattered trapping beam propagate towards quadrant photo-diode (QPD) plane, where they interfere. If the particle is not positioned in the centre of the trap, the interference intensity pattern is not centrally symmetric, as indicated in Fig. 2.4. The asymmetry of the intensity distribution encodes the particles position in the two lateral directions  $x$  and  $y$ , the total intensity encodes the axial position  $z$ . The positions voltage signals are generated from four separate quadrant signals  $Q_1 - Q_4$  according to the following equations:



$$x = \frac{(Q_2 + Q_3) - (Q_1 + Q_4)}{Q_1 + Q_2 + Q_3 + Q_4}$$

$$y = \frac{(Q_1 + Q_2) - (Q_3 + Q_4)}{Q_1 + Q_2 + Q_3 + Q_4}$$

$$z = Q_1 + Q_2 + Q_3 + Q_4$$

Fig. 2.4: QPD detection principle.

In our case, one of the trapping beams (red coloured beam in Fig. 2.3) is used for the tracking the particle position. After passing through the vacuum chamber the measuring beam is reflected by the polarizing beamsplitter PBS3 onto the QPD. Half-wave plate PP3 is used to control the intensity reflected onto the QPD to set optimal signal-to-noise ratio.

Since the typical oscillation frequencies of trapped nanoparticles range from 10 kHz to 150 kHz and for example the rotational frequencies of trapped nanowires are even several orders of magnitude higher, commercially available quadrant detectors with the detection bandwidth (BW) of about 100 kHz are not fast enough. The bandwidth of these devices is limited mainly by the electronics, not the photodiode itself. Quadrant photodiodes with bandwidths up to 120 MHz are available so with appropriate amplifying electronics the detection BW can be significantly enhanced. In collaboration with electrical engineers we developed a QPD detection unit based on InGaAs quadrant photodiode Hamamatsu G6849. The four current signals generated by the quadrants are amplified and analogically processed into  $x, y, z$  voltage signals by summation electronics according to scheme depicted in Fig. 2.4. This detector provides us with detection BW of approximately 1.5 MHz. The position

voltage signals are acquired by NI USB 6351 acquisition card at 400 kHz sampling rate. The 1.5 MHz BW is given by the summation electronics. With modern acquisition and signal processing devices it is possible to sample the four quadrant separately and calculate the coordinates in a digital manner with sampling rates up to several hundreds of MHz.

### 2.3.2 Videomicroscopy

The particle's motion is also tracked from outside the vacuum chamber by videomicroscopy using a fast CMOS camera (Vision Research Phantom V611) which can be triggered to start recording at the same time as the QPD. The position is not known in real time, it is obtained by postprocessing of the recorded video using in house developed MATLAB code. Employing videomicroscopy brings some significant advantages over the QPD approach. First, more than one particle can be tracked. If more particles are trapped, for example during optical binding experiments, the QPD signal is a mixture of two motions which cannot be separated. Second, the microscope can be easily calibrated by calibration grid so the dimensions in the image are well known. In contrast, the QPD signal is a voltage signal and the relation between voltage and displacement expressed in meters has to be established by sophisticated methods using parameters of the trapped particle, which are not always well known [67, 68].

We set up a microscope composed of a microscope objective (MOTIC, Plan Apo,  $100\times/0.55$ , WD 13), tube lens (Thorlabs ACA-254-500A) and a fast CMOS camera (Vision Research Phantom V611) capable of recording up to 700 000 frames per second. Long working distance of our objective (13 mm) enabled us to observe the particle motion from outside the vacuum chamber. Still it was necessary to manufacture a vacuum viewport allowing us to put the objective barrel close enough to the trap. We manufactured such viewport by welding a stainless steel tube onto a blank flange with a hole in it. On the other end of the tube there is a microscope slide glued on. The flange mounted on the vacuum chamber creates a tunnel leading to the trap in which the objective is inserted.

The most straight-forward way how to observe a trapped particle by such microscope is to record the scattered trapping light without any additional illumination. The position of the bright spot in the image (viz. Fig. 2.5a) can be evaluated with sub-pixel precision when the intensity distribution is fitted by 2D Gaussian function or its centre of mass (centroid) is calculated. Particle position can be found, naturally, only for the two observed dimensions. Unfortunately the achievable frame-rate of such recording is limited by both the amount of light scattered and sensitivity of camera on used trapping wavelength. The camera we use is designed for recording

scenes illuminated by white light and it is the most sensitive in the green spectral region, the sensitivity on near IR is nearly zero. Since we trap with 1064 nm laser, this way our frame-rate would be very limited. Thus we employed wide horizontal green laser beam (532 nm) with low intensity to not affect the motion of observed particles and we observed the green scattered light as depicted in Fig. 2.3.

We also employ the so called holographic microscopy technique, which in principle provides us with all three coordinates of the particle position and moreover with its radius and refractive index [69, 70, 71, 72]. The particle is illuminated by wide Gaussian beam and it scatters a little portion of the incident light. The scattered light propagates to the microscope objective focal plane where it interferes with the unscattered beam. The interference pattern is then imaged by the microscope onto the camera CMOS chip (viz. Fig. 2.5b). The obtained intensity distribution is then fitted with physical model of scattering with fitted parameters being the 3D position of the particle, its radius and refractive index.

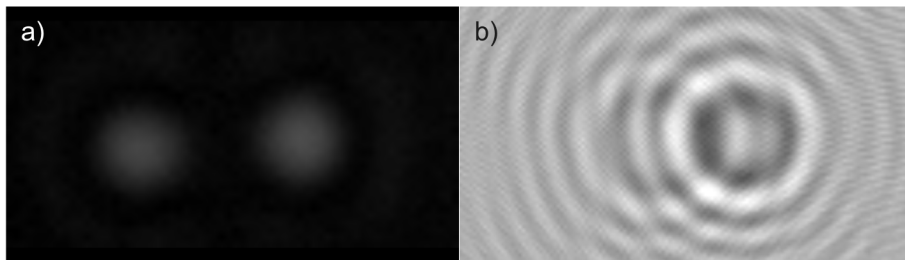


Fig. 2.5: Videomicroscopic observation of particles; (a) image of two trapped micro-particles using only scattered trapping light; (b) holographic image of two trapped micro-particles.

Holographic microscopy was successfully used for tracking particle motion in optical traps in water [69, 70, 71, 72], which are devices often based on commercial microscopes with well corrected optical aberrations. To our knowledge we are the first to implement holographic microscopy in vacuum set-up. It turns out that the vacuum viewport situated in the optical path between the focal plane and the objective is source of strong spherical aberration rendering the standard evaluation procedure useless. We tried to reduce the aberration by replacing our original 1 mm thick viewport with 150  $\mu\text{m}$  thick coverslip. After this adjustment we were still able to keep good vacuum conditions in the chamber, however, when the chamber is pumped down, the coverslip bends and corrupts the hologram even more. Nevertheless, we are still able to obtain particle position in 2D in common video-microscopic way by focusing on the particle. We are improving the theoretical model so that it take into account the spherical aberration in general.

## 2.4 Particle loading

Loading a particle into a vacuum optical trap presents a surprisingly non-trivial problem. In liquid the procedure is straight-forward. A tenuous suspension of beads in water is prepared and it is injected into the experimental chamber (glass capillary, sample on microscope slide). The particle moves around the trap in a Brownian manner. By moving the sample stage accordingly, a desired particle can be moved to close vicinity of the trap and trapped. When the particle is lost, it stays nearby and can be trapped once more. On the other hand, particles in air cannot be manipulated in controlled manner to load the trap and when lost they fall down due to gravitational force and cannot be recaptured again.

### 2.4.1 Nebulisation

We implemented two methods of loading the vacuum trap, both relying on the bead reaching the trapping volume by chance. The technologically less demanding method uses an ultrasonic nebuliser. An ultrasonic nebuliser is a medical device which creates a spray of little droplets of a medicament which is then inhaled by a patient. It essentially consists of thin polymer mesh mount on the top of a piezoelectric ring. Suspension of beads in isopropyl alcohol (IPA) is put on one side of the mesh. When the nebuliser is turned on, the piezoelectric ring starts to oscillate thus pushing the suspension through the mesh and creating little droplets on the other side. The typical diameter of a droplet is  $< 10 \mu\text{m}$  and the concentration of the suspension is such, that there is one or zero particle on average. Under standard atmospheric conditions the IPA evaporates quickly and a individual bead in air remains.

We use the commercial nebuliser Beurer IH50 which generates quite fast stream of droplets with inconveniently big spatial spread. Particles sprayed this way are too fast to be trapped and generally too far from the trap. In order to slow the droplets down and focus them near the trapping region we first generate a mist of droplets in a glass nozzle ended with a small opening (see Fig. 2.6a)). Then the droplets are pushed out slowly from the nozzle into the trap by air pumped into the nozzle by peristaltic pump. This way we get a dense stream of droplets falling slowly into the optical trap (Fig. 2.6c)) enabling us reliable loading of either single particle or chain of particles for optical binding experiments. The disadvantage of this method is the necessity of loading under air pressure and pumping down to target pressure afterwards. During initial phase of pumping the particles tend to be kicked out of the trap by airflow in the chamber which needs to be prevented by reducing the pumping speed substantially thus making this method quite time consuming.

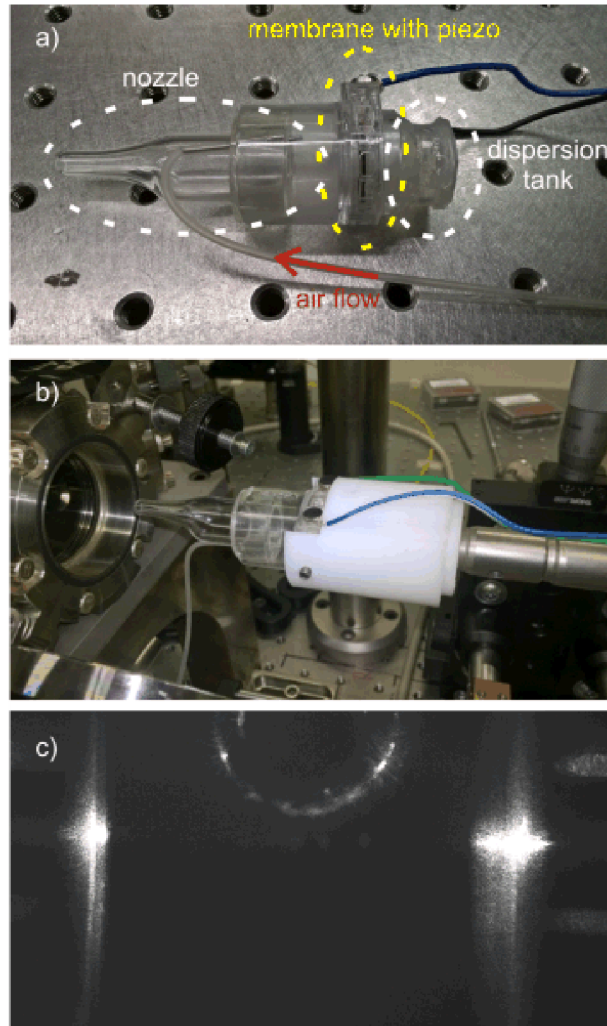


Fig. 2.6: Ultrasonic nebuliser modified for particle loading. (a) only the membrane with piezoelement is taken from the commercial nebuliser, a tank for the dispersion is glued on the back-side of the membrane, on the front-side a glass nozzle is attached with silicon ring. Air is pushed into the nozzle through a silicon hose. (b) The whole nebuliser is inserted into the chamber by sliding mechanism. (c) Droplets falling through the trapping beam.

## 2.4.2 Laser induced acoustic desorption

The second method of loading the particles into optical trap we implemented is laser induced acoustic desorption [73], also known as optical catapult. We spin-coat two or three layers of the beads on top of a silicon wafer ( $200\ \mu\text{m}$  thick). The particles are attracted to the surface by Van-der-Waals forces which need to be overcome in order to release the particles. Acoustic desorption aims at moving the surface sufficiently fast to shake the particles off. The necessary acceleration can be achieved by absorption of high power laser pulses. We put the wafer into the vacuum

chamber approximately 5 mm under the optical trap reduce the pressure to 5 - 10 mbar. We hit the bottom side of the wafer by a single focused laser pulse of central wavelength 532 nm, spot diameter 300  $\mu\text{m}$  and 10 - 15 mJ energy in pulse. The pulse is absorbed in the wafer and creates an acoustic wave propagating through it to the top side [74], subsequently catapulting a cloud of beads upwards [75] to the optical trap (Fig. 2.7b)) from surface area of size comparable to the laser spot. The initial velocity of the catapulted beads and the height they reach depend on gas pressure and power density of the pulse hitting the wafer [73]. Basically the lower the pressure and the bigger the power density of the pulse, the higher the beads are catapulted. So fine-tuning these two parameters the beads can be catapulted in a way that by the time they reach the trap height they are slow enough to be trapped.

Apparently, after couple of pulses the beads from the surface area and the pulse incidence spot has to be moved. Simultaneously the laser beam spot has to be placed under the trap quite precisely so the particles hit the trap. Little shift of the focus position can be done by tilting the beam in front of the focusing lens by mirror (Fig. 2.7a)) but after some more shots the whole wafer needs to be moved inside the vacuum chamber. We avoided the need for venting and opening the chamber by installing a simple wafer holder which can be moved from outside of the chamber. The holder consists of two teflon parts (Fig. 2.7a)). One part is placed inside the chamber, it is sitting on the bottom vacuum viewport under the optical trap and it is carrying the silicon wafer. This first part has pieces of steel installed in it. The second part of the holder is placed outside the chamber on the viewport and it incorporates set of neodymium magnets. The two parts are magnetically coupled and by shifting the outside part, the inside part is also shifted enabling us to adjust the wafer without the necessity of venting.

Compared to the nebuliser technique, the catapulting avoids the slow and problematic pumping from air pressure and if needed, a single particle can be loaded quickly again. From our experience, more than one particle are trapped extremely rarely and trying to trap additional particle by catapulting once more leads nearly always to losing the original one. So catapulting is not suitable for loading more than one particle. Additionally the optical access used for the pulsed laser optical path and the wafer holder cannot be used for anything else thus considerably restricting the experiment.

## 2.5 Vacuum system

The vacuum system is depicted in Fig. 2.5. The evacuation is done by a turbomolecular pumping station (Pfeiffer HiCube 80 Eco) consisting of a diaphragm backing pump (Pfeiffer MVP 015-2) and a turbopump (Pfeiffer HiPace 80) with ultimate



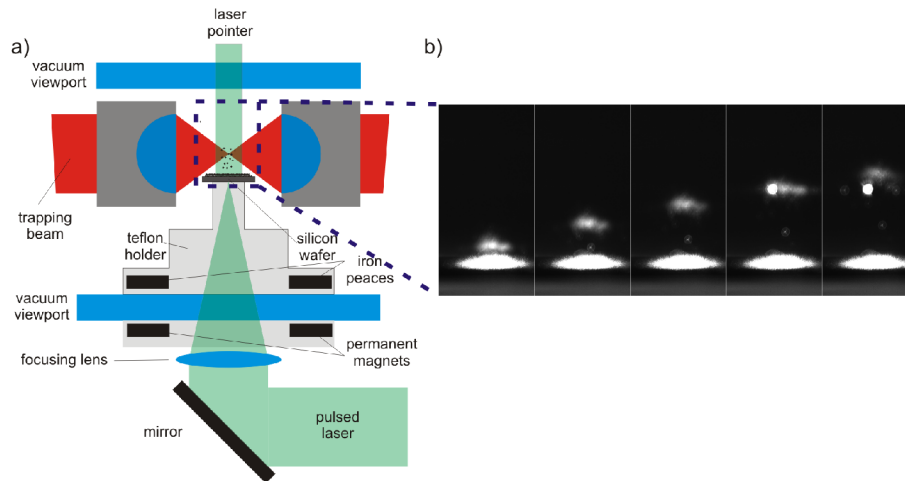


Fig. 2.7: Optical catapult. (a) geometry of the loading mechanism by optical catapult with movable holder; (b) cloud of catapulted particles ascending towards the trap and reaching the trap (bright spot on the right).

pressure of  $10^{-7}$  mbar. For experiments not requiring pressures lower than 3 mbar the turbopump can be turned off and the system can be pump down only by diaphragm pump. In order to be able to pump either very fast or very slowly and in a controlled manner, we split the tubing between the chamber and the pump into two branches. The chamber is separated from the pump by a different valve in each branch. During fast pumping or venting the variable leak valve is closed and the gate valve is open. Inverse variant is chosen when we load a particle by nebuliser and pump down from the atmospheric pressure with a particle trapped. We close the gate valve and adjust the variable leak valve in a way that the gas flow is not strong enough to push the particle out but still the pumping does not take too long. Also when we perform a pressure dependent measurement we often start the experiment in higher pressure and decrease it in steps by opening and closing the variable leak valve. Also starting with low pressure and increasing it in steps is possible. In this case the pump side of the tubing is at atmospheric pressure and the variable leak valve leaks air into the chamber.

The pressure is measured by combined gauge (Pfeiffer PKR 251) consisting of Pirani gauge ( $10^3 - 10^{-4}$  mbar) and cold cathode gauge ( $10^{-4} - 5 \cdot 10^{-9}$  mbar) which is placed as close to the chamber as possible. The gauge is read out by its controller (Pfeiffer TPG 262) which can also be connected to computer via RS 232 interface.

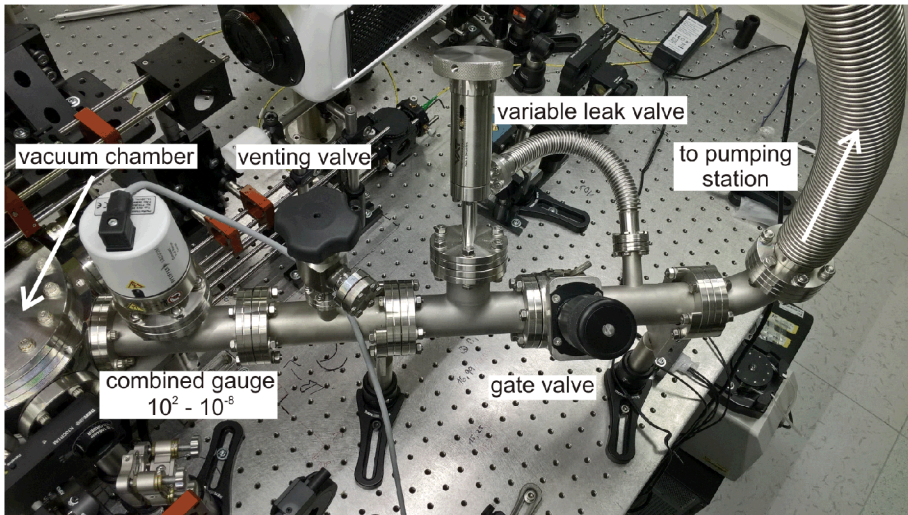


Fig. 2.8: Vacuum system.

### 3 Transverse spin forces and non-equilibrium particle dynamics in a circularly polarized vacuum optical trap

The optically levitated particle became popular platform to study stochastic thermodynamics. The ability to design and dynamically change the optical potential or to control the stochastic forces opened experimental ways to test fluctuation theorems [48], test information thermodynamics [49] or realize compression stages of heat engines [50]. In the presented paper we show that an optical trap consisting of two counter-propagating circularly polarized laser beams gives rise to a non-conservative force field in azimuthal direction which drives the particle out of thermal equilibrium. Depending on the conditions, the dynamics of the particle can range from stochastic motion near thermal equilibrium to stable orbital motion around the optical axes, rendering such optical traps promising testbed for non-equilibrium statistical mechanics.

Second intriguing aspect of this experiment is the origin of the azimuthal component of the optical force itself. According to Newton's third law, the optical force acting on a particle emerges as a result of change of momentum of photons. Consequently, the momentum of light can be studied by observing mechanical effect of light on a probe particle. The observed dynamics is a manifestation of mechanical effect of optical spin. Spin angular momentum is given by the polarization state of the light beam, linearly polarised light having zero and circularly polarised light having maximal spin [76, 77]. Under certain circumstances the spin angular momentum generates a spin dependent component of linear momentum of the beam,  $\mathbf{p}^S$ , which tends to point in transverse direction [76, 78, 79]. This component of the linear momentum was previously thought to be virtual and unmeasurable. Here, its effect is revealed in the inertial motion of a probe particle in a circularly polarized Gaussian trap, in vacuum.

The results presented below in this chapter is a typical example of our team collaboration. I was responsible for design, development and operation of the experimental setup (described in detail in Chapter 2). I also carried out all the measurements and performed part of data processing.

Since it is the central theme of the presented article, this chapter starts by discussing optical momentum and optical forces in more detail, than it was possible to include in the article itself. Then the article is included, followed by derivation of trapped particle motion characteristics used in the paper (equation of motion, position power spectrum density, position variance) and data processing techniques.

## 3.1 Optical Momentum and forces

### 3.1.1 Optical momentum

The mechanical action of an optical field is connected to the change of momentum of photons scattered off a piece of matter. This also means that by observation of mechanical effects we can study the momentum of the field. In the presented article, we state that the observation of a transverse spin force is evidence of transverse spin momentum. This association is not trivial: optical momentum can be decomposed in various ways, and the ways in which these components couple to matter is open to interpretation. Furthermore, momentum is a point-wise property of the field, while forces are integral quantities. We note that the connection between optical force and momentum is a fundamental issue, effecting the interpretation of all such experiments. The relationship between optical torque and spin angular momentum is analogous. Circularly polarized light was first observed to rotate objects by Beth in 1936 [80], yet the interpretation of this experiment continues to be debated [81].

Considering a monochromatic electromagnetic field in vacuum with electric and magnetic vectors  $\Re[\mathbf{E} \exp(-i\omega t)]$  and  $\Re[\mathbf{H} \exp(-i\omega t)]$ , the field momentum density  $\mathbf{p}$  is proportional to Poynting vector  $\mathbf{S}$

$$\mathbf{p} = \frac{\mathbf{S}}{c^2} = \frac{1}{2c^2} \Re(\mathbf{E}^* \times \mathbf{H}), \quad (3.1)$$

where  $\mathbf{E}$  and  $\mathbf{H}$  are the complex amplitudes. The Poynting momentum (3.1) can be decomposed into distinct components in various ways. In vacuum, most decompositions seek to separate out a spin component. This can be achieved with emphasis placed on the electric field (as we do in the presented article), the magnetic field or on their average [77, 82]:

$$\mathbf{p} = \frac{1}{2c^2} \Re(\mathbf{E}^* \times \mathbf{H}) = \frac{\epsilon}{2\omega} \left[ \Im(\mathbf{E}^* \cdot (\nabla)\mathbf{E}) + \frac{1}{2} \nabla \times \Im(\mathbf{E}^* \times \mathbf{E}) \right] \equiv \mathbf{p}_{\mathbf{E}}^{\mathbf{O}} + \mathbf{p}_{\mathbf{E}}^{\mathbf{S}} \quad (3.2a)$$

$$\mathbf{p} = \frac{1}{2c^2} \Re(\mathbf{E}^* \times \mathbf{H}) = \frac{\mu}{2\omega} \left[ \Im(\mathbf{H}^* \cdot (\nabla)\mathbf{H}) + \frac{1}{2} \nabla \times \Im(\mathbf{H}^* \times \mathbf{H}) \right] \equiv \mathbf{p}_{\mathbf{H}}^{\mathbf{O}} + \mathbf{p}_{\mathbf{H}}^{\mathbf{S}} \quad (3.2b)$$

$$\mathbf{p} = \frac{1}{2} \left( \mathbf{p}_{\mathbf{E}}^{\mathbf{O}} + \mathbf{p}_{\mathbf{H}}^{\mathbf{O}} \right) + \frac{1}{2} \left( \mathbf{p}_{\mathbf{E}}^{\mathbf{S}} + \mathbf{p}_{\mathbf{H}}^{\mathbf{S}} \right) \equiv \mathbf{p}_{\mathbf{E-H}}^{\mathbf{O}} + \mathbf{p}_{\mathbf{E-H}}^{\mathbf{S}} \quad (3.2c)$$

The choice of gauge provides a further degree of freedom [78]. We interpret our results in terms of Eq. (3.2a), for the following reasons:

1. For the quasi-paraxial light beams we use here, orbital components of the momentum (e.g.  $\mathbf{p}_{\mathbf{E}}^{\mathbf{O}}, \mathbf{p}_{\mathbf{H}}^{\mathbf{O}}, \mathbf{p}_{\mathbf{E-H}}^{\mathbf{O}}$ ) are very small or negligible in transverse directions (see supplementary note 2 of [83]). Thus, the spin components ( $\mathbf{p}_{\mathbf{E}}^{\mathbf{S}}, \mathbf{p}_{\mathbf{H}}^{\mathbf{S}}, \mathbf{p}_{\mathbf{E-H}}^{\mathbf{S}}$ ) are approximately equivalent in the transverse plane.
2. The force on a small, finite particle can be decomposed into parts that can be directly identified with the underlying components of momentum (see Eqns.

(3.5, 3.6)). This provides an immediate association with the decomposition Eq. (3.2a), and also with the Coulomb gauge which gives the force due to the orbital component of the momentum,  $\mathbf{p}_E^O$  [78].

3. For Mie particles this formal association between spin force and spin momentum is lost. Nevertheless, a transverse force on a sphere requires a source of transverse momentum.
4. For dielectrics, the decomposition Eq. (3.2a) has been shown to make sense in a variety of experimental systems, including for spheres and slabs in the Mie regime [84, 78, 85].
5.  $\mathbf{p}_E^S$  and  $\mathbf{p}_E^O$  have been shown to couple to dielectrics in the Mie regime, in qualitatively different ways. For instance, consideration of the optical forces on finite flat plates indicate that  $\mathbf{p}_E^S$  couples to matter via an edge effect [84].

Taken together, these points suggest that the decomposition Eq. (3.2a) is appropriate and physically meaningful not only for small particles but also for dielectric objects in the Mie regime. For these reasons, we neglect the  $\mathbf{E}$  and  $\mathbf{H}$  subscripts throughout the text and refer generically to the spin,  $\mathbf{p}^S \equiv \mathbf{p}_E^S$  and orbital,  $\mathbf{p}^O \equiv \mathbf{p}_E^O$ , components of the momentum and we write:

$$\mathbf{p} = \frac{\epsilon_0}{2\omega} \Im(\mathbf{E}^* \times \nabla \times \mathbf{E}) \quad (3.3a)$$

$$\mathbf{p}^O = \frac{\epsilon_0}{2\omega} \Im(\mathbf{E}^* \cdot (\nabla)\mathbf{E}) \quad (3.3b)$$

$$\mathbf{p}^S = \frac{\epsilon_0}{4\omega} \nabla \times \Im(\mathbf{E}^* \times \mathbf{E}) \quad (3.3c)$$

### 3.1.2 Optical forces - small particle approximation

Assuming a dielectric and isotropic particle of radius  $a$  is much smaller than the wavelength of the light  $\lambda$  ( $ka \ll 1$ ), it can be approximated as a dipole. Then, the total force felt by the particle can be calculated using the Rayleigh scattering theory. To the leading order of electric-dipole approximation, the optical force is commonly expressed in literature as [86, 87, 88]:

$$\mathbf{F}^{\text{opt}} = \pi\epsilon_0 \Re(\alpha_e) \nabla |\mathbf{E}|^2 + 2\pi\epsilon_0 \Im(\alpha_e) \{2\omega\mu \langle \mathbf{S} \rangle + \Im[(\mathbf{E}^* \cdot \nabla)\mathbf{E}]\}. \quad (3.4)$$

Here,  $\epsilon_0$  is the particle vacuum permittivity and  $\alpha_e$  is the particle electric polarizability (defined below by equations (3.7)). The first term of the sum in (3.4) represents the *gradient force*  $\mathbf{F}^{\text{grad}}$ , which is given by the inhomogeneity of the field energy distribution  $W_e \propto |\mathbf{E}|^2$ . The second term describes the *scattering force*  $\mathbf{F}^{\text{scat}}$  and it is connected to the field momentum density. The scattering force consists of the 'traditional radiation pressure' (the first term in curly bracket) and the 'curl force' connected to the non-uniform spin angular momentum distribution (the second term in curly bracket).

It is worth noting that the two parts of the scattering force in Equation (3.4) are not independent and the expression can be further modified to [89]:

$$\mathbf{F}^{\text{opt}} = \pi\epsilon_0\Re(\alpha_e)\nabla|\mathbf{E}|^2 + 2\pi\epsilon_0\Im(\alpha_e)\mathbf{p}^O \quad (3.5)$$

where  $\mathbf{p}^O$  is the orbital momentum defined by Eq. (3.3b). This modification shows that in the lowest order, the force on a small particle is governed by the energy density and orbital momentum density only.

The spin momentum density  $\mathbf{p}^S$  defined by Eq. (3.3c) appears in the next higher order interaction, which is the dipole-dipole interaction between the induced electric and magnetic dipoles. The correction reads [84, 78]:

$$\mathbf{F}^1 = -\frac{\omega^3}{3}\Re(\alpha_e\alpha_m^*)(\mathbf{p}^O + \mathbf{p}^S) - \mathbf{F}^{\text{Im}}. \quad (3.6)$$

$\alpha_{e/m}$  is the electric/magnetic polarizability which, for dielectric particles, is approximately:

$$\alpha_{e/m} = \alpha_{e/m}^0 / (1 - \frac{2}{3}ik^3\alpha_{e/m}^0) \quad (3.7a)$$

$$\alpha_e^0 \approx \frac{\epsilon_m}{k^3} \left[ \frac{(\epsilon_p - \epsilon_m)(ka)^3}{(\epsilon_p + 2\epsilon_m)} \right] \quad (3.7b)$$

$$\alpha_m^0 \approx \frac{(\epsilon_p - \epsilon_m)(ka)^5}{30k^3\epsilon_m} \quad (3.7c)$$

Here,  $\alpha_{e/m}^0$  are the Clausius-Mossotti polarizabilities for dielectric particles with  $\epsilon_{m/p}$  the relative permittivity of medium/particle and permeability equal to one.  $\alpha_{e/m}$  are the polarizabilities, corrected for finite size. These latter polarizabilities contain an imaginary part, even for non-absorbing particles, that produces the scattering force captured by Eq. (3.5).

The last term in Eq. (3.6),  $\mathbf{F}^{\text{Im}} \propto \Im(\alpha_e\alpha_m^*)\Im(\mathbf{E}^* \times \mathbf{H})$ , is a contribution, which is proportional to imaginary part of the product of electric and magnetic polarizabilities. Considering equations (3.7) we get  $|\Re(\alpha_e\alpha_m^*)| \propto k^5a^8$  but  $|\Im(\alpha_e\alpha_m^*)| \propto k^8a^{11}$ . For small particles,  $ka \ll 1$ , the force  $\mathbf{F}^{\text{Im}}$  is much weaker than the contributions from  $\mathbf{p}^O$  and  $\mathbf{p}^S$  and it can be neglected.

If the size of the particle is comparable to the wavelength of light ( $ka \sim 1$ ), Rayleigh approximation is not appropriate and the Lorentz-Mie theory of scattering has to be used. Here, the optical force is calculated from the photon momentum change by calculating the incoming and outgoing fields. In the Mie regime, there is no formal way to associate transverse spin forces with  $\mathbf{p}^S$ . Nevertheless, when a high-symmetry object, such as a sphere, experiences a force in a particular direction, there must be an underlying source of momentum.

ARTICLE

<https://doi.org/10.1038/s41467-018-07866-8>

OPEN

# Transverse spin forces and non-equilibrium particle dynamics in a circularly polarized vacuum optical trap

V. Svak<sup>1</sup>, O. Brzobohatý<sup>1</sup>, M. Šiler<sup>1</sup>, P. Ják<sup>1</sup>, J. Kaňka<sup>1</sup>, P. Zemánek<sup>1</sup> & S.H. Simpson<sup>1</sup>

We provide a vivid demonstration of the mechanical effect of transverse spin momentum in an optical beam in free space. This component of the Poynting momentum was previously thought to be virtual, and unmeasurable. Here, its effect is revealed in the inertial motion of a probe particle in a circularly polarized Gaussian trap, in vacuum. Transverse spin forces combine with thermal fluctuations to induce a striking range of non-equilibrium phenomena. With increasing beam power we observe (i) growing departures from energy equipartition, (ii) the formation of coherent, thermally excited orbits and, ultimately, (iii) the ejection of the particle from the trap. As well as corroborating existing measurements of spin momentum, our results reveal its dynamic effect. We show how the under-damped motion of probe particles in structured light fields can expose the nature and morphology of optical momentum flows, and provide a testbed for elementary non-equilibrium statistical mechanics.

<sup>1</sup>The Czech Academy of Sciences, Institute of Scientific Instruments, Královopolská 147, 612 64 Brno, Czech Republic. Correspondence and requests for materials should be addressed to S.H.S. (email: [simpson@isibrno.cz](mailto:simpson@isibrno.cz))

Although its existence has been recognized since the time of Kepler, the momentum of light remains a subject of intense debate. Uncertainty over its value when propagating through continuous media continues to excite interest<sup>1</sup>. Even in free space the topic is not without controversy. For example, the time averaged Poynting momentum in free space can be separated into two parts<sup>2–4</sup> whose differing properties have yet to be fully understood:

$$\mathbf{p} = \frac{1}{2c^2} \Re(\mathbf{E}^* \times \mathbf{H}) = \frac{\epsilon_0}{2\omega} \Im[\mathbf{E}^* \cdot (\nabla)\mathbf{E}] + \frac{\epsilon_0}{4\omega} \nabla \times \Im[\mathbf{E}^* \times \mathbf{E}] \equiv \mathbf{p}^O + \mathbf{p}^S, \quad (1)$$

(in SI units, with  $c$  the speed of light, and  $\epsilon_0$  the permittivity, in vacuum). The first of these contributions,  $\mathbf{p}^O$ , is independent of polarization, and referred to as the orbital component. The second term,  $\mathbf{p}^S$ , is related to inhomogeneous circular polarization, and referred to as the spin component. Alternative decompositions of the momentum are discussed in Supplementary Note 1. Eq. (1) is the most appropriate as the different components,  $\mathbf{p}^S$  and  $\mathbf{p}^O$ , couple to dielectric matter in qualitatively different ways for dielectric objects of small or intermediate size<sup>5–7</sup>.

Interest in these distinct contributions is rooted in field theory, as has been extensively discussed elsewhere<sup>6,8,9</sup>. In summary, the field theoretic basis of the Poynting momentum rests on Belifante's symmetrization of the canonical stress energy tensor, derived by applying Noether's theorem to the electromagnetic Lagrangian<sup>10,11</sup>. This modification ensures conservation of angular momentum, removes the gauge dependence of physical quantities, and resolves various other inconsistencies<sup>10,11</sup>. In this context,  $\mathbf{p}^O$  can be identified as the canonical momentum derived

from the Noether theorem, evaluated in the Coulomb gauge. This term gives the optical scattering force on a point particle (Supplementary Note 2). The spin part of the Poynting vector,  $\mathbf{p}^S$ , appears as a consequence of symmetrization and was thought to be virtual, as it does not contribute to the overall momentum of the field ( $\int_{\infty} \mathbf{p}^S dV = 0$ ). The physical origin of  $\mathbf{p}^S$  can be conceptually understood in terms of spin momentum loops<sup>6</sup>. In infinite, homogeneous fields, contributions from neighboring loops cancel. Spatial inhomogeneities, including intensity gradients, break this balance, generating a non-zero boundary spin current,  $\mathbf{p}^S \neq 0$ <sup>6</sup>. Figure 1b illustrates this mechanism for circularly polarized beams, as used in this work.

The question of how and, indeed, if  $\mathbf{p}^S$  couples to matter presents itself. Addressing this issue is experimentally challenging. Spin momentum ( $\mathbf{p}^S$ ) requires field inhomogeneities which, by necessity, generate other forms of optical force, including gradient forces. To measure its effect, delicate spin forces must be reliably distinguished from other stronger forces. This was elegantly achieved in a recent experiment, in which the deflection of a nano-cantilever, immersed in a circularly polarized evanescent field was measured<sup>5</sup>. In this case, the spin dependence of the force is isolated, from the prevailing effects of orbital momentum, by varying the degree of circular polarization, applying a symmetry argument and by observing that, in an evanescent wave, spin and orbital components of momentum are orthogonal<sup>6</sup>. Other experiments require minute analysis of the motion of particles in liquid, subject to appropriate light fields<sup>12,13</sup>. Related or analogous effects rely on substrate interactions or optical chirality or birefringence<sup>14–17</sup> and, whereas fascinating in their own right, do not depend explicitly on incident spin momentum.

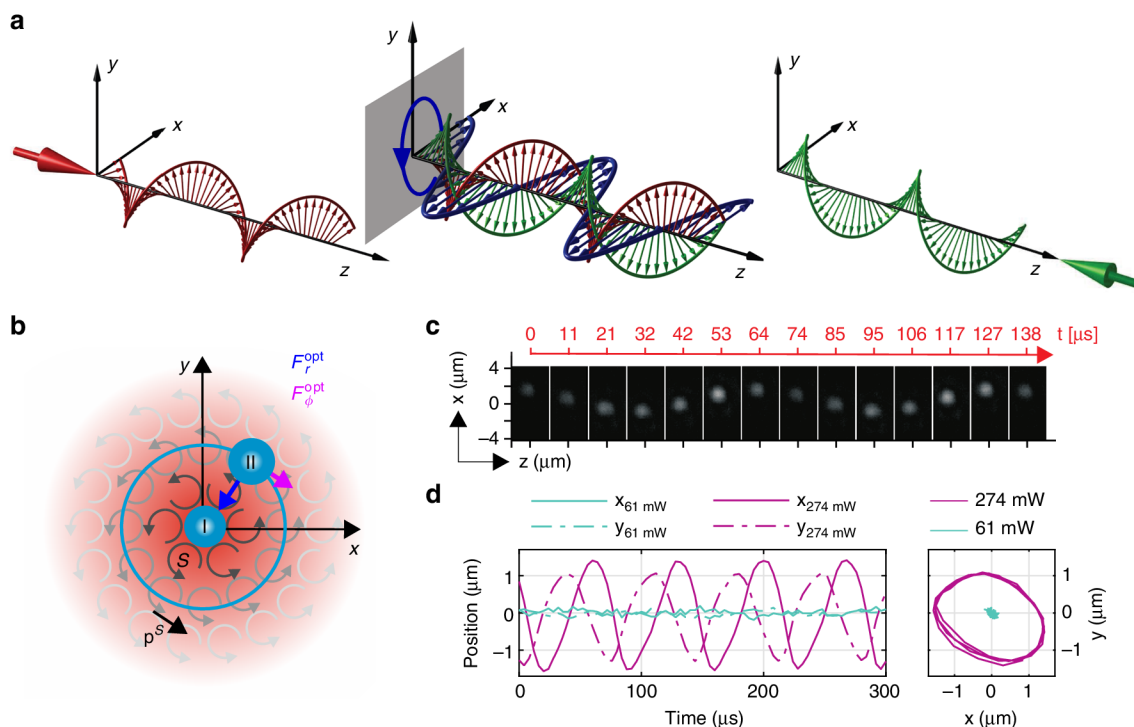


**Fig. 1** Physical principles of the experiment. **a** Schematic showing the electric fields in the counter-propagating circularly polarized beams of opposing handedness (green and red) and the rotation of the combined electric field (blue). **b** Local optical spin ( $\mathbf{S} = \Im(\mathbf{E}^* \times \mathbf{E})$ ) field in the transverse  $xy$  plane of the beam. Radial gradient optical force  $F_r^{\text{opt}}$  and azimuthal non-conservative spin force,  $F_\phi^{\text{opt}}$  acting upon a particle positioned off-axis. Regime I corresponds to the particle position in the vicinity of the beam axis for lower laser power, whereas regime II corresponds to the above threshold condition, in which the particle orbits the beam axis. **c** Snapshots of orbiting particle (regime II) taken by the CCD camera oriented perpendicularly to the beam propagation. **d** Trajectories of the particle for both regimes I and II acquired by a QPD. Turquoise curves denote trajectories for a lower trapping power of 55 mW with particle motion near the beam axis; pink trajectories show an orbiting particle for an above threshold power of 180 mW



We note that mechanical tests of spin momentum generally require a minor caveat. There is no unique definition of  $\mathbf{p}^S$  and, in the Mie regime, there is no formal way to associate transverse spin forces with  $\mathbf{p}^S$ . Nevertheless, when a high-symmetry object, such as a sphere, experiences a force in a particular direction, there must be an underlying source of momentum. These matters are discussed further in Supplementary Note 1.

In this work, we consider the motion of a probe microsphere in an almost paraxial, circularly polarized Gaussian vacuum trap. Pronounced departures from equilibrium behavior are observed that demonstrate the presence of transverse spin forces deriving from corresponding components of optical momentum.

## Results

**Physical principles and overview of the experiment.** In our experiments, spin forces manifest themselves directly, through the inertial motion of a microsphere in a vacuum optical trap, in free space. Such traps are used in the pursuit of ground state cooling of macroscopic objects<sup>18–20</sup>, for studying aspects of nano-scale dynamics<sup>21,22</sup> and statistical mechanics<sup>23–25</sup>. By comparison with the relatively subtle effects previously observed, our results are striking and unequivocal. Ultimately, we observe the violent ejection of a probe particle from an optical trap, as a direct consequence of transverse optical spin momentum. The experiment itself is elegant in its simplicity. We track the motion of a small, dielectric probe particle in a counter-propagating Gaussian beam trap, in vacuum (see Fig. 1a, b). The beams are weakly focused with a numerical aperture of  $NA \approx 0.18$  (equivalent to a Rayleigh range of  $kz_R \approx 150$ , for wave-vector  $k$ ). This symmetric geometry nullifies the axial scattering forces associated with each beam<sup>26</sup> and emphasizes transverse spin components, when they are present. The polarization state of the beams can be independently adjusted using quarter-wave plates on either side of the trap (see Methods). When the beams have parallel, linear polarization (LP), the only surviving forces in the trap are optical gradient forces. These forces attract the particle toward the beam axis, and provide a periodically modulated force, in the axial direction, that is associated with the interference fringes of the standing wave (see Supplementary Note 2). As gradient forces are conservative, thermal equilibrium is maintained within the trap and the thermal motion of the particle complies with the equipartition of energy, so that elastic energy of the trap is equal to the thermal energy. In particular, the optical restoring force,  $F_i$ , is linearly proportional to displacement,  $x_i$ , to first order, e.g.,  $F_i = -K_i x_i$ , where  $K_i$  is the trap stiffness in direction  $i$ .  $K_i$  is directly proportional to the optical power,  $K_i = Pk_i$ . Equating thermal and elastic energies gives  $\frac{1}{2}k_B T = \frac{1}{2}K_i \langle x_i^2 \rangle$ , so that the greater the power in the trap, the more tightly the particle is constrained, i.e.,  $\langle x_i^2 \rangle \propto 1/P$ .

When the quarter-wave plates are adjusted so that the beams are circularly polarized with opposite handedness (CP) the electric field vectors of the beams rotate together, in the same sense, Fig. 1a. This has two effects. First, the weak focusing by the lens produces small, transverse components of  $\mathbf{p}^O$  through spin-orbit coupling<sup>27</sup>. Second, the inhomogeneous circular polarization generates transverse components of  $\mathbf{p}^S$ , which also circulate about the beam axis, Fig. 1b. For the quasi-paraxial beams used here, the various momentum decompositions are approximately equivalent, and the spin term is strongly dominant, with  $|p_\phi^S/p_\phi^O| \gtrsim (2kz_R) \approx 300$  (Supplementary Note 1). These transverse momenta give rise to azimuthal forces, primarily associated with  $\mathbf{p}^S$  (Supplementary Note 2). In combination with the optical gradient forces, the circularly polarized trap has a cylindrically symmetric force field,  $\mathbf{F}^{opt} = F_\phi^{opt} \mathbf{e}_\phi + F_r^{opt} \mathbf{e}_r$ , with all forces vanishing on the beam axis (see (Supplementary Note 2)). For

small displacements from the axis, the gradient force,  $F_r^{opt}$ , is restoring, attracting the particle toward the center of the beam. The azimuthal component,  $F_\phi$ , makes the trap non-conservative (i.e.,  $\nabla \times \mathbf{F}^{opt} \neq 0$ ), forcing it out of equilibrium and allowing the particle to accumulate angular momentum. Notably, the ratio of the radial gradient force to the azimuthal spin force is approximately constant over the width of the beam, i.e.,  $F_\phi^{opt}/F_r^{opt} \approx \text{const}$ , because they have a similar dependence on intensity gradients (see Supplementary Note 2). A detailed theoretical analysis of the momentum flows and optical forces acting on small and Mie particles is provided in Supplementary Note 1 and Supplementary Note 2.

The motion of the probe particle is determined by the delicate interplay between thermal fluctuations, spin and gradient optical forces and is governed by a Langevin equation, in Cartesian coordinates:

$$\mathbf{F}^{opt}(\mathbf{r}) + \mathbf{F}^L(t) - \xi \dot{\mathbf{r}} = m \ddot{\mathbf{r}}, \quad (2)$$

where  $m$  is the mass of the particle and  $\xi$  the pressure dependent Stokes' drag.  $\mathbf{F}^{opt} \equiv P\mathbf{f}^{opt}$  is the external optical force at power  $P$  and  $\mathbf{F}^L$  is the fluctuating Langevin force, which is uncorrelated in time with zero mean and variance given by the fluctuation–dissipation theorem, e.g.,  $\langle F_i^L(t) \rangle = 0$ ,  $\langle F_i^L(t) \otimes F_j^L(t') \rangle = 2k_B T \xi \delta_{ij} \delta(t - t')$  for Cartesian components  $i, j = x, y, z$ . For CP beams, we observe two distinct regimes (see depiction in Fig. 1c, d), dependent on optical power. These can be contrasted with the conspicuously different behavior observed in LP traps, which is qualitatively similar for all trap powers. At low optical powers (regime I) the particle undergoes non-equilibrium Brownian motion, deviating substantially from the equipartition of energy. At higher powers (regime II) we observe the formation of stable orbits, which are thermally excited and driven by optical spin.

**Regime I: driven Brownian motion.** In the low power regime I (turquoise curves, Fig. 1d), the particle remains within the linear range of the trap and, in Cartesian coordinates, the optical force can be approximated as,

$$\begin{bmatrix} F_x^{opt} \\ F_y^{opt} \end{bmatrix} = - \begin{bmatrix} K_r & K_\phi \\ -K_\phi & K_r \end{bmatrix} \begin{bmatrix} x \\ y \end{bmatrix}. \quad (3)$$

$K_r$  is the radial stiffness associated with the gradient force. It is isotropic and gives a force in the radial direction, toward the origin.  $K_\phi$  is the stiffness of the azimuthal force. Both stiffness coefficients are proportional to power, e.g.,  $K_r = Pk_r$  and  $K_\phi = Pk_\phi$ .

The resulting linear system has a set of characteristic frequencies  $\{\omega_c\}$ , which relate to qualitative features of the stochastic dynamics. In the case of weak damping,  $\xi^2 \ll 4mK_r$  (see Supplementary Note 3)

$$\omega_c \approx \pm \omega_0 + \frac{i}{2m} \left( \xi \pm \frac{K_\phi}{\omega_0} \right). \quad (4)$$

The real parts of  $\omega_c$  describe typical oscillation frequencies and, for all polarization states, they are approximately equivalent to the resonant trap frequency,  $\omega_0 = \sqrt{Pk_r/m}$ . The imaginary parts of  $\omega_c$ ,  $\Im(\omega_c)$ , represent damping or loss coefficients, associated with exponential decay. For linearly polarized beams, the azimuthal force is zero,  $k_\phi = 0$  so that  $\Im(\omega_c) = \xi/2m$  is positive and independent of power. In contrast, when  $k_\phi \neq 0$ , the imaginary parts of two of the characteristic frequencies approach

zero as the optical power approaches a critical value,  $P_{\text{thr}}$ :

$$\frac{P_{\text{thr}}}{\xi^2} = \frac{k_r}{mk_\phi^2}. \tag{5}$$

At  $P = P_{\text{thr}}$ , the corresponding threshold frequency  $\Omega_{\text{thr}} \equiv \omega_0(P_{\text{thr}})$  satisfies,

$$\frac{\Omega_{\text{thr}}}{\xi} = \frac{k_r}{mk_\phi}. \tag{6}$$

As demonstrated below, these conditions (Eqs. 5 and 6) describe the boundary between regimes I and II, and are achieved when average centripetal forces acquired by the Brownian particle are just sufficient to balance attractive, gradient forces.

In regime I, where the power is below threshold ( $P < P_{\text{thr}}$ ), the stochastic motion of the probe particle can be characterized in terms of the power spectral density (PSD) and the time correlations of the particle coordinates. The former quantifies the energy in the particle motion as a function of frequency. The latter relates to underlying deterministic motion. For instance,  $\langle x(t)y(t+\tau) \rangle$  measures the correlation between the  $x$  coordinate at time  $t$  with the  $y$  coordinate at a later time  $(t+\tau)$ . For  $\tau=0$ , we get the instantaneous variances of the coordinates. Both the PSD and the time correlations can be expressed in terms of  $\omega_c$  (see Supplementary Note 3) and both depend qualitatively on the presence of spin forces (i.e., on whether or not  $k_\phi = 0$ ). Table 1 summarizes the results.

In both cases, the PSD of the system is dominated by a single peak, approximately at the resonant frequency,  $\omega_0 = \sqrt{Pk_r/m}$  (see Supplementary Note 3). For conservative, linearly polarized beams, the peak height decreases with increasing optical power ( $\propto 1/P$ ) and has a constant width associated with the drag term.

For very low optical power, the circularly polarized trap behaves similarly. However, as the power increases and approaches the threshold,  $P_{\text{thr}}$ , a qualitative difference emerges and the peak grows in height,  $\propto 1/(P_{\text{thr}} - P)^2$ , whereas decreasing in width in proportion to  $\Im(\omega_c) \approx \frac{\xi}{2m} \frac{(P_{\text{thr}} - P)}{2P_{\text{thr}}}$ . Physically, the white thermal noise excites a resonance in which frictional losses are increasingly compensated by the non-conservative spin forces and the behavior becomes increasingly coherent and deterministic. In this respect the behavior of the trap is analogous to that of a laser approaching the lasing threshold. These theoretical predictions are supported by the experimental results in Fig. 2.

Time correlations (Supplementary Note 3) measure the rate at which the motion loses coherence owing to thermal fluctuations. In general,  $\langle x(t+\tau)x(t) \rangle$  and  $\langle y(t+\tau)y(t) \rangle$  are

damped oscillations. As  $P \rightarrow P_{\text{thr}}$ , see Table 1, the amplitude of  $\langle x(t+\tau)x(t) \rangle$  increases as  $1/(P_{\text{thr}} - P)$ , and decays increasingly slowly with time. Meanwhile,  $\langle x(t+\tau)y(t) \rangle$  has the same amplitude, but is phase shifted by  $\pi/2$ , indicating a growing tendency toward rotation of the center of mass about the beam axis. Experimental results strongly support this idea, see Fig. 2c, d. Once more, they clearly demonstrate an increase of motional coherence for circularly polarized beams for powers approaching the threshold power.

For zero time ( $\tau=0$ ), the instantaneous variances of the particle coordinates, e.g.,  $\langle x^2 \rangle$ , quantify the departure from thermodynamic equilibrium. In a conservative, harmonic trap (i.e., linearly polarized beams) equipartition is satisfied and the elastic and thermal energies can be equated, e.g.,  $\frac{1}{2}Pk\langle x^2 \rangle = \frac{1}{2}k_B T$ , so that the product,  $P\langle x^2 \rangle$  is constant. In contrast, the circularly polarized trap deviates increasingly from equipartition as  $P_{\text{thr}}$  is approached, so that  $\langle x^2 \rangle \propto 1/(P_{\text{thr}} - P)$  increases rapidly, as confirmed experimentally in Fig. 2e. Figure 2f illustrates this phenomenon visually: the two-dimensional probability density distribution of the trapped particle in the transversal plane, scaled by the square root of the beam power, is invariant for a conservative trap but grows with increasing power in the presence of non-conservative forces.

In combination, the PSD, time correlations, and variances reveal the underlying physical behavior. Optical forces vanish on the beam axis and are locally restoring so that points on the beam axis are mechanical equilibria. Nevertheless, thermal fluctuations repeatedly push the particle off-axis, exposing it to the small, azimuthal spin forces. These increase the tendency for the particle to orbit about the beam axis, as expressed by the time correlations,  $\langle x(t+\tau)y(t) \rangle$  and  $\langle x(t+\tau)x(t) \rangle$ . Centripetal forces grow and act against the gradient forces, effectively canceling them as  $P \rightarrow P_{\text{thr}}$ . Under these conditions, the stochastic motion becomes increasingly coherent in terms of rotation: kinetic energy is increasingly concentrated at a single, resonant frequency as indicated in the PSD (Fig. 2b). Conversely, the radial motion is increasingly incoherent, and the particle is free to explore the trap (i.e.,  $\langle x^2 \rangle \rightarrow \infty$ ). Crucially, these non-equilibrium effects are absent for linearly polarized beams and only appear when for circular polarization. This further demonstrates that our trap is free from circulating flows of momentum, caused by beam misalignment, that would push even LP beams out of equilibrium<sup>28</sup>.

As the power is increased above  $P_{\text{thr}}$ , centripetal forces tend to exceed gradient forces, and the particle is pushed outward. If the force field were truly linear, this process would continue indefinitely. In reality, the trap is finite. Stable orbits with well defined radii,  $r_\infty$ , and frequency,  $\Omega$ , can form as the particle encounters non-linear regions of the trap, taking us into the high power regime II (purple curves, Fig. 1d).

**Table 1 Comparison summary for stochastic motion in CP and LP beams in regime I**

Quantity	Linear polarization (LP) $K\phi = 0$	Circular polarization (CP) $K\phi \neq 0$
$\omega_c$	$\approx \pm \omega_0 + \frac{i\xi}{2m}$	$\approx \pm \omega_0 + \frac{i\xi}{2m} \left(1 \pm \sqrt{\frac{P}{P_{\text{thr}}}}\right)$
PSD peak height	Decreases with power	Increases with $P \rightarrow P_{\text{thr}}$
$\langle X(\omega)X^*(\omega) \rangle_{\text{max}}$	$= \frac{2k_r T}{\xi \omega_0^2} \propto \frac{1}{P}$	$\approx \frac{2k_r T (\xi^2 \omega_0^2 + K_\phi^2) P_{\text{thr}}^2}{m^2 \xi \omega_0^2 (P - P_{\text{thr}})^2} \propto \frac{1}{(P - P_{\text{thr}})^2}$
PSD peak width at half maximum	Power independent $\approx \frac{\xi}{2m}$	Decreases towards zero with increasing power $\approx \frac{\xi}{2m} \left(1 \pm \sqrt{\frac{P}{P_{\text{thr}}}}\right)$
Time correlations	Decay power independent	Decay decreases with $P \rightarrow P_{\text{thr}}$
$\langle x(t)x(t+\tau) \rangle$	$\approx \frac{k_r T}{K_r} \cos(\omega_0 \tau) e^{-\xi \tau / 2m}$	$\approx \frac{\cos(\omega_0 \tau)}{P - P_{\text{thr}}} e^{\xi(P - P_{\text{thr}})\tau / 4mP_{\text{thr}}}$
$\langle x(t+\tau)y(t) \rangle$	$\approx 0$	$\approx \pm \frac{\sin(\omega_0 \tau)}{P - P_{\text{thr}}} e^{\xi(P - P_{\text{thr}})\tau / 4mP_{\text{thr}}}$

Characteristic frequencies,  $\omega_c$ , PSD characteristics and time correlations describing under-damped stochastic motion in circularly and linearly polarized beams

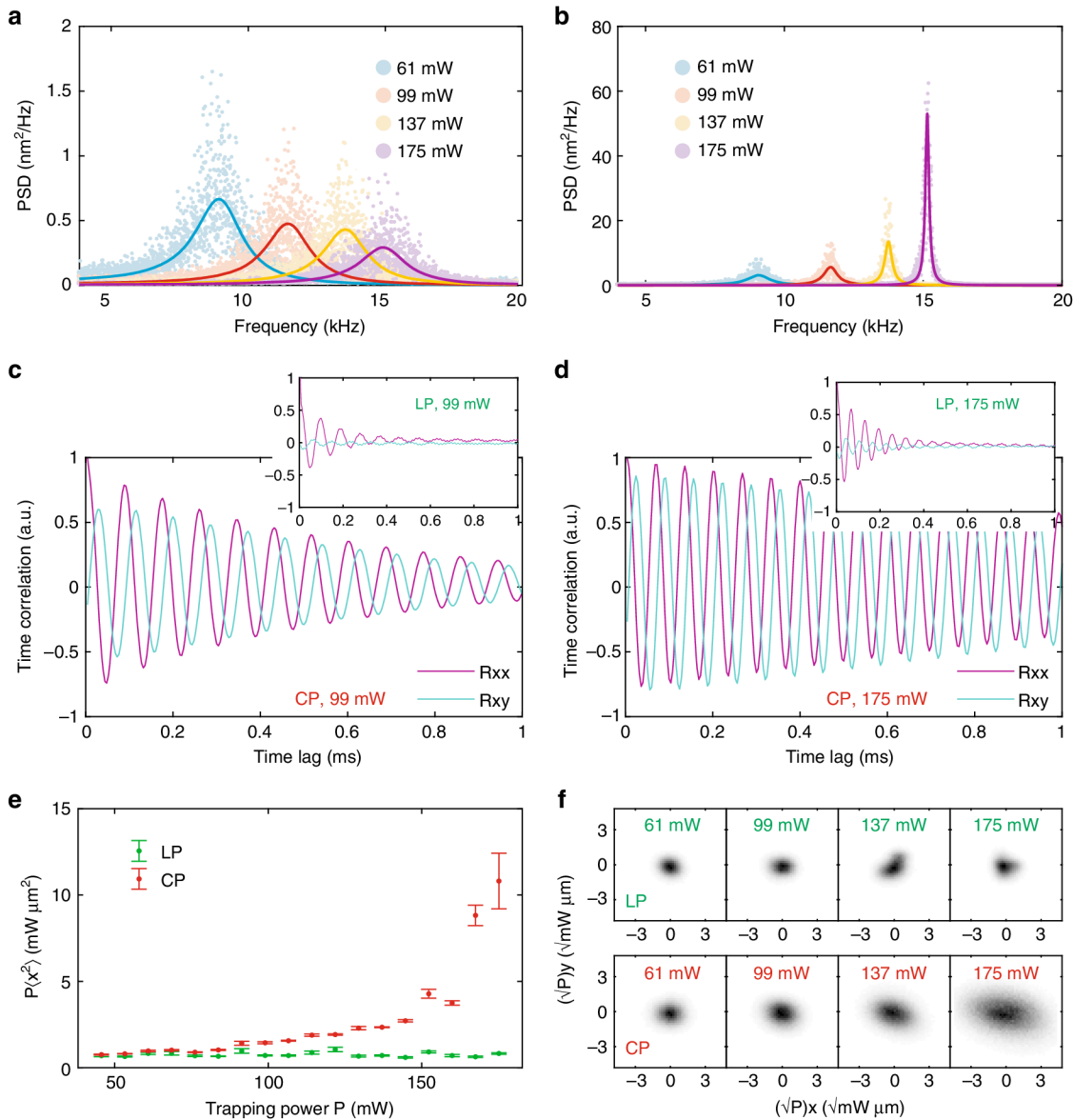


**Fig. 2** Characteristics of the stochastic motion in Regime I. Power spectral densities for particle positions for **a** LP **b** CP beams. In the latter case, spin momentum drives a resonance, increasing the peak height and narrowing its width. **c, d** Time-dependent variance of particle coordinates at two different beam powers.  $\langle x(t + \tau)x(t) \rangle$  and  $\langle y(t + \tau)y(t) \rangle$  are  $\pi/2$  phase shifted, indicating a tendency toward circular motion. Increasing the power increases the mean frequency of rotation and increases the time constant governing the loss of coherence of the oscillation. Results for linearly polarized beams are inset. **e** Graph showing the product of the position variance with power, as a function of power ( $P\langle x^2 \rangle \nu P$ ), for LP and CP. Error bars show the standard error of the mean. **f** Measured probability distribution of the trapped particle in the transverse plane, scaled by the square root of the beam power for a linearly polarized trap (top row) and a circularly polarized trap (lower row). Variation of this distribution with beam power indicates deviation from thermodynamic equilibrium

**Regime II: stable orbits.** Simple equilibrium conditions for the orbits can be obtained by balancing azimuthal spin forces with viscous drag, and radial centripetal forces with optical gradient forces:

$$\frac{P_o}{\xi^2} = -\frac{r_o f_r(r_o)}{m f_\phi^2(r_o)}, \tag{7a}$$

$$\frac{\Omega_o}{\xi} = \frac{f_r(r_o)}{m f_\phi(r_o)}, \tag{7b}$$

where  $P_o$  is the optical power required to sustain an orbit with radius  $r_o$  for a given viscous drag,  $\xi$ . Taking the linear

approximation for small orbits (e.g.,  $f_i(r) \approx k_i r$ , with  $i = r, \phi$ ) in Eqs. (7, a, b), reproduces the threshold conditions between regimes I and II, Eqs. (5 and 6): the optical power required to zero the imaginary parts of the characteristic frequencies, i.e.,  $\Im(\omega_c(P)) = 0$ , is precisely the power required for centripetal forces to balance gradient forces in the linear approximation. Because the ratio of the azimuthal and radial forces is approximately constant the orbit frequency,  $\Omega_o$ , is also approximately constant and independent of orbit radius and optical power, i.e.,  $\Omega_o \approx \Omega_{thr}$ .

In order for an orbit to be stable and coherent, further conditions must be met. Any change in the orbit radius or frequency should be counteracted by the trap. For instance, a perturbation in the radius will cause a change in the gradient,

azimuthal and centripetal forces that should act to restore the orbit radius. Furthermore, these responses need to be strong enough to constrain thermal fluctuations. The linear stability of the orbits, and their resistance to thermal fluctuations are analyzed in Supplementary Note 4. In summary, we find that for a beam with waist radius  $W_0$ , there are no asymptotically stable orbits with  $r_0 \gtrsim r_{\max} \equiv \sqrt{2/3}W_0$ , which corresponds to a maximum optical power given by Eq. (7a). Furthermore, thermal fluctuations tend to dominate orbits with small radii and a higher optical power ( $P_{\text{orb}} > P_{\text{thr}}$ ) is required for formation of thermally stable, coherent orbits (Supplementary Note 4).

This overall behavior is confirmed experimentally. Figure 1c illustrates the qualitative difference in the transverse motion of the particle between regimes I and II. This is quantified in Fig. 3a, which shows the mean values of the radius of the orbit as a function of optical power. Insets show that the orbit is slightly elliptical and its size suffers hysteresis with respect to the direction of power change. In particular, orbiting appears to survive to lower powers when the power is being decreased. These effects are related to the difference between  $P_{\text{thr}}$ , the power required to destabilize the trap in the linear regime, and  $P_{\text{orb}} > P_{\text{thr}}$ , the power required to form a stable, coherent orbit. At the lowest powers, the mean radii of the particle trajectories are indeed comparable for CP and LP beams. However, they begin to diverge with increasing power; the LP radii decrease and CP increase, in accordance with theory. We note that the non-orbiting trajectories for the linearly polarized beams (black crosses in Fig. 3a) were captured between the orbiting trajectories shown by the blue and green circles, demonstrating the robustness of the orbiting behavior. At higher optical powers than those represented in the graph, centripetal forces exceed gradient forces and the particle is radially ejected from circularly polarized traps.

Mean values for  $x$  and  $y$  trap frequencies ( $\omega_0/2\pi$ ) in LP traps are shown in Fig. 3b and, together with the CP results, they follow the predicted behavior. In regime I, CP and LP traps follow the same power dependence, however in regime II the orbiting frequency remains constant, the exact value depending slightly on the branch of the hysteresis curve. This reflects the observation that the ratio of the radial and azimuthal forces is approximately constant, yielding a constant orbit frequency in Eq. (7b).

Finally, Fig. 3c shows the measured azimuthal force as a function of radius. These data are evaluated by fitting to experimentally measured trajectories as described in the Methods section, below, and in Supplementary Note 5. In particular, the curve was evaluated by fitting experimental PSDs to theoretical profiles (Supplementary Note 3) for regime I, and by applying the orbiting equation, Eq. (7b), in regime II. The validity of the theoretical description is further demonstrated by the close overlap of the data points in the transitional region between axial motion and fully developed orbiting. For comparison, the continuous black line in Fig. 3c shows the theoretical optical force, calculated from Mie theory (Supplementary Note 2). This agreement requires the theoretical optical power to be scaled by a factor of  $\approx 2$ , which includes various uncertainties in the experimental system (Supplementary Note 4 and Supplementary Note 5). The scaling factor cancels in the theoretical evaluation of  $\Omega_{\text{thr}}$ , through Eq. (6), which provides a direct relationship between experiment and theory.

## Discussion

Our experiments vividly demonstrate the mechanical effects of optical spin momentum. Spin forces bias Brownian motion, induce orbits, and ultimately throw a probe particle from an optical trap. These results are completely generic: for a given particle and circularly polarized beam, at a given air pressure,

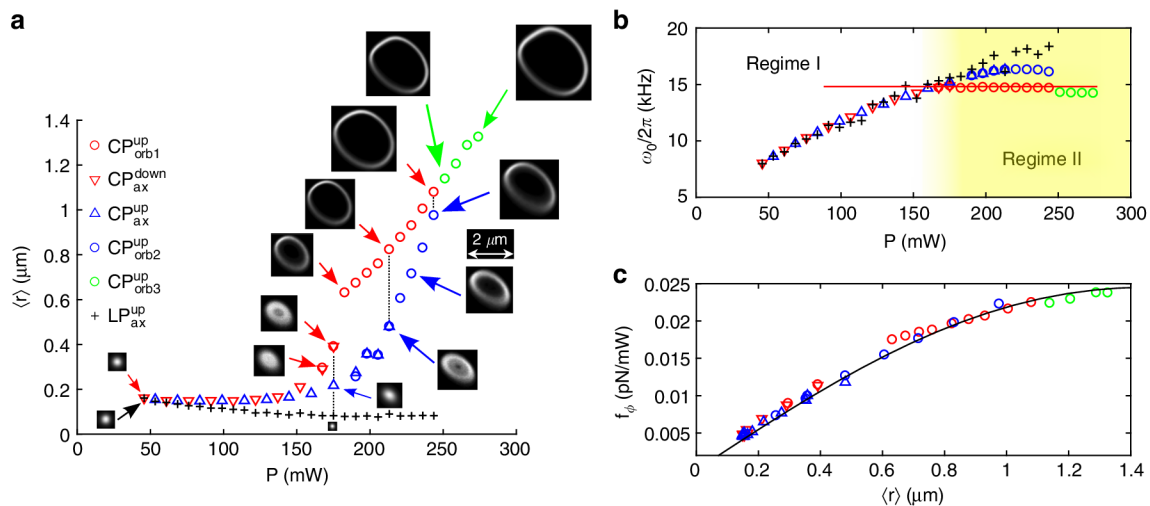


**Fig. 3** Graphical comparison of the key physical quantities in regimes I and II. **a** Mean value of the orbit radius,  $\langle r \rangle$ , as a function of optical power. The insets show the probability density of the particle positions in the lateral  $xy$  plane relative to the given scale bar. Data related to circularly polarized beams (CP) are denoted by  $\circ$ ,  $\Delta$ , and  $\nabla$  for the orbiting regime II.  $\Delta$  and  $\nabla$  symbols correspond to increasing and decreasing optical power, respectively. For comparison data corresponding to parallel linear polarization (LP) are marked by black + signs. The sequence in which the data was acquired is indicated by colors and markers: red circles, red triangles, blue triangles, blue circles, +, and green circles. Overlapping points red circles with red triangle and blue triangles with blue circles illustrate how different calculation methods, used for regime I and II, overlap in the region where the orbiting is not fully developed. **b** Resonant trap frequency  $\omega_0/2\pi$  or orbiting frequency  $\Omega_0/2\pi$  for regime I or II, respectively. The theoretical value from Eq. (7b), is indicated by the horizontal red line. Measured values of  $\xi/m$ , and calculated values of  $f_r/f_\phi$  for a particle of radius 770 nm and density  $2200 \text{ kg m}^{-3}$ . The presented values were determined as the mean value for  $x$  and  $y$  directions from fits to the PSD (Supplementary Note 3) for regime I and from the orbiting equation (Eq. 7b) for regime II (see details in Supplementary Note 5). The black curve shows the theoretical force, obtained from generalized Lorentz Mie theory (Supplementary Note 2). A single scaling parameter has been used (Supplementary Note 5)

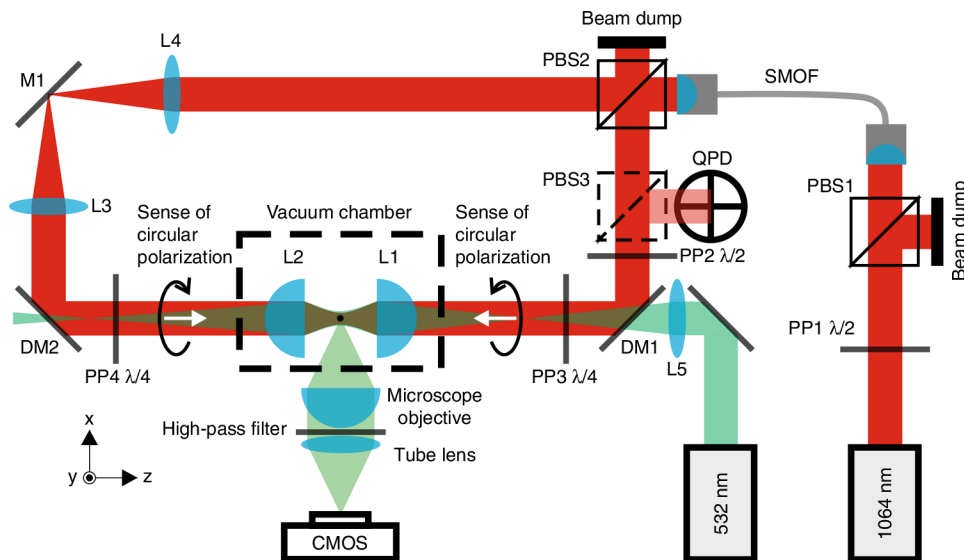


**Fig. 4** Schematic showing the optical set-up. A detailed description is provided in the Methods section

there is always an escape power above which the trap will eject the particle. For fixed optical power, there is also an equivalent pressure beneath which the same thing will happen. The parametric variation of these phenomena is theoretically investigated in Supplementary Note 3. As anticipated, the relative magnitude of the spin force falls off very rapidly for small spheres, vanishing in the small particle limit. As a result the threshold power,  $P_{\text{thr}}$ , increases sharply, as does the threshold orbit frequency,  $\Omega_{\text{thr}}$ . Increasing the beam waist gradually increases  $P_{\text{thr}}$ , but preserves the ratio between spin and gradient forces, leaving  $\Omega_{\text{thr}}$  approximately unchanged. These results show an intriguing possibility. For small spheres, and tightly focused beams, it should be possible to excite very high-frequency orbits with  $\Omega_{\text{thr}} \approx 10^6$  Hz under experimentally accessible conditions. At a pressure of  $\sim 4$  mbar we would expect  $\Omega_{\text{thr}} \approx 10^6$  Hz for a sphere of radius  $a \approx 0.2 \mu\text{m}$  in a diffraction limited beam. Decreasing the pressure further, accentuates the effect considerably.

In addition, this work provides an archetypal example of linearly non-conservative optical vacuum traps. All of the phenomena observed here arise from intrinsic, non-symmetric coupling between motional degrees of freedom. This is expressed in the asymmetry of the stiffness matrix, Eq. (3). For circularly polarized light, this coupling is caused by spin. More generally, asymmetric coupling can be induced by any reduction in symmetry, either of the particle shape, or the trapping field<sup>29</sup>. In viscous media, this results in biased Brownian motion<sup>30</sup>. As we have seen, the consequences in air or weak vacuum are more extreme, as the trapped particle can accumulate momentum, resulting in thermally excited coherent motion. Analogous effects may be expected for non-spherical particles or defective beams.

Finally, these experiments signpost a new research direction. Optical force fields are generally non-conservative, and their structure is derived from internal momentum flows. It is clear that measuring the trajectories of probe particles in vacuum can help us develop our understanding of optical momentum flows in structured light fields as well as the dynamics and thermodynamics associated with motion in potentially complex force fields. Some of these possibilities have previously been described by Berry and Shukla<sup>31,32</sup>. Nevertheless, major unanswered questions persist, especially concerning the details of momentum coupling to matter of varying shape and composition, and to the interplay between thermal fluctuations and some of the dynamical behavior predicted elsewhere.

## Methods

**Experimental set-up.** A schematic of the experimental set-up is provided in Fig. 4. The low noise laser beam from a Prometheus laser (Coherent) working at a wavelength of 1064 nm passes, first, through a polarizing beamsplitter PBS1 and then is coupled to a single mode optical fiber (SMOF) for spatial filtering. The trapping power is controlled by rotation of the half-wave plate, PP1, in front of PBS1. The output of the SMOF is divided into two beams of equal power and orthogonal LP by polarizing beamsplitter PBS2. Lenses L3 and L4 constitute a 1/1 beam expander. Before entering the vacuum chamber, the polarization of one of the beams could be changed from linear to right-hand or left-hand circular (CP) by a quarter-wave plate PP4. The linear polarization of the second beam can be first rotated through an arbitrary angle by half-wave plate, PP2, and subsequently changed from linear to right-hand or left-hand circular polarization by the quarter-wave plate, PP3. In the vacuum chamber, the counter-propagating beams were focused by aspheric lenses L1, L2 (Thorlabs C240TME-C) of focal length 8 mm to create a trap with a beam waist of  $W_0 \approx 2.7 \mu\text{m}$ . Non-porous  $\text{SiO}_2$  microspheres (Bangs Laboratories, diameter  $1.54 \mu\text{m}$ , size CV 10–15%) with negligible absorption were sprayed with a nebulizer (Breuer IH50) into the volume of the optical trap at atmospheric pressure. Prior to spraying, the spheres were suspended in isopropyl alcohol with low particle concentration and the suspension was sonicated in an ultrasonic bath for 15 min to prevent clumping. All subsequent experiments were performed at 4 mbar. The pressure in the trap was measured with 30% accuracy with a Pirani and cold cathode gauge (Pfeiffer PKR 251). For CP measurements, the two counter-propagating beams were circularly polarized with opposite handedness, so that the transverse electric fields of the beams rotate together (Fig. 1a). Using the quarter-wave plates we made comparative measurements with parallel or perpendicularly linearly polarized beams. The same particle was used for all the presented experiments that were performed with optical trapping power varying in the range 45–281 mW.

**Particle tracking.** Motion of the trapped particle was tracked using a quadrant photodetector (InGaAs QPD Hamamatsu G6849). We employed a detection scheme similar to back focal plane interferometry, where the scattered trapping light interferes with the unscattered trapping beam and creates a rotationally non-symmetrical intensity distribution in the plane of QPD<sup>33</sup>. In our case, the trapping beam, propagating from left to right, was used as for the particle tracking at the QPD. While trapping in CP light, after passing through the vacuum chamber the measuring beam is reflected upwards out of the plane of the set-up by the polarizing beamsplitter PBS3. On the other hand, while trapping in LP light, the measuring beam would have been transmitted by PBS3 so PP3 was rotated by  $2^\circ$  from its ideal orientation in order to get a signal on QPD. This allowed us to monitor the motion of the trapped sphere in axial ( $z$ ) and orthogonal horizontal ( $x$ ) and vertical ( $y$ ) directions. The QPD signal was processed by home-made electronics and acquired by NI USB 6351 card at 250 kHz sampling rate. The particle's motion was also tracked from outside the vacuum chamber by a fast CMOS camera (Vision Research Phantom V611) which was triggered to begin recording at the same time as the QPD. The microscope was composed of a microscope objective (MOTIC, Plan Apo,  $100\times/0.55$ , WD 13), tube lens (Thorlabs ACA-254-500A), and a fast CMOS camera (Vision Research Phantom V611). For the purpose of observation, the particle was illuminated by a broad, weak laser beam of wavelength 532 nm, as the camera is more sensitive at this spectral range. The framerate was 200,000 fps for measurements in LP beams, when the particle remains close to the beam axis, and 187,290 fps for measurements of orbiting. The position of the particle in each

frame was obtained with sub-pixel precision by fitting a two-dimensional Gaussian profile to the image<sup>34</sup>. The microscope was calibrated using a calibration grid so the camera recording eventually provided calibrated  $x$  and  $z$  coordinates of the particle trajectory (nm). Finally, the calibration constant relating the QPD signal to displacement in meters was obtained for each power separately by comparing widths of histograms of position obtained by camera (nm) and by QPD (V). This comparison was possible because the camera and QPD recordings were triggered to start simultaneously. As the CMOS camera detects  $x$  and  $z$  axis, we used the same calibration constant for  $x$  and  $y$  axes of QPD.

**Data processing.** Theoretical profiles were fitted to experimentally measured PSDs for LP beams, allowing us to determine the ratio of the drag to the mass of the particle,  $\xi/m$ . This was used as a fixed parameter for the system in analysis of particle motion in CP beams. Resonant trap frequencies,  $\omega_0$  or orbiting frequencies  $\Omega_0$ , were determined from fits to theoretical power spectra and the spin force contribution was obtained from fits to theoretical power spectra in regime I or using Eq. (8) for regime II. Further details are provided in Supplementary Note 5.

### Data availability

The data presented in this article are available from the corresponding author on request.

Received: 19 July 2018 Accepted: 28 November 2018

Published online: 21 December 2018

### References

- Pfeifer, R. N. C., Nieminen, T. A., Heckenberg, N. R. & Rubinsztein-Dunlop, H. Colloquium: momentum of an electromagnetic wave in dielectric media. *Rev. Mod. Phys.* **79**, 1197–2016 (2007).
- Berry, M. V. Optical currents. *J. Opt. A* **11**, 094001 (2009).
- Bekshaev, A., Bliokh, K. Y. & Soskin, M. Internal flows and energy circulation in light beams. *J. Opt.* **13**, 053001 (2011).
- Neugebauer, M., Bauer, T., Aiello, A. & Banzer, P. Measuring the transverse spin density of light. *Phys. Rev. Lett.* **114**, 063901 (2015).
- Antognozzi, M. et al. Direct measurements of the extraordinary optical momentum and transverse spin-dependent force using a nano-cantilever. *Nat. Phys.* **12**, 731–735 (2016).
- Bliokh, K. Y., Bekshaev, A. Y. & Nori, F. Extraordinary momentum and spin in evanescent waves. *Nat. Commun.* **5**, 3300 (2014).
- Liu, L. et al. Three-dimensional measurement of the helicity-dependent forces on a Mie particle. *Phys. Rev. Lett.* **120**, 223901 (2018).
- Bliokh, K. Y., Bekshaev, A. Y. & Nori, F. Dual electromagnetism: helicity, spin, momentum, and angular momentum. *New J. Phys.* **15**, 033026 (2013).
- Bliokh, K. Y. et al. Spin-to-orbital angular momentum conversion in focusing, scattering, and imaging systems. *Opt. Express* **19**, 26132–26149 (2011).
- Jackson, J. *Classical Electrodynamics: Third Edition* (Cambridge university press, 1999).
- Soper, D. *Classical Field Theory* (Dover Publications Inc., 2008).
- Angelsky, O. V. et al. Orbital rotation without orbital angular momentum: mechanical action of the spin part of the internal energy flow in light beams. *Opt. Express* **20**, 3563–3571 (2012).
- Ruffner, D. B. & Grier, D. G. Optical forces and torques in nonuniform beams of light. *Phys. Rev. Lett.* **108**, 173602 (2012).
- Sukhov, S., Kajorndejnukul, V., Naraghi, R. R. & Dogariu, A. Dynamic consequences of optical spin-orbit interaction. *Nat. Photon.* **9**, 809–812 (2015).
- Rodríguez-Fortuno, F. J., Engheta, N., Martínez, A. & Zayats, A. V. Lateral forces on circularly polarizable particles near a surface. *Nat. Commun.* **6**, 8799 (2015).
- Wang, S. B. & Chan, C. T. Lateral optical force on chiral particles near a surface. *Nat. Commun.* **5**, 3307 (2014).
- Magallanes, H. & Brasselet, E. Macroscopic direct observation of optical spin-dependent lateral forces and left-handed torques. *Nat. Photon.* **12**, 461–464 (2018).
- Li, T., Kheifets, S. & Raizen, M. G. Millikelvin cooling of an optically trapped microsphere in vacuum. *Nat. Phys.* **7**, 527–530 (2011).
- Chan, J. et al. Laser cooling of a nanomechanical oscillator into its quantum ground state. *Nature* **478**, 89–92 (2011).
- Millen, J., Fonseca, P. Z. G., Mavrogordatos, T., Monteiro, T. S. & Barker, P. F. Cavity cooling a single charged levitated nanosphere. *Phys. Rev. Lett.* **114**, 123602 (2015).
- Gieseler, J., Spasenovic, M., Novotny, L. & Quidant, R. Nonlinear mode coupling and synchronization of a vacuum-trapped nanoparticle. *Phys. Rev. Lett.* **112**, 103603 (2014).
- Arita, Y., Mazilu, M. & Dholakia, K. Laser-induced rotation and cooling of a trapped microgyroscope in vacuum. *Nat. Commun.* **4**, 2374 (2013).
- Rondin, L. et al. Direct measurement of Kramers turnover with a levitated nanoparticle. *Nat. Nanotech.* **12**, 1130–1133 (2017).
- Millen, J., Deesuan, T., Barker, P. & Anders, J. Nanoscale temperature measurements using non-equilibrium brownian dynamics of a levitated nanosphere. *Nat. Nanotech.* **9**, 425–429 (2014).
- Gieseler, J., Quidant, R., Dellago, C. & Novotny, L. Dynamic relaxation of a levitated nanoparticle from a non-equilibrium steady state. *Nat. Nanotech.* **9**, 358–364 (2014).
- Divitt, S., Rondin, L. & Novotny, L. Cancellation of non-conservative scattering forces in optical traps by counter-propagating beams. *Opt. Lett.* **40**, 1900–1903 (2015).
- Nieminen, T. A., Stilgoe, A. B., Heckenberg, N. R. & Rubinsztein-Dunlop, H. Angular momentum of a strongly focused Gaussian beam. *J. Opt. A* **10**, 115005 (2008).
- Xiao, G., Yang, K., Luo, H., Chen, X. & Xiong, W. Orbital rotation of trapped particle in a transversely misaligned dual-fiber optical trap. *IEEE Phot. J.* **8**, 6100108 (2016).
- Simpson, S. H. & Hanna, S. First-order nonconservative motion of optically trapped nonspherical particles. *Phys. Rev. E* **82**, 031141 (2010).
- Irrera, A. et al. Photonic torque microscopy of the nonconservative force field for optically trapped silicon nanowires. *Nano. Lett.* **16**, 4181–4188 (2016).
- Berry, M. V. & Shukla, P. Physical curl forces: dipole dynamics near optical vortices. *J. Phys. A* **46**, 422001 (2013).
- Berry, M. V. & Shukla, P. Curl force dynamics: Symmetries, chaos and constants of motion. *New J. Phys.* **18**, 063018 (2016).
- Pralle, A., Prummer, M., Florin, E., Stelzer, E. & Hörber, J. Three-dimensional high-resolution particle tracking for optical tweezers by forward scattered light. *Microsc. Res. Tech.* **44**, 378–386 (1999).
- Cheezum, M. K., Walker, W. F. & Guilford, W. H. Quantitative comparison of algorithms for tracking single fluorescent particles. *Biophys. J.* **81**, 2378–2388 (2001).

### Acknowledgements

We thank František Hrubý and Petr Jedlička for technical assistance and Radim Filip for encouraging discussions. This work was supported by project No. GB14-36681G from the Czech Science Agency and LO1212 from the Ministry of Education, Youth, and Sports.

### Author contributions

S.S. suggested the phenomena, provided theoretical analysis, and wrote the article, P.Z. and O.B. designed the experiment, V.S, O.B, P.J, J.K. built up the experimental system, and V.S. collected experimental data, V.S, P.Z, M.S, S.S. analyzed the experimental data and compared with theoretical predictions. All authors assisted with the preparation of the manuscript.


### Additional information

**Supplementary Information** accompanies this paper at <https://doi.org/10.1038/s41467-018-07866-8>.

**Competing interests:** The authors declare no competing interests.

**Reprints and permission** information is available online at <http://npg.nature.com/reprintsandpermissions/>

**Publisher's note:** Springer Nature remains neutral with regard to jurisdictional claims in published maps and institutional affiliations.

 **Open Access** This article is licensed under a Creative Commons Attribution 4.0 International License, which permits use, sharing, adaptation, distribution and reproduction in any medium or format, as long as you give appropriate credit to the original author(s) and the source, provide a link to the Creative Commons license, and indicate if changes were made. The images or other third party material in this article are included in the article's Creative Commons license, unless indicated otherwise in a credit line to the material. If material is not included in the article's Creative Commons license and your intended use is not permitted by statutory regulation or exceeds the permitted use, you will need to obtain permission directly from the copyright holder. To view a copy of this license, visit <http://creativecommons.org/licenses/by/4.0/>.

© The Author(s) 2018

## 4 Optical binding of microparticles in vacuum

More complex system of oscillators can be created by simultaneous trapping of multiple dielectric particles. The trapping light scattered by one particle can modify the trapping light field in location of some other particle, thus modifying the optical forces felt by the second particle. This also works the other way around, the second particle scatters trapping light, thus modifying the optical forces felt by the first particle. If such situation occurs, the two levitated particles become two coupled oscillators in a similar manner two pendulums would be coupled by a spring between them. This phenomenon of coupling mediated by scattered light is usually called *optical binding*, we say that the two particles are optically bound.

While optical binding in water (overdamped regime) was studied extensively [90, 91, 9, 92, 93, 51], systems of optically bound particles in vacuum (underdamped regime) are quiet unexplored. Such systems are believed to be excellent platforms for experimental investigation of as intriguing collective effects as selforganization [94] or synchronization [95]. So far, dynamics of particles trapped in two parallel optical tweezers in vacuum has been investigated [96] and experimentally very challenging trapping of optically bound array trapped inside a hollow core optical fiber was shown [[97]].

### 4.1 Stochastic dynamics of optically bound matter levitated in vacuum

In the presented work, we demonstrate the optical binding between multiple levitated beads trapped in cross-polarized counter-propagating laser beams in vacuum. For two particles we identify normal modes, show the tunability of the interparticle separation and quantify the nonlinear interparticle coupling for various separations. We consider the results necessary preliminary step on the way towards experimental studies of non-classical physics of complex coupled systems like entanglement on mesoscopic level.

I performed the first preliminary experiments with two and three optically bound particles trapped in cross-polarized counter-propagating beams using the experimental setup described in Chapter 2. I observed the collective dynamics similar to that presented in Fig.2 and did the measurement of collective dynamics of three particles presented in Fig.5. I also observed and captured collision of particles mentioned in section D. of the presented paper and performed part of the data processing (particle

position tracking from video and analysis of particle trajectories). I also participated in development of the theoretical models, which arose from cooperation between me, S. Simpson, O. Brzobohatý and M. Šiler.

The first setup mentioned above did not allow us to easily modify the beam parameters for tuning the inter-particle distance as shown in Fig. 3. Also it took unbearably long (typically hours) for two or more particles to reach the trap. So another setup was used for detailed parametric study (description can be found in the following text). It employed spatial light modulator (SLM) for trapping beam shaping. It also employed miniature vacuum chamber fitted between trapping lenses which proved more experimentally convenient in terms of optical path adjustment and speed of loading more particles.





# Stochastic dynamics of optically bound matter levitated in vacuum

VOJTĚCH SVAK, JANA FLAJŠMANOVÁ, LUKÁŠ CHVÁTAL, MARTIN ŠILER, ALEXANDR JONÁŠ, ,  
 JAN JEŽEK, STEPHEN H. SIMPSON, PAVEL ZEMÁNEK, AND OTO BRZBOHATÝ\*

Institute of Scientific Instruments of the CAS. v.v.i., Královopolská 147, 612 64 Brno, Czech Republic

\*Corresponding author: otobrzo@isibrno.cz

Received 6 August 2020; revised 2 November 2020; accepted 13 December 2020 (Doc. ID 404851); published 10 February 2021

Optically levitated nanoparticles in a vacuum offer a light–matter interface with broad and easy tunability of all key system parameters. However, the majority of previously reported experimental achievements in this area have only dealt with a single levitated object. Here, we demonstrate optical binding between multiple levitated objects confined in cross-polarized counter-propagating laser beams in a vacuum. We characterize the level of interparticle interaction, quantify its nonlinearity for various configurations of the system, and demonstrate its broad tunability. Our methodology for quantitative characterization of optically bound structures is supported by an extensive theoretical description and validated by numerical simulations. We believe the presented results represent a step toward the development of a framework of levitated optomechanics of complex coupled systems with a controlled level of coupling nonlinearity for experimental studies including, for example, mesoscopic entanglement.

© 2021 Optical Society of America under the terms of the OSA Open

Access Publishing Agreement

<https://doi.org/10.1364/OPTICA.404851>

## 1. INTRODUCTION

Optical levitation of particles in laser beams propagating in a vacuum was first demonstrated by Arthur Ashkin in his 1976 pioneering work [1]. The technique, referred to as levitated optomechanics, has recently attracted renewed interest owing to its applications in the emerging fields of macroscopic quantum mechanics [2] and stochastic thermodynamics [3]. These activities have been facilitated by the development of two strategies for cooling the center-of-mass motion of optically levitated, mesoscopic particles toward the quantum regime. The first one, independently proposed by three groups in 2010 [4–6], relies on coupling the trapped particle to an optical cavity, with the resulting efforts culminating in the very recent demonstration of ground-state cooling by Delić *et al.* [7]. The second approach is based on active feedback control [8–10], and is well suited to studying elementary statistical mechanics [11]. In particular, levitated optomechanics permits detailed studies of the Brownian motion of individual particles controllably coupled to the environment, whose positions can be tracked with high temporal and spatial resolution. This approach has yielded new insights into microscale thermodynamic processes taking place in the underdamped regime [3]; e.g., the first observation of Kramers turnover [11] or the emergence of nonconservative instabilities in thermally excited particle motion [12].

Extending levitated optomechanics to systems with multiple mechanical degrees of freedom offers new opportunities in research fields ranging from the quantum entanglement of “macroscopic” objects of increasing mass and size [13] to the statistical

mechanics of coupled systems. Mechanisms for entangling levitated nanoparticles via nonlinear coupling have been considered theoretically [14,15], and experiments involving the selective cooling of individual phonon modes and redistribution of energy between nonlinearly coupled oscillators (in analogy with the famed Fermi–Pasta–Ulam–Tsingou problem [16]) can be envisaged [17,18].

When a collection of microobjects is immersed in an incident optical field, multiple light scattering events result in mutually coupled optical forces between the illuminated objects that depend on the configuration of the system as a whole. These optical binding forces [19] then drive self-organization of various micro- and nanoassemblies [19–23], dependent on the shape [24–26], material [27–29], and internal structure [30] of the objects comprising the ensemble, as well as on the polarization [31,32] and spatial distribution [33,34] of the incident optical field. Since the optical binding forces arise due to the deflection of momentum carried by the scattered light, the law of action and reaction between optically bound objects does not need to be satisfied [35]. As a consequence, optical binding forces have nonconservative components [36], which dramatically influence the motion of individual illuminated particles in the underdamped regime [12], while optically bound systems immersed in viscous liquids at low Reynolds numbers are known to display a rich variety of nonequilibrium dynamic behaviors [35,37,38]. Previous experimental studies of optical binding dynamics have most commonly been conducted at overdamped conditions; to date, only two studies have considered the behavior of optically bound matter in underdamped environments [39,40].

In particular, Bykov *et al.* reported long-range optical binding of several levitated microparticles mediated by intermodal scattering and interference inside the evacuated core of a hollow-core photonic crystal fiber [39], while Arita *et al.* demonstrated optical binding between two rotating chiral microparticles confined in a vacuum in independent circularly polarized optical traps [40].

In this paper, we investigate optical binding between multiple silica particles with identical submicron diameters confined in a vacuum using two noninterfering, counter-propagating Gaussian beams with mutually orthogonal linear polarizations. In this highly symmetrical particle–light field configuration, the motion of the illuminated particles is approximately conservative [41]. Our previous studies that were carried out with such an experimental system in the overdamped regime showed the formation of extended arrays of optically bound particles [42], which themselves exhibited exotic optical effects [43]. Here, we concentrate on the collective dynamics of optically bound matter in the underdamped regime at low ambient pressures. We observe the appearance of normal modes of vibration in the thermally driven particle motion, reconstruct the optical binding forces from experimentally recorded particle trajectories, quantify the level of nonlinear coupling between the particles, and investigate the influence of the beam intensity profiles on the particle dynamics. We compare our experimental findings with the predictions of a quantitative theoretical model of particle interaction via optical and hydrodynamic forces, and observe a very good agreement.

## 2. METHODS

### A. Experimental Setup

To optically confine the studied particles inside a vacuum chamber and characterize their optical binding, we used a source of infrared laser light operating at the vacuum wavelength of 1064 nm with low intensity noise (Mephisto, Coherent Inc., Santa Clara, CA, USA). For the laser beam transformation, we used Thorlabs achromatic doublets with antireflection coating ACN254-XXX-C (L1–L6), dielectric mirrors PF10-03 (M1–M3), and aspheric lenses C240TME-C with antireflection coating (AS1). A collimated Gaussian beam from the laser was first expanded by a telescope formed by lenses L1 ( $f_1 = 150$  mm) and L2 ( $f_2 = 300$  mm) and projected on a spatial light modulator (SLM) (LCOS X10468-07, Hamamatsu Photonics K.K., Hamamatsu City, Japan). Phase mask encoded at the SLM diffracted the beam into the  $\pm 1$  diffraction orders that were used to generate the two counter-propagating trapping beams; the zeroth and higher orders were blocked by a stop placed in the focal plane of lens L3 ( $f_3 = 400$  mm). The two transmitted 1<sup>st</sup>-order beams were reflected from prisms P1 and collimated by lenses L4 ( $f_4 = 200$  mm). These lenses formed telescopes with the lens L3, projecting the SLM plane on the mirrors M2. Telescopes consisting of lenses L5 ( $f_5 = 100$  mm) and L6 ( $f_6 = 150$  mm) then imaged the SLM plane onto the back focal planes of aspheric lenses AS1 ( $f = 8$  mm, maximal NA = 0.5) that focused the two trapping beams into the vacuum chamber. The polarization of the beams was controlled with a pair of half-wave plates to form a cross-polarized dual-beam trap [12,33]. The focal planes of the two beams created in the trapping region by aspheric lenses AS1 were slightly displaced from each other along the beam propagation direction  $z$  (by approximately 5  $\mu\text{m}$ ; see red lines in Fig. 1) to increase the axial trapping stability [20]. The beam waist radii

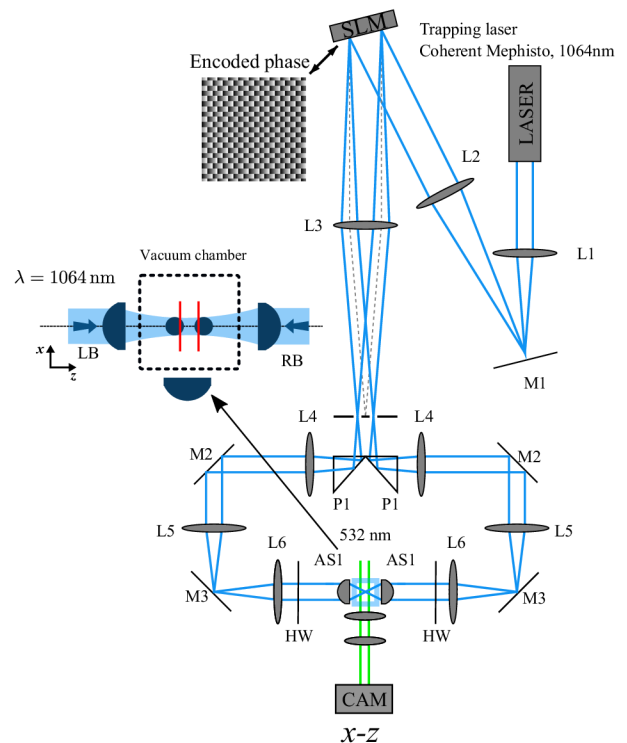


**Fig. 1.** Experimental setup of the dual-beam optical trap with two orthogonal or parallel linearly polarized counter-propagating laser beams (LB and RB) controlled by a half-waveplate (HW). Optically bound particles in the vacuum chamber are observed using a microscope oriented along the  $y$  axis, perpendicularly to the beams' axes.

$w_0$  in the trapping region could be adjusted in the range between 1–3  $\mu\text{m}$  by controlling the area of the diffraction grating imposed upon the SLM.

Silica ( $\text{SiO}_2$ ) particles (mean diameter  $d = 600$  nm, standard deviation of the particle size distribution 12%, Bangs Laboratories Inc., Fishers, IN, USA) were dispersed in isopropyl alcohol and after  $\sim 20$  min sonication of the suspension, droplets containing the particles were sprayed into the trapping region in the vacuum chamber employing an ultrasonic nebulizer (Beurer IH 50).

To enable position tracking of the optically trapped and bound particles, the sample was illuminated by an independent laser beam (Prometheus, vacuum wavelength 532 nm, Coherent Inc., Santa Clara, CA, USA) propagating along the  $y$  direction perpendicular to the imaging  $x - z$  plane. Large beam waist radius of  $w_0 = 40$   $\mu\text{m}$  and low power (approximately 5 mW at the sample) of the green illuminating beam ensured its negligible contribution to the net optical force acting on the particles. To record the motion of the particles in the  $x - z$  plane, a fast CMOS camera (Phantom V611, Vision Research, Inc., Wayne, NJ USA) was oriented along the  $y$  direction; its exposure time was set to 1  $\mu\text{s}$  and the frame rate was 300 kHz. Typically, we recorded at least 100,000 frames from the studied optically bound structures to obtain sufficiently long trajectories for the analysis of their motional dynamics.

The off-line tracking of the particle position from the high-speed video recordings was based on the determination of symmetries in the particle images [44]. Briefly, since a spherical particle produces an azimuthally invariant image, we used the shift property of the Fourier transform and looked for the best horizontal and vertical symmetries in the particle image, which

provided us with the information about the in-plane  $x$  and  $z$  coordinates with the spatial resolution of  $\sim 10$  nm and the temporal resolution of  $\sim 3.3$   $\mu$ s.

## B. Theoretical Model of Optically Bound Structures with Hydrodynamic Interactions

The detailed derivation of our theoretical model is presented in Section 1 of [Supplement 1](#). Here, we summarize the most important elements of the model and its analytical results we directly used in the data processing and analysis.

The system of  $N$  identical optically trapped and bound particles subject to hydrodynamic forces is described by the following set of Langevin equations in the frequency domain,

$$-m\omega^2 \mathbf{I} \mathbf{Z} + i\omega \mathbf{\Xi} \mathbf{Z} + \mathbf{K} \mathbf{Z} = \mathbf{f}^{\perp}. \quad (1)$$

Here,  $\mathbf{Z} = (Z_1, \dots, Z_N)^T$  is the spectral representation of particle displacement coordinates,  $\mathbf{K}$  is a symmetric ( $N \times N$ ) matrix representing generalized stiffness of the optical force field acting on the system, and  $\mathbf{\Xi}$  is the symmetric ( $N \times N$ ) friction matrix, including hydrodynamic coupling between the particles. The stochastic Langevin forces  $\mathbf{f}^{\perp}$  are normalized as

$$\begin{aligned} \langle \mathbf{f}^{\perp}(\omega) \rangle &= 0, \\ \langle \mathbf{f}^{\perp}(\omega) \otimes \mathbf{f}^{\perp}(\omega') \rangle &= 2k_B T \mathbf{\Xi} \delta(\omega - \omega'). \end{aligned} \quad (2)$$

In the absence of hydrodynamic coupling, the thermal motion of a collection of optically bound spheres can be accurately described by conventional normal mode analysis. At this level of description, the normal modes of the system, given by the eigenvectors  $\mathbf{v}_i^{(0)}$  of the stiffness matrix,  $\mathbf{K}$ , represent a set of  $N$  independent harmonic oscillators. Each of these oscillators has a distinct resonant frequency determined by the respective eigenvalue  $\lambda_i^K$  of  $\mathbf{K}$  and experiences identical viscous damping  $\xi_0 = 6\pi\mu a$ , corresponding to the Stokes viscous drag coefficient of a spherical particle with radius  $a$  moving in a fluid with viscosity  $\mu$ .

The presence of hydrodynamic interactions modifies the form of the normal modes and their damping, so that each quasi-normal mode has now a different effective damping coefficient associated with it. To approximate these effects, we introduce hydrodynamic coupling as a perturbation in the small parameter  $\epsilon = a/r$ , where  $r$  is the mean separation between the spheres, and evaluate all relevant quantities to first order in  $\epsilon$ . This analysis is described in detail in [Supplement 1](#), Section 1.3. To the first order, the quasi-normal modes are given by the eigenvectors  $\mathbf{v}_i \approx \mathbf{v}_i^{(0)} + \epsilon \mathbf{v}_i^{(1)}$  of the modified stiffness matrix of the hydrodynamically coupled system, which depends on the friction matrix, and the resonant frequency of mode  $i$  is

$$\omega_{c,i} = \sqrt{\frac{\lambda_i^K}{m} - \frac{(1 + \epsilon c_i)^2 \xi_0^2}{4m^2}} + i \frac{(1 + \epsilon c_i) \xi_0}{2m}. \quad (3)$$

The power spectral density (PSD) for mode  $i$  is

$$\langle A_i(\omega) A_i^*(\omega) \rangle = \frac{2k_B T \xi_0 (1 + \epsilon c_i)}{m^2 (\omega^2 - \omega_{c,i}^2) (\omega^2 - (\omega_{c,i}^*)^2)}. \quad (4)$$

The PSD acquires a maximum value of

**Table 1. Solving the Case of Two Spheres**

$i$	$\lambda_i^K$	$\mathbf{v}_i^{(0)}$	$\mathbf{v}_i^{(1)}$	$c_i$
1	$k$	$\frac{1}{\sqrt{2}}(1, 1)$	–	$-\frac{3}{2}$
2	$k + 2b$	$\frac{1}{\sqrt{2}}(1, -1)$	–	$+\frac{3}{2}$

**Table 2. Solving the Case of Three Spheres**

$i$	$\lambda_i^K$	$\mathbf{v}_i^{(0)}$	$\mathbf{v}_i^{(1)}$	$c_i$
1	$k$	$\frac{1}{\sqrt{3}}(1, 1, 1)$	$-\frac{i\omega\xi_0}{3\sqrt{2}b} \mathbf{v}_3^{(0)}$	–2
2	$k + b$	$\frac{1}{\sqrt{2}}(1, 0, -1)$	0	0
3	$k + 3b$	$\frac{1}{\sqrt{6}}(1, -2, 1)$	$\frac{i\omega\xi_0}{3\sqrt{2}b} \mathbf{v}_1^{(0)}$	+2

$$\begin{aligned} \langle A_i(\omega) A_i^*(\omega) \rangle_{\max} &= \frac{2k_B T}{\left( \frac{\lambda_i^K}{m} - \frac{(1 + \epsilon c_i)^2 \xi_0^2}{4m^2} \right) (1 + \epsilon c_i) \xi_0} \\ &\approx \frac{2k_B T m}{\lambda_i^K (1 + \epsilon c_i) \xi_0} \end{aligned} \quad (5)$$

for  $\omega \approx \Re(\omega_{c,i})$ .

As described in Section 1.4 of the [Supplement 1](#), the stiffness matrix  $\mathbf{K}$  for a quasi-linear chain of optically bound spheres is approximated using a simple mass-and-spring type model, with each sphere interacting only with its nearest neighbors. In this approximation, each sphere feels the effects of an external optical trapping potential characterised by a stiffness  $k$ , and it is also subject to a harmonic binding force, characterized by an effective stiffness  $b$ . Hydrodynamic coupling between the neighboring spheres is then modeled using the Oseen tensor (see Section 1.5 of [Supplement 1](#)). In Tables 1–3, we provide the eigenvalues  $\lambda_i^K$  of the stiffness matrix  $\mathbf{K}$ , corresponding eigenvectors  $\mathbf{v}_i^{(0)}$  of  $\mathbf{K}$  representing the normal modes of a system without hydrodynamic coupling, first-order corrections  $\mathbf{v}_i^{(1)}$  to the eigenvectors of the quasi-normal modes of a hydrodynamically coupled system, as well as the correction factors  $c_i$  that modify the effective modal friction, for 2, 3, and 4 identical interacting spheres. These quantities are expressed in terms of the stiffness coefficients  $k$  and  $b$ , and the Stokes drag coefficient  $\xi_0$ . The case of two spheres can be solved exactly, without the use of perturbation, as shown in Table 1. The only remaining assumption is the use of the Oseen tensor. Specifically, oscillatory dynamics of two elastically and hydrodynamically coupled spheres can be fully characterized by two normal modes: the center-of-mass (COM) mode ( $i = 1$ ), in which the two particles oscillate in phase within the external trapping potential while their separation distance remains constant, and the breathing (BR) mode ( $i = 2$ ), in which the particles oscillate out-of-phase, so that the system's center of mass does not move but the particle separation distance periodically changes [45]. Tables 2 and 3 show information for three and four spheres, respectively.

## C. Determination of Interparticle and External Forces and Trapping Stiffness from Particles' Trajectories

To determine the spatial profiles of interparticle forces from the experimentally recorded particle positions, we first calculated the acceleration of breathing-mode oscillations along the actual mode trajectory, using numerical differentiation of the particle separation distance  $\Delta z(t) = [z_2^a(t) - z_1^a(t)]$ , where  $z_1^a, z_2^a$  are the absolute coordinates of the particles [see Fig. 2(a)]. Applying

**Table 3. Solving the Case of Four Spheres<sup>a</sup>**

$i$	$\lambda_i^K$	$\mathbf{v}_i^{(0)}$	$\mathbf{v}_i^{(1)}$	$c_i$
1	$k$	$\frac{1}{2}(1, 1, 1)$	$-\frac{3i\omega\xi_0}{8b}\mathbf{v}_3^{(0)}$	$\approx -2.25$
2	$k + (1 + \gamma)b$	$\frac{1}{2\sqrt{1+\gamma}}(1, -\gamma, \gamma, -1)$	$-\frac{3i\omega\xi_0}{16b}\mathbf{v}_4^{(0)}$	$\approx -0.84$
3	$k + 2b$	$\frac{1}{2}(1, -1, -1, 1)$	$\frac{3i\omega\xi_0}{8b}\mathbf{v}_1^{(0)}$	$\approx +0.75$
4	$k + (1 + \delta)b$	$\frac{1}{2\sqrt{1+\delta}}(1, -\delta, \delta, -1)$	$\frac{3i\omega\xi_0}{16b}\mathbf{v}_2^{(0)}$	$\approx +2.34$

<sup>a</sup>Note: Here,  $\gamma = (1 - \sqrt{2}) < 0$  and  $\delta = (1 + \sqrt{2}) > 0$ .

Newton's second law, we then obtained the averaged net interparticle force along the  $z$  axis as  $f_{z;21}^{\text{net}}(\Delta z) = m \langle \Delta \ddot{z}(t) \rangle_{[\Delta z, \Delta z + \delta z]}$ , where  $\Delta \ddot{z}(t)$  is the breathing-mode acceleration and the operator  $\langle \rangle_{[\Delta z, \Delta z + \delta z]}$  denotes averaging over all values of its argument observed for particle separation distances lying within the interval  $[\Delta z, \Delta z + \delta z]$ . This averaging procedure was applied within equally sized adjacent bins of width  $\delta z \ll \langle \Delta z \rangle$  covering the relevant range of  $\Delta z$  ( $\langle \Delta z \rangle$  represents the mean separation between the particles), resulting in the profile of  $f_{z;21}^{\text{net}}(\Delta z)$  at a series of discrete values of  $\Delta z$ . Generally,  $f_{z;21}^{\text{net}}(\Delta z)$  contains deterministic contributions from the optical and viscous forces and a random contribution from the stochastic thermal force [40,45]. However, the averaged modal viscous drag  $\xi \langle \Delta \dot{z}(t) \rangle_{[\Delta z, \Delta z + \delta z]}$ , where  $\xi$  is the coefficient of effective modal viscous friction (see Supplement 1 for details), is zero for all  $\Delta z$ , as during their motion, the particles are equally likely to be in the configuration with a given value of  $\Delta z$  with a positive and negative modal velocity  $\Delta \dot{z}(t)$  of the same magnitude. Similarly, the averaged modal Langevin thermal force  $\langle \Delta f_{z;21}^{\text{L}}(\Delta z) \rangle_{[\Delta z, \Delta z + \delta z]} = 0$  for all  $\Delta z$ . These assertions are rigorously true for a system in thermal equilibrium; hence, the fact they hold for the experimentally observed modal trajectories indicates we operated at near-equilibrium conditions. Since the viscous and thermal forces average out,  $f_{z;21}^{\text{net}}(\Delta z)$  directly represents the all-optical interparticle force  $f_{z;21}(\Delta z)$ . Using an analogical procedure, we determined the spatial profiles of the external optical trapping force as  $f_{z;ext}^{\text{net}}(\bar{z}) = m \langle \ddot{z}(t) \rangle_{[\bar{z}, \bar{z} + \delta z]}$ , where  $\bar{z}(t) = [z_2^a(t) + z_1^a(t)]$  and the operator  $\langle \rangle_{[\bar{z}, \bar{z} + \delta z]}$  denotes averaging over all values of its argument observed for particle separation distances lying within the interval  $[\bar{z}, \bar{z} + \delta z]$ .

The stiffnesses  $k$  of the external trapping potential and  $B$ ,  $B^{\text{sin}}$  of the interparticle potential, presented in Fig. 3(e) as functions of the mean particle separation distance  $\langle \Delta z \rangle$ , were determined from the experimental data by two independent methods:

1. The spatial profiles of the interparticle optical forces,  $f_{z;21}^{\text{net}}(\Delta z)$ , were fitted with Eq. (8) to obtain the values of  $B$ ,  $B^{\text{sin}}$  [using also Eq. (9) for  $B^{\text{sin}}$ ], whereas the values of  $k$  were determined from the slopes of the spatial profiles of the external optical trapping forces,  $f_{z;ext}^{\text{net}}(\bar{z})$  [symbols  $\circ$  in Fig. 3(e)].
2. Power spectral densities of experimental modal trajectories were first fitted with Eq. (4) to extract the mode resonant frequencies,  $\omega_{\text{COM}}^{x,z}$ ,  $\omega_{\text{BR}}^{x,z}$  and subsequently, the values of  $k$  and  $B$  were determined using Eqs. (6) and (7) and the known mass of the used particles [symbols  $\times$  in Fig. 3(e)].

### 3. RESULTS AND DISCUSSION

#### A. Modification of Optical Trapping Potential due to Light Scattering and Interference

In our optical binding experiments, we used the trapping geometry with two horizontal, counter-propagating laser beams with wave vectors  $\mathbf{k}$ , laterally overlapping in a vacuum chamber so that the beam axes were aligned along the same line [33] [see Figs. 1 and 2(a) for illustration]. As the strength of transverse optical trapping in the  $x - y$  plane is significantly higher than the axial trapping strength along the  $z$  direction, the trapped particles tend to migrate to the common axis of the two beams and form a quasi one-dimensional (1D) structure oriented along the  $z$  axis [20–22]. Figure 2(a) illustrates how the scattered photons modify the distribution of light intensity in the simplest case of two optically trapped particles. For each of the two counter-propagating incident beams, the light scattered in the beam propagation direction denoted by  $\mathbf{k}$  locally increases its optical intensity, whereas the backscattered wave interferes with the corresponding co-polarized incident beam, creating a weak standing wave along the optical axis [42].

In contrast to previous work on optical levitation of nanoparticles in a stationary, multistable optical trapping potential with an oscillatory standing wave component [46], optically bound nanoparticles in our experiments did not feel any preexisting, static periodic potential landscape. Instead, modulation of the instantaneous trapping potential sensed by a given particle dynamically changed with the changing positions of the other simultaneously illuminated particle (or particles). This dependence of the trapping potential on the positions of individual illuminated particles then resulted in coupling of the particles' motion and in their collective dynamical response. Since the modulation depth of the optical interference field produced by backscattering was rather low, the thermally driven particles could frequently hop between different trapping positions and, thus, sampled the net anharmonic trapping potential containing multiple potential wells [see inset in Fig. 2(b) for illustration].

#### B. Linearly Coupled Harmonic Oscillators

As discussed in detail in Section 1 of Supplement 1 and summarized in the Methods section of this paper, a system of  $N$  optically and hydrodynamically interacting particles moving in an external optical trapping potential can be described as a set of  $N$ -coupled damped harmonic oscillators. With an appropriate coordinate transformation, this set can be represented by an equivalent system of  $N$ -uncoupled linear oscillators, whose resonant frequencies define the normal modes of the system. For two coupled particles, oscillatory dynamics can be fully characterized in terms of the COM and BR normal modes. Along the  $z$  axis, the transformations from the absolute positions of the particles  $z_1^a$ ,  $z_2^a$  to the normal-mode coordinates  $z_{\text{COM}}$ ,  $z_{\text{BR}}$ , with the corresponding resonant frequencies  $\omega_{\text{COM}}^z$ ,  $\omega_{\text{BR}}^z$ , read as (see the Methods section and Sections 1.4 and 1.6 in Supplement 1 for details):

$$z_{\text{COM}} = (z_1^a + z_2^a) / \sqrt{2},$$

$$(\omega_{\text{COM}}^z)^2 = \frac{k}{m} \left\{ 1 - \frac{[1 - 3a / (2(\Delta z))]^2 \xi_0^2}{4mk} \right\} \approx \frac{k}{m}, \quad (6)$$

$$z_{\text{BR}} = (z_2^a - z_1^a - \langle \Delta z \rangle) / \sqrt{2},$$

$$(\omega_{\text{BR}}^z)^2 = \frac{(k + 2b)}{m} \left\{ 1 - \frac{[1 + 3a/(2\langle \Delta z \rangle)]^2 \xi_0^2}{4mk} \right\} \approx \frac{k + 2b}{m}. \quad (7)$$

Here,  $m$  is the particle mass,  $a$  is the particle radius,  $k$  is the stiffness of the external optical trapping potential created by the two counter-propagating beams,  $b$  is the effective stiffness of the binding interaction,  $\langle \Delta z \rangle$  is the mean separation between the particles, and  $\xi_0 = 6\pi\mu a$  is the particle's viscous drag coefficient, with  $\mu$  being the viscosity of the surrounding fluid. Similar formulas hold along the  $x$  axis, with  $\langle \Delta x \rangle = 0$  in the expression for  $x_{\text{BR}}$ , and  $k$  and  $b$  replaced with their transverse counterparts. As we operate in the underdamped regime with the damping ratio  $\xi_0/\sqrt{4mk} \ll 1$ , the normal-mode resonant frequencies,  $\omega_{\text{COM}}^{x,z}$ ,  $\omega_{\text{BR}}^{x,z}$ , are approximately independent of the viscous friction [40].

Figures 2(c) and 2(d) show representative sequences of video frames recorded from two trapped, coupled particles in independent experimental runs. Depending on the actual initial conditions (particle position and velocity) at the time of entering the trap, the particles were observed to oscillate either in phase in the COM mode [see Fig. 2(c)] or out of phase in the BR mode [see Fig. 2(d)]. In general, the thermally driven motion of two coupled particles is a linear combination of the COM and BR normal modes with different relative weights. This notion can be illustrated by the power spectral densities (PSDs) of particle positions calculated from the particle trajectories  $[x_1^a(t), z_1^a(t)]$  and  $[x_2^a(t), z_2^a(t)]$  recorded in the  $x - z$  plane. As shown in Fig. 2(e), the position PSDs of both particles 1 and 2 along the  $x$  and  $z$  directions feature distinct peaks corresponding to  $\omega_{\text{COM}}^x/2\pi$  ( $\omega_{\text{COM}}^z/2\pi$ ) and  $\omega_{\text{BR}}^x/2\pi$  ( $\omega_{\text{BR}}^z/2\pi$ ). The differences between the transverse ( $x$ ) and axial ( $z$ ) values of the mode resonant frequencies stem from the different values of  $k$  and  $b$  along these two directions [22]. Upon carrying out the coordinate transformations indicated in Eqs. (6) and (7), the two normal modes can be separated, as verified by the PSDs of  $(x_{\text{COM}}, z_{\text{COM}})$  and  $(x_{\text{BR}}, z_{\text{BR}})$  plotted in Fig. 2(f).

The resonant frequency  $\omega_{\text{BR}}^z$  of the axial breathing mode reflects the overall optical interparticle force characterized by the spring constants  $k$  of the external optical potential and  $b$  of the optical binding interaction [see Eq. (7)]. To determine the profile of this force from the experimental data, we first calculated the acceleration of breathing-mode oscillations along the actual mode trajectory, using numerical differentiation of the particle separation distance  $\Delta z(t) = [z_2^a(t) - z_1^a(t)]$ , and subsequently obtained the averaged net interparticle force along the  $z$  axis as  $f_{z;21}^{\text{net}}(\Delta z) = m \langle \Delta \ddot{z}(t) \rangle_{[\Delta z, \Delta z + \delta z]}$  (see the Methods section for details). Since the hydrodynamic and thermal forces average out,  $f_{z;21}^{\text{net}}(\Delta z)$  directly represents the all-optical axial interparticle force  $f_{z;21}(\Delta z)$ . Figure 2(b) compares the experimentally determined interparticle force,  $f_{z;21}(\Delta z)$  (blue line), with its theoretical counterpart  $f_{z;21}^{\text{th}}(\Delta z) = (f_{z;2} - f_{z;1})$  (black line), calculated as the difference of the axial optical forces  $f_{z;2}$ ,  $f_{z;1}$  acting on the two illuminated, optically bound particles. For the actual experimental values of system parameters, the model based on the multiple-scattering Mie theory [42,47] agrees very well with the experiments. A similar conclusion applies to the experimental (orange line) and theoretical (black line) interparticle potentials  $U_{z;21}(\Delta z)$ , calculated by the integration of the corresponding forces as  $U_{z;21}(\Delta z) = - \int f_{z;21}(\Delta z) d\Delta z$ .

## C. Non-linearly Coupled Particles

Within the experimentally relevant range of  $\Delta z$ , the axial optical interparticle potential resembles a harmonic potential well with a superimposed sinusoidal modulation [see the inset in Fig. 2(b)]. Consequently, the associated axial optical interparticle force  $f_{z;21}(\Delta z)$  is a superposition of a linear term and a nonlinear oscillatory component, so

$$f_{z;21}(\Delta z) = -B(\Delta z - \langle \Delta z \rangle) - \alpha \sin(4\pi[\Delta z - \langle \Delta z \rangle]/\lambda). \quad (8)$$

Here,  $B$  is the stiffness (spring constant) of the harmonic part of the force, and  $\alpha$  describes the magnitude of the oscillating optical binding force with a spatial period of  $\lambda/2$ , arising due to interference of the incident and backscattered light [42,48]. Depending on the incident light power, two qualitatively different types of the trapped particles' behavior can be observed. For low light powers, the depth of the secondary optical traps created due to the sinusoidal modulation of the harmonic potential background is below the thermal energy  $k_B T$ , and these traps cannot stably confine the particles subject to stochastic thermal forces. Thus, the modulation has a negligible impact on the particles' axial motion, which is determined primarily by the harmonic part of the interparticle force associated with the constant stiffness  $B$ . In this case, the resonant frequency of the axial breathing mode given by Eq. (7) is  $\omega_{\text{BR}}^z = \sqrt{(k + 2b)/m} = \sqrt{B/m}$ . On the other hand, for sufficiently high light powers, the secondary traps deepen and additional stable particle configurations appear at separation distances  $\Delta z$ , for which  $f_{z;21}(\Delta z) = 0$  and  $(df_{z;21}/d\Delta z) < 0$ . Because they are established by both the linear and oscillating part of the axial interparticle force, these secondary equilibria are characterized by a higher stiffness of confinement. For small deviations from the equilibrium configuration corresponding to  $\Delta z = \langle \Delta z \rangle$ , the sine term in Eq. (8) can be linearized using Taylor series expansion, yielding an effective stiffness,

$$B^{\text{sin}} \approx B + 4\pi\alpha/\lambda, \quad (9)$$

which determines the value of  $\omega_{\text{BR}}^{z,\text{sin}} = \sqrt{(k + 2b^{\text{sin}})/m} = \sqrt{B^{\text{sin}}/m}$ . At intermediate light powers, the particle confinement in the secondary optical traps is transient and the thermally driven particles can effectively sample the whole multistable anharmonic potential landscape. Consequently, particles' motion displays characteristic frequencies corresponding to both  $B$  and  $B^{\text{sin}}$ , reflecting the nonlinear character of the net interparticle force (8) (see Section 2.B of Supplement 1 for details).

The spatial arrangement and motional dynamics of optically trapped and bound particles strongly depend on the distribution of light intensity of the illuminating beams. As illustrated in Fig. 3(a), the interparticle separation distance can be sensitively and reversibly tuned by changing the beam waist radius  $w_0$  [34]. This behavior can be intuitively explained in terms of the interplay between the optical binding and trapping forces. Specifically, the particles coupled by optical springs with stiffness  $b$  are simultaneously subject to the trapping forces of the external optical potential with stiffness  $k$ , which tend to push the particles together [20,45]. Hence, the interparticle springs are, in effect, always partially compressed (see Supplement 1, Section 1.4, for details). For larger beam waists, the stiffness of the external trapping potential—and, thus, the magnitude of the trapping forces—is reduced and the interparticle springs expand toward their relaxed length.

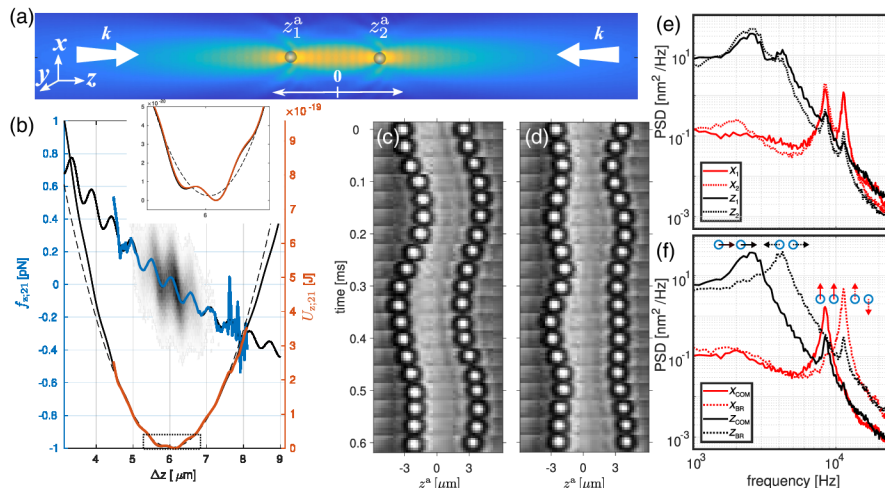


**Fig. 2.** Optical binding of two identical particles confined at a low ambient pressure in cross-polarized, counter-propagating trapping beams. (a) Spatial distribution of optical intensity modified by light scattering from the two optically bound silica particles with nominal diameter  $d = 600$  nm and refractive index  $n = 1.45$ , located on the beam axis at  $z_1^a, z_2^a$ . (b) Comparison of the experimental interparticle force  $f_{z;21}$  (blue line) and potential  $U_{z;21}$  (orange line) with their theoretical counterparts (solid black lines of corresponding shapes) plotted as a function of the interparticle distance  $\Delta z = z_2^a - z_1^a$ . For reference, a parabolic fit to the experimental potential is plotted using a dashed black line. The grayscale-colored 2D histogram visualizes the full distribution of the experimental interparticle forces  $m\Delta\ddot{z}(t)$ . The inset illustrates a weak sinusoidal modulation of the potential near its minimum. (c) Sequence of video frames showing oscillation of the bound particles in the center-of-mass (COM) mode. (d) Sequence of video frames showing oscillation of the bound particles in the breathing (BR) mode. (e) Experimental power spectral densities (PSDs) of  $(x_1^a, z_1^a)$  and  $(x_2^a, z_2^a)$  determined for individual bound particles 1 and 2. (f) Experimental PSDs of  $(x_{\text{COM}}, z_{\text{COM}})$  and  $(x_{\text{BR}}, z_{\text{BR}})$  determined for COM and BR normal modes. Directions of motion of individual particles in the modes are illustrated by blue circles with arrows. Experimental parameters:  $w_0 = 1.95$   $\mu\text{m}$ ,  $P = 70$  mW in both beams.

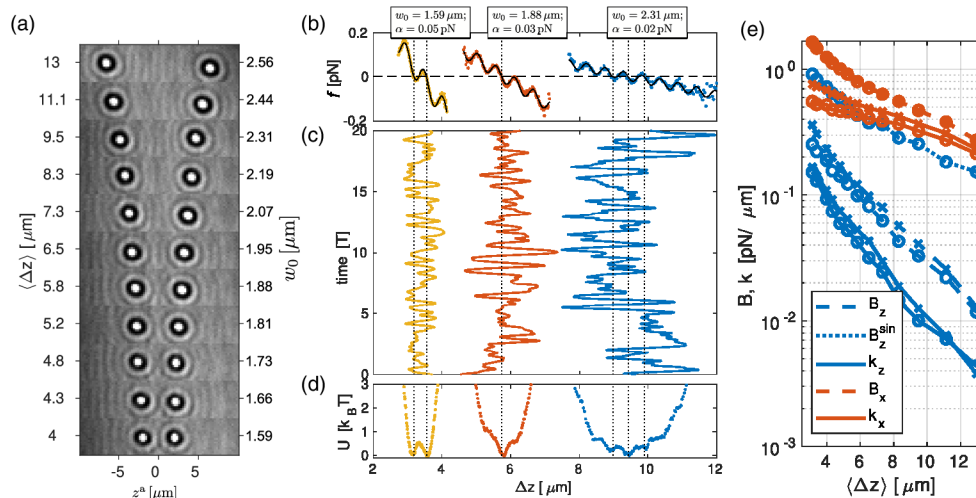


**Fig. 3.** Modification of optically bound structures by adjusting the width of the incident light beams. (a) Gradual expansion of an optically bound structure of two particles upon increasing the beam waist radius  $w_0$ . (b) Experimentally determined axial interparticle forces  $f_{z;21}$  (colored lines), together with the fits to Eq. (8) (black lines) for different values of  $\langle\Delta z\rangle$ . (c) Time evolution of breathing-mode trajectories along the  $z$  axis. The time is specified in the units of the breathing-mode oscillation period  $T$ . (d) Demonstration of anharmonicity of interparticle potential  $U_{z;21}$  caused by light interference. The potential profiles were determined by integration of the corresponding force profiles  $f_{z;21}$  shown in part (b). (e) Experimental dependence of the stiffness  $k_x, k_z$  of the external trapping potential, harmonic interparticle stiffness  $B_x, B_z$ , and modulated interparticle stiffness  $B_z^{\text{sin}}$  on the mean interparticle distance  $\langle\Delta z\rangle$ . The circles ( $\circ$ ) denote the stiffness values determined from the experimental force profiles reconstructed from the recorded particle trajectories, and the crosses ( $\times$ ) denote the stiffness values obtained from the corresponding resonant mode frequencies using Eqs. (6) and (7). All the data correspond to ambient pressure 6 millibar and laser power  $P = 37$  mW in both beams.

In the particular experiment illustrated in Fig. 3(a), the particle separation was varied between 4 and 13  $\mu\text{m}$  by increasing  $w_0$  from 1.6 to 2.6  $\mu\text{m}$ . The experimentally determined optical interparticle forces,  $f_{z;21}(\Delta z)$  (colored lines), together with the corresponding fits to Eq. (8) (black lines), are shown in Fig. 3(b) for three different values of  $w_0$ . The corresponding fitted values of

$\alpha$  significantly increase with reduced interparticle separation distance, indicating the increasing nonlinearity of the optical binding [42]. Larger modulation amplitudes  $\alpha$  then lead to the appearance of multiple stable particle configurations indicated by dotted vertical lines in Figs. 3(b)–3(d). Depending on the value of  $w_0$ , various anharmonic interparticle potentials,  $U_{z;21}(\Delta z)$ , were observed,

including double wells at small interparticle separations [see yellow line in Fig. 3(d)] and multistable potentials for larger separations [see blue line in Fig. 3(d)]. Due to weak barriers between the local minima in the potential landscape, the particles frequently jumped between multiple stable configurations, with a transition rate comparable to  $\omega_{\text{BR}}^z/2\pi = \sqrt{B/(4\pi^2 m)}$  [see Fig. 3(c)].

Figure 3(e) compares the stiffness  $k$  of the external trapping potential with the harmonic ( $B$ ) and sinusoidally modulated ( $B^{\text{sin}}$ ) interparticle stiffness for different mean particle separation distances,  $\langle \Delta z \rangle$ . Individual stiffness values were found using two independent procedures. In the first one, the stiffness was calculated from the spatial profiles of the interparticle force ( $B$ ,  $B^{\text{sin}}$ ) and external trapping force ( $k$ ) acting on the system of optically bound particles; these force profiles were determined from the analysis of experimental particle trajectories (see the discussion above and in the Methods section). Alternatively, the stiffness was estimated from the position of the characteristic spectral peaks in the PSDs of normal-mode coordinates and known particle mass (see Methods section). As illustrated in Fig. 3(e), the values of  $k$  and  $B$  obtained from the two procedures agree very well for both the  $x$  and  $z$  directions. Due to the small oscillation amplitude of particles confined in the secondary optical traps in multistable potentials and broadening of spectral peaks caused by anharmonicity of these potentials and relatively large viscous damping, we were not able to observe clear evidence of oscillatory peaks corresponding to  $\omega_{\text{BR}}^{z,\text{sin}} = \sqrt{B^{\text{sin}}/m}$  in the modal PSDs (see Supplement 1, Section 2, for details).

## D. Pressure Dependence and Collision of Particles

In the previous studies of the motion of individual optically levitated particles [8,9], it was observed the traps became unstable at pressures around 1 mbar, so an active feedback control scheme was required for trapping at such lower pressures. To study the dynamics of optically bound levitated particles under these ambient conditions, we gradually reduced the pressure from atmospheric level down to the critical value and continuously monitored the particles' response. In doing so, we took advantage of our position detection method based on an ultrafast CMOS camera, which gave us quantitative, properly calibrated information about the amplitude of particles' motion without any prior knowledge of the particles' properties [12].

In general, ambient pressure affects the profile of internal temperature within the levitated particles, which subsequently modifies their density and refractive index and influences the optical forces acting on the particles [49]. This effect was qualitatively studied using a theoretical model presented in Section 3 of the Supplement 1. However, by analysing particle trajectories recorded at different pressures, we found that the optical interparticle forces and potentials were almost independent of the pressure [see Figs. 4(a) and 4(b)]. Consequently, any changes in the optical properties of the particles were rather small. We conclude that the observed increase in the amplitude of particles' motion was primarily caused by increasing the kinetic energy of the ambient gas heated due to the absorption of the trapping laser light in the levitated particles [49–51].

Moreover, silica particles are porous and contain traces of condensed water, which, when heated, can evaporate, strongly affecting the particles' motion [52]. Using the width of the

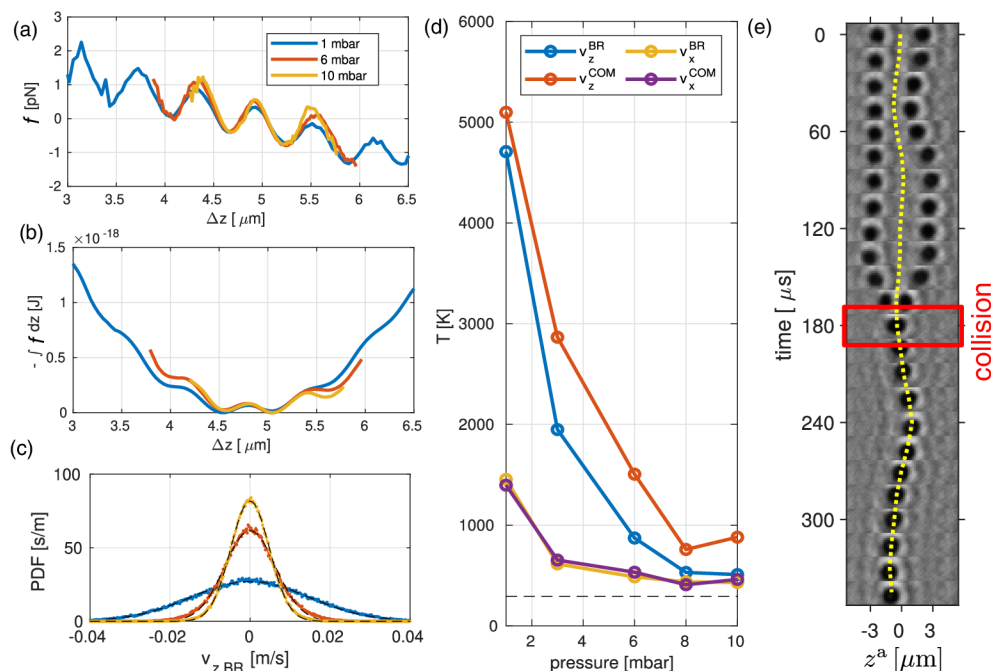


**Fig. 4.** Influence of ambient pressure on the dynamics of motion of optically bound particles. (a) Axial optical interparticle force  $f_{z,21}$  determined from particle experimental trajectories at different ambient pressures. (b) Axial optical interparticle potential  $U_{z,21}$  calculated by the integration of the corresponding force profiles shown in part (a). (c) Probability density functions PDF( $v$ ) for the velocity  $v_{z,\text{BR}}$  of the axial breathing mode determined from particle experimental trajectories at different ambient pressures. (d) Effective temperatures of the axial and transverse BR and COM normal modes calculated from the width of PDF( $v$ ) as a function of the ambient pressure. (e) Sequence of video frames showing a collision of two optically bound particles at the pressure of  $\sim 1$  mbar. Experimental parameters:  $w_0 = 2.8 \mu\text{m}$ , and  $P = 400$  mW in both beams.

probability density functions for velocity components  $v$ ,  $\text{PDF}(v) \propto \exp[-mv^2/(2k_B T)]$ , where  $m$  is the mass of the particle and  $k_B$  is the Boltzmann constant [see examples in Fig. 4(c)], we estimated the effective temperatures  $T$  of the axial and transverse BR and COM normal modes of optically bound particles [Fig. 4(d)]. We observed different effective temperatures for the particle motion along and perpendicular to the optical axis. We attribute this difference, at least in part, to anisotropic absorption of the incident laser light within the sphere volume [50]. While reducing the ambient pressure, the amplitudes of particle oscillations were observed to increase and, at a pressure around 1 mbar, the particles were observed to collide, as shown in Fig. 4(e).

To investigate the possible effects of nonconservative optical forces on the stability of optically levitated [53] and bound [25,35] structures, we carried out full 3D stochastic simulations of the system, using the multiple Mie scattering theory to correctly describe the optical forces acting on the system (see Section 4 of the Supplement 1). These simulations did not show any evidence of instability in the optically bound structures for pressures down to  $10^{-7}$  mbar and incident powers corresponding to the typical experimental values. Thus, nonconservative optical forces can be ruled out as the main source of the observed instability.

### E. Optically Bound Structures with More Than Two Particles

With a growing number of constituent particles, oscillatory dynamics of optically bound structures becomes significantly more intricate, containing contributions from multiple normal modes of increasing complexity. Figure 5 summarizes the analysis of motion of three identical optically bound particles. We calculated the pairwise optical interparticle forces from the time-averaged accelerations of the particles as  $f_{z,21}(\Delta z) = m(\ddot{z}_2^a - \ddot{z}_1^a)$  and  $f_{z,32}(\Delta z) = m(\ddot{z}_3^a - \ddot{z}_2^a)$ , where  $\Delta z = (z_2^a - z_1^a)$ ,  $\Delta z = (z_3^a - z_2^a)$  are the respective interparticle distances. According to the plots presented in Fig. 5(a), the profiles of  $f_{z,21}(\Delta z)$  and  $f_{z,32}(\Delta z)$  are almost identical, indicating a high degree of symmetry of the studied experimental configuration.

As predicted by the theoretical model of coupled, damped harmonic oscillators, which is developed and discussed in detail in Supplement 1 and summarized in the Methods section, the general motion of the particles along both axial  $z$  direction and transverse  $x$  direction can be decomposed into three normal modes. In particular, the particles display the COM mode, in which they all oscillate in phase with identical amplitudes and the frequency  $\omega_{\text{COM}} \approx \sqrt{k/m}$ , symmetric breathing (s-BR) mode, in which the middle particle remains stationary and the peripheral particles oscillate out of phase with identical amplitudes and the frequency  $\omega_{\text{s-BR}} \approx \sqrt{(k+b)/m}$ , and antisymmetric breathing (a-BR) mode, in which the peripheral particles oscillate in phase with identical amplitudes, while the middle particle oscillates out of phase with them with the frequency  $\omega_{\text{a-BR}} \approx \sqrt{(k+3b)/m}$ . After carrying out the coordinate transformations described in Supplement 1 and in the Methods section of this paper, the PSDs of the normal-mode coordinates can be calculated. Plots of these PSDs shown in Figs. 5(b) and 5(c) for the axial and transverse normal modes, respectively, clearly indicate distinct resonant frequencies for the three modes. The observed differences between the transverse and axial values of  $\omega_{\text{COM}}$ ,  $\omega_{\text{s-BR}}$ , and  $\omega_{\text{a-BR}}$  result from different values of the trapping and binding stiffness along the

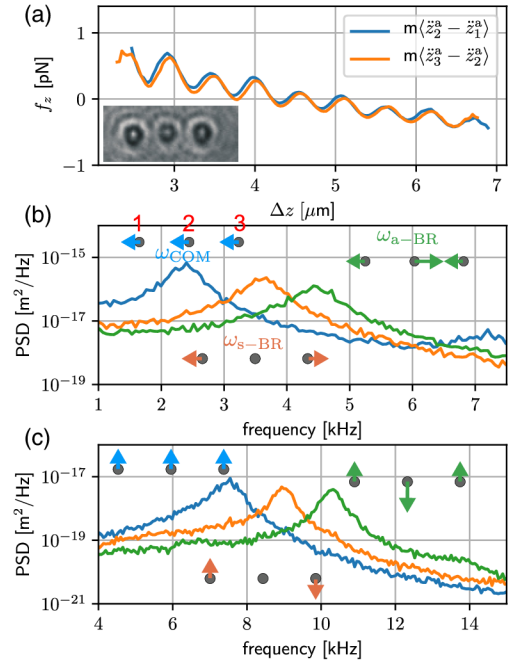


**Fig. 5.** Motional dynamics of three optically trapped and bound particles. (a) Pairwise optical interparticle forces  $f_{z,21}(\Delta z) = m(\ddot{z}_2^a - \ddot{z}_1^a)$  (blue line) and  $f_{z,32}(\Delta z) = m(\ddot{z}_3^a - \ddot{z}_2^a)$  (red line), acting between identical neighboring silica particles [1,2] and [2,3], respectively. Inset: Image of the trapped and bound particles with nominal diameters  $d = 600$  nm and refractive index  $n = 1.45$ . PSDs of the normal modes of oscillation of an optically bound structure of three particles (b) along the axial  $z$  direction, and (c) along the transverse  $x$  direction. Experimental parameters:  $w_0 = 1.95$   $\mu\text{m}$ , and  $P = 70$  mW in both beams.

two directions [22]. To compare the experimentally observed resonant frequencies with the model predictions, we determined the stiffness  $k$  of the external optical trapping potential and the binding stiffness  $b$  from  $\omega_{\text{COM}}$  and  $\omega_{\text{s-BR}}$  measured along both  $x$  and  $z$  directions, and, subsequently, used these values of  $k$  and  $b$  to calculate the expected  $\omega_{\text{a-BR}}$ . Comparison of thus calculated  $\omega_{\text{a-BR}}$  with the directly measured value obtained from the corresponding modal PSD revealed an acceptable 10% difference.

When working in overdamped conditions in aqueous environments, it is possible to experimentally study the dynamics of formation and motion of large assemblies of optically bound particles over extended periods of time [42]. On the other hand, at low ambient pressures associated with low viscous damping, we often observed collisions between individual trapped particles and irreversible formation of small particle clusters, which typically occurred during the particle loading process or during the evacuation of the sample chamber (see Supplement 1 for examples). Despite these experimental challenges, we were still able to form extended chains containing as many as 10 optically bound particles at atmospheric pressure. Usually, instabilities of the bound structures arose when the ambient pressure was reduced, resulting in the loss of the particles from the trap. However, we succeeded in resolving the normal modes of a chain of four optically bound particles confined at the pressure of 20 mbar (see Supplement 1, Section 5, for illustration).



## 4. CONCLUSION

In summary, we demonstrated stable optical binding of up to four microscopic silica particles confined in the underdamped regime, at pressures lower than 20 mbar, using cross-polarized counter-propagating Gaussian beams. We then presented a methodology that determines the parameters of such coupled oscillators—in particular, the trapping and binding stiffness—from the camera record of particles' trajectories. We were able to clearly resolve collective vibrational modes of optically bound structures characteristic of linearly coupled harmonic oscillators moving in the presence of weak viscous damping and hydrodynamic coupling. In addition, we observed and characterized sinusoidal modulations of the optical binding potentials describing a weak nonlinear inter-particle coupling, which is caused by interference of the incident and backscattered light [42] and results in multistability of such optically bound matter [48]. A similar type of externally controllable coupling nonlinearity could facilitate optically induced entanglement between the trapped mesoscopic particles [14,15], and is of significant interest for the systematic studies of energy redistribution between coupled nonlinear oscillators [17,18]. Currently, the lowest achievable gas pressure at which stable optically bound structures can be formed and maintained is limited to  $\sim 1$  mbar by heating effects, which substantially increase the center-of-mass motion of the particles, causing unwanted collisions and instabilities. However, by implementing a parametric feedback cooling scheme [8,9] or cavity-assisted cooling [7], both recently developed for individual optically levitated nanoparticles, it is feasible to selectively cool the collective vibrational modes of the structures, possibly all the way down to the quantum ground state. With efficient cooling protocols in place, the number of coupled degrees of freedom of the system could potentially be further expanded, which represents an important step toward the development of a mesoscopic experimental model of solid-state matter.

**Funding.** Grantová Agentura České Republiky (GA18-27546S); European Commission (CZ.1.05/2.1.00/01.0017); Akademie Věd České Republiky (RVO:68081731); Ministerstvo Školství, Mládeže a Tělovýchovy (LO1212); European Regional Development Fund (CZ.02.1.01/0.0/0.0/16\_026/0008460).

**Disclosures.** The authors declare no conflicts of interest.

**Supplemental document.** See Supplement 1 for supporting content.

## REFERENCES

1. A. Ashkin and J. Dziedzic, "Optical levitation in high vacuum," *Appl. Phys. Lett.* **28**, 333–335 (1976).
2. Z.-Q. Yin, A. A. Geraci, and T. Li, "Optomechanics of levitated dielectric particles," *Int. J. Mod. Phys. B* **27**, 1330018 (2013).
3. J. Gieseler and J. Millen, "Levitated nanoparticles for microscopic thermodynamics—a review," *Entropy* **20**, 326 (2018).
4. D. Chang, C. Regal, S. Papp, D. Wilson, J. Ye, O. Painter, H. Kimble, and P. Zoller, "Cavity opto-mechanics using an optically levitated nanosphere," *Proc. Natl. Acad. Sci. USA* **107**, 1005–1010 (2010).
5. P. F. Barker and M. N. Shneider, "Cavity cooling of an optically trapped nanoparticle," *Phys. Rev. A* **81**, 023826 (2010).
6. O. Romero-Isart, M. Juan, R. Quidant, and J. I. Cirac, "Toward quantum superposition of living organisms," *New J. Phys.* **12**, 033015 (2010).
7. U. Delić, M. Reisenbauer, K. Dare, D. Grass, V. Vuletić, N. Kiesel, and M. Aspelmeyer, "Cooling of a levitated nanoparticle to the motional quantum ground state," *Science* **367**, 892–895 (2020).
8. T. Li, S. Kheifets, and M. G. Raizen, "Millikelvin cooling of an optically trapped microsphere in vacuum," *Nat. Phys.* **7**, 527–530 (2011).
9. J. Gieseler, B. Deutsch, R. Quidant, and L. Novotny, "Subkelvin parametric feedback cooling of a laser-trapped nanoparticle," *Phys. Rev. Lett.* **109**, 103603 (2012).
10. F. Tebbenjohanns, M. Frimmer, V. Jain, D. Windey, and L. Novotny, "Motional sideband asymmetry of a nanoparticle optically levitated in free space," *Phys. Rev. Lett.* **124**, 013603 (2020).
11. L. Rondin, J. Gieseler, F. Ricci, R. Quidant, C. Dellago, and L. Novotny, "Direct measurement of Kramers turnover with a levitated nanoparticle," *Nat. Nanotechnol.* **12**, 1130–1133 (2017).
12. V. Svak, O. Brzobohatý, M. Šiler, P. Ják, J. Kaňka, P. Zemánek, and S. H. Simpson, "Transverse spin forces and non-equilibrium particle dynamics in a circularly polarized vacuum optical trap," *Nat. Commun.* **9**, 5453 (2018).
13. M. Arndt and K. Hornberger, "Testing the limits of quantum mechanical superpositions," *Nat. Phys.* **10**, 271–277 (2014).
14. H. Nguyen and F. Bernards, "Entanglement dynamics of two mesoscopic objects with gravitational interaction," *Eur. Phys. J. D* **74**, 69 (2020).
15. S. Qvarfort, S. Bose, and A. Serafini, "Mesoscopic entanglement through central-potential interactions," *J. Phys. B* **53**, 235501 (2020).
16. E. Fermi, P. Pasta, S. Ulam, and M. Tsingou, "Studies of the nonlinear problems," Technical Report LA-1940 (Los Alamos Scientific Lab, 1955).
17. J. Ford, "The Fermi-Pasta-Ulam problem: paradox turns discovery," *Phys. Rep.* **213**, 271–310 (1992).
18. R. Livi, M. Pettini, S. Ruffo, M. Sparpaglione, and A. Vulpiani, "Equipartition threshold in nonlinear large Hamiltonian systems: the Fermi-Pasta-Ulam model," *Phys. Rev. A* **31**, 1039–1045 (1985).
19. M. M. Burns, J.-M. Fournier, and J. A. Golovchenko, "Optical matter: crystallization and binding in intense optical fields," *Science* **249**, 749–754 (1990).
20. S. A. Tatarikova, A. E. Carruthers, and K. Dholakia, "One-dimensional optically bound arrays of microscopic particles," *Phys. Rev. Lett.* **89**, 283901 (2002).
21. W. Singer, M. Frick, S. Bernet, and M. Ritsch-Marte, "Self-organized array of regularly spaced microbeads in a fiber-optical trap," *J. Opt. Soc. Am. B* **20**, 1568–1574 (2003).
22. K. Dholakia and P. Zemánek, "Gripped by light: optical binding," *Rev. Mod. Phys.* **82**, 1767–1791 (2010).
23. T. Čížmár, L. C. D. Romero, K. Dholakia, and D. L. Andrews, "Multiple optical trapping and binding: new routes to self-assembly," *J. Phys. B* **43**, 102001 (2010).
24. O. Brzobohatý, A. V. Arzola, M. Šiler, L. Chvátal, P. Ják, S. Simpson, and P. Zemánek, "Complex rotational dynamics of multiple spheroidal particles in a circularly polarized, dual beam trap," *Opt. Express* **23**, 7273–7287 (2015).
25. S. H. Simpson, P. Zemánek, O. M. Maragò, P. H. Jones, and S. Hanna, "Optical binding of nanowires," *Nano Lett.* **17**, 3485–3492 (2017).
26. M. G. Donato, O. Brzobohatý, S. H. Simpson, A. Irrera, A. A. Leonardi, M. J. Lo Faro, V. Svak, O. M. Maragò, and P. Zemánek, "Optical trapping, optical binding, and rotational dynamics of silicon nanowires in counter-propagating beams," *Nano Lett.* **19**, 342–352 (2019).
27. V. Demergis and E.-L. Florin, "Ultrastrong optical binding of metallic nanoparticles," *Nano Lett.* **12**, 5756–5760 (2012).
28. Z. Yan, S. K. Gray, and N. F. Scherer, "Potential energy surfaces and reaction pathways for light-mediated self-organization of metal nanoparticle clusters," *Nat. Commun.* **5**, 3751 (2014).
29. Y. Li, H. Xin, Y. Zhang, H. Lei, T. Zhang, H. Ye, J. J. Saenz, C.-W. Qiu, and B. Li, "Living nanospear for near-field optical probing," *ACS Nano* **12**, 10703–10711 (2018).
30. O. Brzobohatý, R. J. Hernández, S. Simpson, A. Mazzulla, G. Cipparrone, and P. Zemánek, "Chiral particles in the dual-beam optical trap," *Opt. Express* **24**, 26382–26391 (2016).
31. C. D. Mellor, T. A. Fennerty, and C. D. Bain, "Polarization effects in optically bound particle arrays," *Opt. Express* **14**, 10079–10088 (2006).
32. F. Nan and Z. Yan, "Probing spatiotemporal stability of optical matter by polarization modulation," *Nano Lett.* **18**, 1396–1401 (2018).
33. T. Čížmár, O. Brzobohatý, K. Dholakia, and P. Zemánek, "The holographic optical micro-manipulation system based on counter-propagating beams," *Laser Phys. Lett.* **8**, 50–56 (2011).
34. O. Brzobohatý, V. Karásek, T. Čížmár, and P. Zemánek, "Dynamic size tuning of multidimensional optically bound matter," *Appl. Phys. Lett.* **99**, 101105 (2011).
35. S. Sukhov, A. Shalin, D. Haefner, and A. Dogariu, "Actio et reactio in optical binding," *Opt. Express* **23**, 247–252 (2015).
36. S. Sukhov and A. Dogariu, "Non-conservative optical forces," *Rep. Prog. Phys.* **80**, 112001 (2017).

37. V. Karásek, M. Šiler, O. Brzobohatý, and P. Zemánek, "Dynamics of an optically bound structure made of particles of unequal sizes," *Opt. Lett.* **42**, 1436–1439 (2017).
38. L. Chvátal, O. Brzobohatý, and P. Zemánek, "Binding of a pair of Au nanoparticles in a wide Gaussian standing wave," *Opt. Rev.* **22**, 157–161 (2015).
39. D. S. Bykov, S. Xie, R. Zeltner, A. Machnev, G. K. L. Wong, T. G. Euser, and P. St.J. Russell, "Long-range optical trapping and binding of microparticles in hollow-core photonic crystal fibre," *Light Sci. Appl.* **7**, 22 (2018).
40. Y. Arita, E. M. Wright, and K. Dholakia, "Optical binding of two cooled micro-gyroscopes levitated in vacuum," *Optica* **5**, 910–917 (2018).
41. S. Divitt, L. Rondin, and L. Novotny, "Cancellation of non-conservative scattering forces in optical traps by counter-propagating beams," *Opt. Lett.* **40**, 1900–1903 (2015).
42. O. Brzobohatý, L. Chvátal, and P. Zemánek, "Optomechanical properties of optically self-arranged colloidal waveguides," *Opt. Lett.* **44**, 707–710 (2019).
43. O. Brzobohatý, L. Chvátal, A. Jonáš, M. Šiler, J. Kaňka, J. Ježek, and P. Zemánek, "Tunable soft-matter optofluidic waveguides assembled by light," *ACS Photon.* **6**, 403–410 (2019).
44. I. T. Leite, S. Turtaev, X. Jiang, M. Šiler, A. Cuschieri, P. St.J. Russell, and T. Čižmár, "Three-dimensional holographic optical manipulation through a high-numerical-aperture soft-glass multimode fibre," *Nat. Photonics* **12**, 33–39 (2018).
45. B. R. Slezak and B. D'Urso, "A microsphere molecule: the interaction of two charged microspheres in a magneto-gravitational trap," *Appl. Phys. Lett.* **114**, 244102 (2019).
46. R. Diehl, E. Hebestreit, R. Reimann, F. Tebbenjohanns, M. Frimmer, and L. Novotny, "Optical levitation and feedback cooling of a nanoparticle at subwavelength distances from a membrane," *Phys. Rev. A* **98**, 013851 (2018).
47. D. Mackowski, *The Extension of Mie Theory to Multiple Spheres* (Springer, 2012), pp. 223–256.
48. V. Karásek, T. Čižmár, O. Brzobohatý, P. Zemánek, V. Garcés-Chávez, and K. Dholakia, "Long-range one-dimensional longitudinal optical binding," *Phys. Rev. Lett.* **101**, 143601 (2008).
49. E. Hebestreit, R. Reimann, M. Frimmer, and L. Novotny, "Measuring the internal temperature of a levitated nanoparticle in high vacuum," *Phys. Rev. A* **97**, 043803 (2018).
50. J. Millen, T. Deesuwan, P. Barker, and J. Anders, "Nanoscale temperature measurements using non-equilibrium Brownian dynamics of a levitated nanosphere," *Nat. Nanotechnol.* **9**, 425–429 (2014).
51. J. Millen, T. S. Monteiro, R. Pettit, and A. N. Vamivakas, "Optomechanics with levitated particles," *Rep. Prog. Phys.* **83**, 026401 (2020).
52. F. Ricci, "Levitodynamics toward force nano-sensors in vacuum," Ph.D. thesis (Institut de Ciències Fotòniques, 2019).
53. Y. Roichman, B. Sun, A. Stolarski, and D. G. Grier, "Influence of nonconservative optical forces on the dynamics of optically trapped colloidal spheres: the fountain of probability," *Phys. Rev. Lett.* **101**, 128301 (2008).

## 4.2 Experimental observation of vacuum optical binding of multiple particles

In principle, the trapping geometry with two counter-propagating beams is capable of confining long particle chains containing tens of particles; this was demonstrated in experiments carried out in aqueous environment [98]. Under atmospheric pressure conditions, we observed stable trapping of chains consisting of up to ten particles (see Fig. 4.1a). Since the standard deviation of the particle size distribution is quite wide (12% of the particle diameter), it was very rare to trap more particles of equal diameter. The size difference could be substantial, as illustrated in Fig. 4.1b. Both the long chains and the chains of particles with large size differences proved to be very unstable; they always escaped from the trap when the ambient pressure was lowered due to reduced viscous damping. Fig. S4.1c shows the gradual collapse of an optically bound structure formed by four particles of different sizes. Note that the particles did not leave the trap one by one; instead, they crashed into each other and the resulting cluster then left the trap.

We were able to reach the pressure of  $\sim 20$  mbar with a chain of four particles of similar sizes. The PSDs of the motion of individual particles in such a chain are depicted in Fig. 4.1d. In this particular case, the PSDs along the  $z$  direction (Fig. 4.1d left) were virtually single-peaked and the motion of individual particles seemed to be mutually independent. Upon transformation to the normal-mode coordinates, (using for example the eigenvectors given in Table S3 in supplementary information of [99]), the spectral peaks become mixed (Fig. 4.1e left). Regarding the  $x$  direction, the PSDs of the direct particle coordinates show that the particles were coupled, although rather loosely (Fig. 4.1d right). Upon transformation to the normal-mode coordinates, the spectral peaks separate (Fig. 4.1e right). These complex trends in the particle dynamics arise from the differences in the particle size; thus, they cannot be directly predicted using the theory developed also in Supplement of the presented paper [99], Sections D and E of, and which assumed interactions between particles of identical sizes.

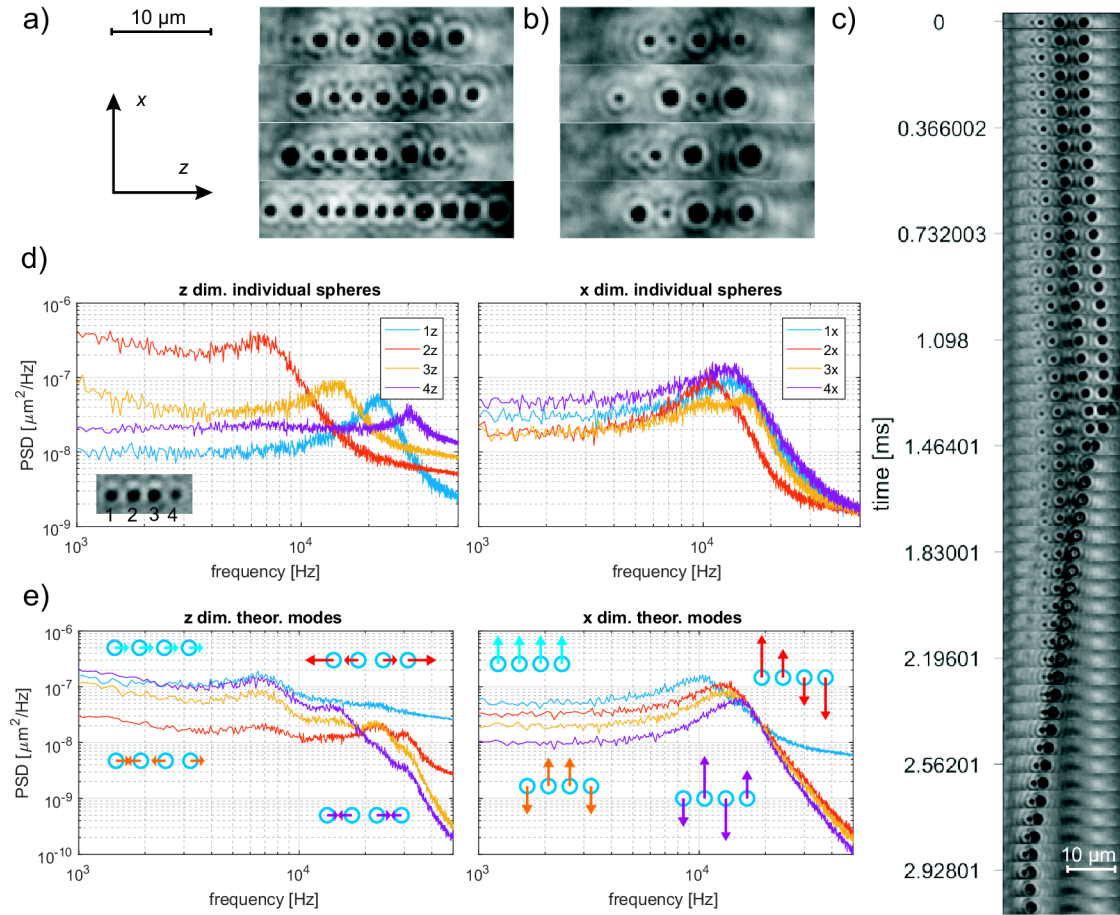


Fig. 4.1: Experimental observation of optical binding of multiple particles in low-viscosity environment. a) Examples of various long chains of particles stably trapped at atmospheric pressure. b) Chains of particles of different sizes confined at atmospheric pressure. c) Sequence of time-lapse images depicting collision of four particles followed by their clustering. d) Position PSDs of individual particles in an optically bound chain of four particles: left -  $z$  direction, right -  $x$  direction. e) Position PSDs of normal modes of the same four-particle chain as in part d): left -  $z$  direction, right -  $x$  direction.

## 5 Force estimation from stochastic trajectory

The optical forces acting on a probe particles are utilized in broad range of experimental techniques used in soft and active matter, biophotonics or optomechanics. Often, the precise knowledge of the force field felt by the particle is essential. In this chapter I focus on an unresolved method how to extract an acting force from a measured particles stochastic trajectory.

None of the current methods is capable of mapping complex non-conservative force fields using the under-damped stochastic motion of the trapped bead. The calibration techniques used today are either suitable only for certain field geometry or they are limited to the over-damped regime. The methods as potential analysis (PA), equipartition method, mean squared displacement analysis, autocorrelation function analysis (all described in Ref. [88]) or Bayesian inference methods [100, 101, 102, 103] assume harmonic oscillator as the model system. The Bayesian methods as well as maximum likelihood method FORMA [104] or the mean drift method [105, 106, 107] are applicable only on over-damped bead dynamics. Some methods can be used for inference of more complex conservative fields (FORMA or potential analysis [88]). It was even shown that FORMA, ACF or Bayesian inference can be adapted for non-conservative force field measurement [108], but still only for over-damped dynamics. Here we present a powerful algorithm for local force estimation based on calculation of local average velocity and acceleration of Brownian trajectories in under-damped regime. The presented approach estimates correctly both the conservative and the non-conservative fields. The performance of the algorithm is shown using both stochastically simulated and experimentally measured trajectories.

I worked out the original idea proposed by my colleague L. Chvátal to the form presented below. I developed the Matlab scripts processing input data, designed the simulations, carried out the experiments and evaluated the performance of the proposed method. I also addressed the influence of additive noise in position detection chain on the estimated force values, came up with the presented correction procedure and implemented it in the Matlab scripts. L. Chvátal helped me with derivation of the joint distribution of noise and the second derivative of noise expressed in equation (5.28). The simulation software used for 1D simulations was developed by M. Šiler, the simulations of stochastic motion in 2D non-conservative force fields were provided by Stephen Simpson.

## 5.1 Estimation procedure

In general, the motion of optically trapped spherical bead is given by a Langevine equation,

$$\mathbf{F}(\mathbf{r}) - \gamma\dot{\mathbf{r}} + \mathbf{F}^L(t) = m\ddot{\mathbf{r}}. \quad (5.1)$$

Here,  $\mathbf{F}$  would typically be the optical force as a function of position,  $\mathbf{r} = (x, y, z)$ . But in general,  $\mathbf{F}$  could be any kind of force, which depends only on position. For example, electrostatic force on electrically charged particle or combination of optical and electrostatic force. In any case, the first term in equation (5.1), the force  $\mathbf{F}(\mathbf{r})$ , is the force we estimate and refer to in this chapter.  $\mathbf{F}^L(t)$  is the Brownian stochastic force caused by air molecules randomly impinging on the bead.  $\mathbf{F}^L(t)$  is a white-noise process fulfilling:

$$\langle \mathbf{F}^L(t) \rangle = 0 \quad (5.2a)$$

$$\langle \mathbf{F}^L(t) \otimes \mathbf{F}^L(t') \rangle = 2k_B T \gamma \mathbf{I} \delta(t - t'), \quad (5.2b)$$

with  $\mathbf{I}$  being the unit matrix. Here we consider only time independent optical forces,  $\mathbf{F} \neq \mathbf{F}(t)$ . Lets assume a bead is moving along a certain stochastic trajectory  $\mathbf{r}(t)$  fulfilling equation (5.1) and we are interested in finding the value of force  $\mathbf{F}(\mathbf{r}_0)$  in particular position  $\mathbf{r}_0$ . During its motion, the bead visits  $\mathbf{r}_0$  many times. Every time the beads position is  $\mathbf{r} = \mathbf{r}_0$ , it feels the same force  $\mathbf{F}(\mathbf{r}_0)$ , but the viscous drag  $\gamma\dot{\mathbf{r}}$  and inertia  $m\ddot{\mathbf{r}}$  differ from time to time, since the trajectory is stochastic. Now we average the equation of motion (5.1) only across the time instants, when the beads position is  $\mathbf{r}_0$ , formally writing

$$\langle \mathbf{F}(\mathbf{r}) \rangle_{\mathbf{r}=\mathbf{r}_0} - \gamma \langle \dot{\mathbf{r}} \rangle_{\mathbf{r}=\mathbf{r}_0} + \langle \mathbf{F}^L \rangle_{\mathbf{r}=\mathbf{r}_0} = m \langle \ddot{\mathbf{r}} \rangle_{\mathbf{r}=\mathbf{r}_0}. \quad (5.3)$$

The proposed method assumes, that the Brownian force averages out,  $\langle \mathbf{F}^L \rangle_{\mathbf{r}=\mathbf{r}_0} = 0$ , for all  $\mathbf{r}_0$  and the force is then given by the average velocity and the average acceleration in  $\mathbf{r}_0$ :

$$\mathbf{F}(\mathbf{r}_0) = \gamma \langle \dot{\mathbf{r}} \rangle_{\mathbf{r}=\mathbf{r}_0} + m \langle \ddot{\mathbf{r}} \rangle_{\mathbf{r}=\mathbf{r}_0}. \quad (5.4)$$

Although a rigorous mathematical proof of this assumption is lacking, in the following text we show that it is reasonable and we rightly estimate the force using equation (5.4).

A typical measured trajectory  $\mathbf{r}_n = (x_n, y_n, z_n) = \mathbf{r}(t_n)$  is a series of  $\mathcal{N}$  positions in discrete time instants  $t_n$  separated by  $\Delta t$ . The velocity  $\mathbf{v}_n = \mathbf{v}(t_n)$  and acceleration  $\mathbf{a}_n = \mathbf{a}(t_n)$  waveforms are calculated from the measured trajectory  $\mathbf{r}_n$  by numerical differentiation using central formulas, two-point formula for velocity and

three-point formula for acceleration.

$$\begin{aligned}\mathbf{v}_n &= \frac{\mathbf{r}_{n+1} - \mathbf{r}_{n-1}}{2\Delta t} \\ \mathbf{a}_n &= \frac{\mathbf{r}_{n+1} - 2\mathbf{r}_n + \mathbf{r}_{n-1}}{\Delta t^2}.\end{aligned}\tag{5.5}$$

The proposed method uses the measured trajectory and calculated velocity and acceleration to estimate the force field not as a continuous function of position  $\mathbf{r}$ , but in discrete positions using a spatial binning process. The optical trap volume is divided into rectangular spatial boxes of dimensions  $\Delta x, \Delta y, \Delta z$  centered around position  $\mathbf{b}_i = (b_{x,i}, b_{y,i}, b_{z,i})$ . For each box, one value of force  $\langle \mathbf{F} \rangle_i$  is calculated by taking the mean value of acceleration and velocity, but the mean value is taken only across the time instants when the bead is positioned inside the particular bin  $\mathbf{b}_i$  - this is the averaging operation we indicate by  $\langle \cdot \rangle_i$  and defined by equations (5.6) and (5.7). This is illustrated in Fig. 5.1a where a little section of a stochastic trajectory is plotted. The red dashed lines show the edges of bin  $b_{13}$ , the samples that are taken into the mean values calculated for  $b_{13}$  are plotted in red. From now on, the subscript  $n$  refers to a particular time instants (or samples) in time ( $t_n$ ), whereas the subscript  $i$  refers to particular spatial bin.

The mean velocity and acceleration in a bin  $\mathbf{b}_i$  is calculated as follows:

$$\langle \mathbf{a} \rangle_i = \frac{1}{\mathcal{N}_i} \sum_{n=1}^{\mathcal{N}} \mathbf{a}_n I(\mathbf{b}_i, \mathbf{r}_n)\tag{5.6a}$$

$$\langle \mathbf{v} \rangle_i = \frac{1}{\mathcal{N}_i} \sum_{n=1}^{\mathcal{N}} \mathbf{v}_n I(\mathbf{b}_i, \mathbf{r}_n)\tag{5.6b}$$

$$\langle \mathbf{r} \rangle_i = \frac{1}{\mathcal{N}_i} \sum_{n=1}^{\mathcal{N}} \mathbf{r}_n I(\mathbf{b}_i, \mathbf{r}_n),\tag{5.6c}$$

where  $I(\mathbf{b}_i, \mathbf{r}_n) = 1$ , if the beads position  $\mathbf{r}_n$  in time  $t_n$  is within the spatial bin  $\mathbf{b}_i$  (red samples for  $b_{13}$  in Fig. 5.1a), otherwise  $I(\mathbf{b}_i, \mathbf{r}_n) = 0$ .  $\mathcal{N}_i = \sum_{n=1}^{\mathcal{N}} I(\mathbf{b}_i, \mathbf{r}_n)$  is the total number of points in the bin  $\mathbf{b}_i$ . The optical force profile is then estimated in discrete positions

$$\langle \mathbf{F} \rangle_i = m \langle \mathbf{a} \rangle_i + \gamma \langle \mathbf{v} \rangle_i.\tag{5.7}$$

The spatial dimensions of position bins are chosen with respect to the force spatial changes. A suitable choice is such that the force change across a bin can be well approximated by linear function. If the force is not constant across a bin, the equations (5.3) and (5.6) do not provide a force estimate centered in  $\mathbf{b}_i$ . In the following section we show for 1D case that force value found by averaging,  $\langle \mathbf{F} \rangle_i$ , corresponds to the force value in the mean position  $\langle \mathbf{r} \rangle_i$ ,  $\mathbf{F}(\langle \mathbf{r} \rangle_i)$ , rather than to the force value in the center of the bin  $\mathbf{F}(\mathbf{b}_i)$  due to the irregular position probability

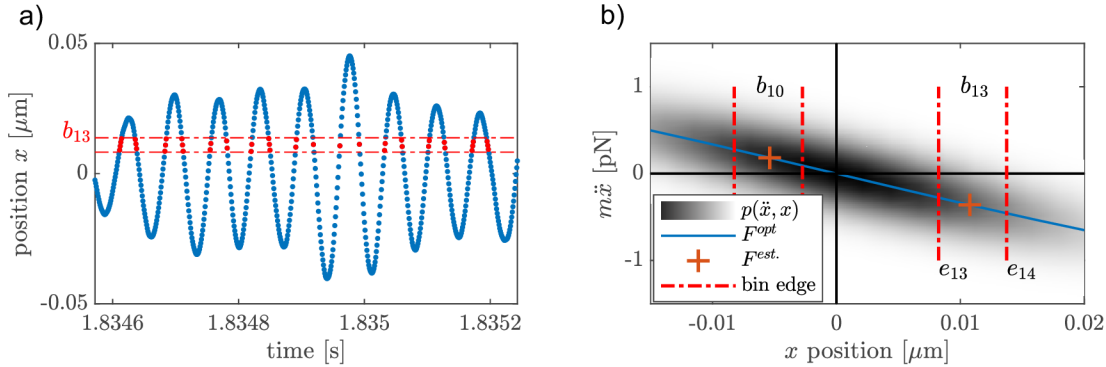


Fig. 5.1: Illustration of the binning principle, where  $\mathbf{r} = (x_n)$  and  $\mathbf{b}_i = (b_{x,i})$ . (a) While calculating the mean values for bin  $b_{13}$  only the time instants when the position is inside the bin (red samples) are taken into account. (b) The grayscale map is the 2D histogram of the bead having the position  $x$  and acceleration  $\ddot{x}$  (multiplied by mass  $m$ ). When estimating the mean force  $\langle F \rangle_i$  (orange cross), the acceleration is averaged across the area between the respective bin edges. The blue curve is the original force profile  $F(x)$  which is searched for. In 1D case the mean velocity is zero and does not contribute to the mean force as discussed later.

density function within the bin. This means, that the method does not provide estimates of force value in regularly spaced positions  $\mathbf{b}_i$ , but in irregularly spaced mean positions in bins,  $\langle \mathbf{r} \rangle_i$ , defined by eq. (5.6c).

It is worth examining the special case of conservative force field  $\mathbf{F}(\mathbf{r})$ . If a particle of mass  $m$  is subjected to a conservative force field  $\mathbf{F}(\mathbf{r})$ , it reaches a thermal equilibrium with the surrounding gas of temperature  $T$  and its state is described by the Gibbs-Boltzmann distribution

$$p_{GB}(\mathbf{r}, \mathbf{v}) \propto \exp\left(-\frac{\frac{1}{2}m\mathbf{v}^2 + U(\mathbf{r})}{k_B T}\right) \quad (5.8a)$$

$$\propto \exp\left(-\frac{\frac{1}{2}m\mathbf{v}^2}{k_B T}\right) \exp\left(-\frac{U(\mathbf{r})}{k_B T}\right) = p(\mathbf{v})p(\mathbf{r}). \quad (5.8b)$$

with  $k_B$  the Boltzmann constant,  $U(\mathbf{r})$  being the potential energy and  $\frac{1}{2}m\mathbf{v}^2$  the kinetic energy of the particle. The average velocity calculated across certain position bin  $\mathbf{b}_i$  is given as  $\langle \mathbf{v} \rangle_i = \int_{-\infty}^{\infty} \mathbf{v} p(\mathbf{v}|\mathbf{b}_i) d\mathbf{v}$  where  $p(\mathbf{v}|\mathbf{b}_i)$  is the conditional probability density function of the instantaneous velocity of the bead being  $\mathbf{v}$  provided the instantaneous position is inside the bin  $\mathbf{b}_i$ . Since the position  $\mathbf{r}$  and the velocity  $\mathbf{v}$  are independent random variables, as shown by equation (5.8a), the conditional probability is given only by the marginal probability density function of velocity,  $p(\mathbf{v}|\mathbf{b}_i) \propto p(\mathbf{v})$ , which is a Gaussian function with zero mean. So the mean velocity



is zero for all bins and it does not contribute to the estimated force value. The mean velocities obtained by binning in 1D simulated trajectories correspond to this observation as shown in figure 5.2a). Here  $\langle \mathbf{v} \rangle_i = 0$  within the errorbar for all position bins.

We would like to stress several aspects of the binning method:

- we estimate the uncertainty  $u(\langle Q \rangle_i)$  of mean values of quantity  $Q$  (force, velocity, acceleration) as the standard deviation of the mean:

$$u(\langle Q \rangle_i) = \sqrt{\frac{1}{\mathcal{N}_i(\mathcal{N}_i - 1)} \sum_{n=1}^{\mathcal{N}_i} (Q_n - \langle Q \rangle_i)^2}. \quad (5.9)$$

This uncertainty decreases as  $1/\sqrt{\mathcal{N}_i}$  so the precision of estimation grows with number of samples in each bin. The estimated force value in bins which are visited very rarely can be quite high (see. Fig. 5.2).

- the method provides reasonable estimation for position dependent forces only. We suspect our method would fail in case the force is also dependent on time or orientation of the trapped bead, although we have not investigated these cases properly. For example, in the case of spherically non-symmetrical beads, like discs or nano-wires, where  $\mathbf{F}(\mathbf{r})$  is also a function of orientation, this formula would give rather random number. The same would hold for force fields generated by laser beams with unstable, fluctuating optical power or if oscillating external electric force is used for driving the motion of electrically charged bead.
- the bead mass  $m$  and drag coefficient  $\gamma$  must be known for precise estimation. Both these parameters can be calculated theoretically from bead size and density stated by the manufacturer. But the uncertainty of the size stated can be as high as 12% which causes uncertainty about 36% for  $m$  and 23% for  $\gamma$  for our typical conditions. The beads parameters can be more precisely measured experimentally. The damping coefficient  $\gamma$  can be estimated with uncertainty easily below 0.1% by fitting the power spectral density function (PSD) of position or the position auto-correlation function of motion in the parabolic potential. The beads mass  $m$  can be measured by fitting the beads relaxation to equilibrium position after it was displaced from it by DC electric field [109]. Another method of measuring  $m$  is to fit the PSD of motion of electrically charged bead driven by electric field on a single harmonic frequency [110].
- the validity of equation (5.3) requires the mechanical system to be in a steady state so that the mean values do not change in time. It does not require the system to meet additional conditions like conservativeness of the force field, ther-

mal equilibrium or at least a state close to thermal equilibrium, so a method of force estimation based on this equation is very universal and reliable, even if the motional state is not precisely known.

## 5.2 Conservative force field - 1D case

Here we focus on the one-dimensional geometry. Our goal is to estimate the force  $\mathbf{F}(\mathbf{r})$  as stated in equation (5.1). For 1D case we use the notation  $\mathbf{r} \rightarrow x$  and  $\mathbf{F}(\mathbf{r}) \rightarrow F(x)$ . First we show, that the mean force  $\langle F \rangle_i$  calculated across a bin  $b_i$  corresponds to the original force in position  $\langle x \rangle_i$  rather than in position of the bin center. This effect is apparently caused by the fact, that the force  $F(x)$  is not constant on the interval  $\Delta x$  spanned by a certain bin, which leads to nonuniform potential  $U(x)$  and nonuniform position probability density function  $p(x)$ . In another words, if the probability density function  $p(x)$  is not constant across one bin, the bead is more likely to be located near the bin edge, where  $p(x)$  is higher, and the force value from this area contributes with bigger weight to the average,  $\langle F \rangle_i$ , than the force value from the opposite side of the bin. So the value  $\langle F \rangle_i$  should not be put to the center of the bin, but it should be shifted towards the edge, where  $p(x)$  is higher.

If the force does not change much across a bin, it can be expressed using the Taylor expansion in a certain point  $x_i$

$$F(x) = F(x_i) + F'(x_i)(x - x_i) + \frac{1}{2}F''(x_i)(x - x_i)^2 + \dots \quad (5.10)$$

For a bin  $b_i$  there is a set  $X_i$  of  $\mathcal{N}_i$  positions from the measured trajectory  $x_n$ , which fall to the bin,  $X_i = \{x_n | x_n \in b_i\}$ . Since the force  $F(x)$  is a function of  $x$ , there is also a set of force values corresponding to  $X_i$  and we can calculate average across this set in the same way as in (5.6),  $\langle F(x) \rangle_i = \frac{1}{\mathcal{N}_i} \sum_{n=1}^{\mathcal{N}_i} I(b_i, x_n)$ . Performing this averaging across one bin on equation (5.10) gives:

$$\begin{aligned} \langle F \rangle_i \approx & F(x_i) \frac{1}{\mathcal{N}_i} \sum_{n=1}^{\mathcal{N}_i} I(b_i, x_n) + F'(x_i) \frac{1}{\mathcal{N}_i} \sum_{n=1}^{\mathcal{N}_i} x_n I(b_i, x_n) \\ & - F'(x_i) x_i \frac{1}{\mathcal{N}_i} \sum_{n=1}^{\mathcal{N}_i} I(b_i, x_n) + \frac{1}{2} F''(x_i) \frac{1}{\mathcal{N}_i} \sum_{n=1}^{\mathcal{N}_i} (x_n - x_i)^2 I(b_i, x_n) \end{aligned} \quad (5.11)$$

If the force is Taylor expanded around the mean sample position  $\langle x \rangle_i = \frac{1}{\mathcal{N}_i} \sum_{n=1}^{\mathcal{N}_i} x_n I(b_i, x_n)$  (as defined in equation (5.6)), the average force can be expressed as

$$\langle F \rangle_i \approx F(\langle x \rangle_i) + \frac{1}{2} F''(\langle x \rangle_i) \sigma_i^2(x), \quad (5.12)$$

where  $\sigma_i^2(x)$  is the variance of position coordinate of samples falling to bin  $b_i$ .

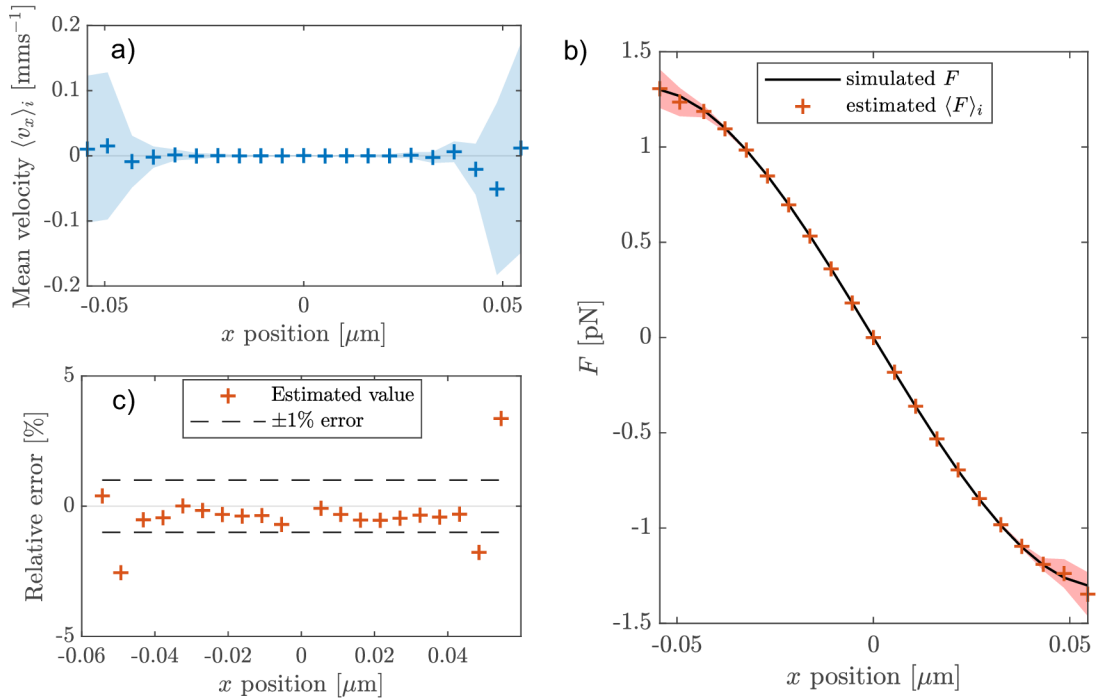


Fig. 5.2: Force estimation in 1D conservative force of the Duffing form from simulated stochastic trajectory. The trajectory was simulated with time increment  $\Delta t = 1 \mu$  s for silica particle of diameter  $1.54 \mu\text{m}$  with  $m = 3.83 \cdot 10^{-15}$  kg,  $\gamma = 4.63 \cdot 10^3 \frac{\text{kg}}{\text{s}}$  and the parameters of force  $\frac{\Omega_0}{2\pi} = 15$  kHz,  $\xi = 100 \mu\text{m}^{-1}$ . Only one trajectory is used - 5s long,  $\mathcal{N} = 5 \cdot 10^6$  samples. The force was estimated in 21 spatial bins with bin size  $\Delta x = 5.5$  nm. (a) Mean velocities in position bins (blue crosses). The light blue area represents the estimation uncertainty (defined in eq. (5.9)). (b) Comparison of numerical simulation input force field (solid black line) and estimated force field (crosses). The light red area represents the estimation uncertainty. (c) Relative error of estimation  $\rho_{err,i}$ .

In order to verify the proposed method, we tested it using simulated stochastic trajectories where the beads parameters and the force function  $F(x)$  are known precisely. We numerically simulated the stochastic trajectories using the approach introduced by Grønbech-Jensen [111, 112] and applied the proposed method to estimate the original force profile. In 1D the force field is conservative by definition so the mean velocity  $\langle v \rangle_i$  should be zero in all bins. This assumption proves true - the mean velocities calculated from one simulated trajectory are approximately zero within the respective errorbars (see Fig. 5.2a). So in 1D it is reasonable to omit the mean velocity term in equation (5.7) and estimate the force using only the mean

acceleration term as

$$\langle F \rangle_i = m \langle a \rangle_i. \quad (5.13)$$

As a test force field we picked the typical case of non-linear restoring force acting on a bead trapped in an optical tweezer. Here the force profile is of the Duffing form  $F = -m\Omega_0^2(1 + \xi x^2)x$ . The estimated force field is depicted in figure 5.2b. The solid line represent the original force field used in the simulation, the orange crosses are the estimated values. The agreement of estimated and original force profile is excellent. The estimation error is significant only for the peripheral bins where the number of samples used for averaging  $\mathcal{N}_i$  is on the order of units and the statistical error is high. As shown in figure 5.2c, the typical relative error  $\rho_{err,i} = \frac{u(\langle F \rangle_i)}{\langle F \rangle_i}$  for bins with good statistics is below  $\pm 0.5\%$ . We conclude that the proposed method provides high accuracy estimate of the optical force field on simulated data and becomes a promising universal and reliable tool for force fields characterization.

We show the performance of the method also on experimental data. We use the stochastic trajectory of a silica bead trapped in counterpropagating beams (experiment described in section 2). For the trap parameters used, the motion of the bead is well described as harmonic oscillator and the force is linear function of  $x$ . Note that in the linear case the force function can be determined from knowledge of the oscillators mass  $m$  and the natural frequency  $\Omega_0$  as  $F = -m\Omega_0^2 x$ . The binning method offers no advantage for the linear case since the natural frequency can be found by fitting the theoretical PSD function  $S_{xx}$  into the measured one and the mass needs to be known anyway. But the linear case offers the opportunity to verify the binning method even without the precise knowledge of the beads mass or even without precisely calibrated position measurement.

First, from the measured trajectory the natural frequency is determined. If the mass is not known, the binning method gives the average acceleration experienced by the bead passing certain bin (see Fig. 5.3):

$$\langle a_x \rangle_i = \Omega_0^2 \langle x \rangle_i, \quad (5.14)$$

with the slope corresponding to the natural frequency squared determined from PSD fitting [113]. Moreover, if the position measurement was badly calibrated and it was off by a factor  $C_{err}$ , the mean acceleration values estimated by binning would be

$$C_{err} \langle \ddot{x} \rangle_i = \Omega_0^2 C_{err} \langle x \rangle_i. \quad (5.15)$$

The bad calibration factors would cancel out and the binning method would again provide the correct value of  $\Omega_0$ .

Here we show the performance of our method by comparing the mean acceleration determined by binning and determined by fitting the PSD. We used one of the

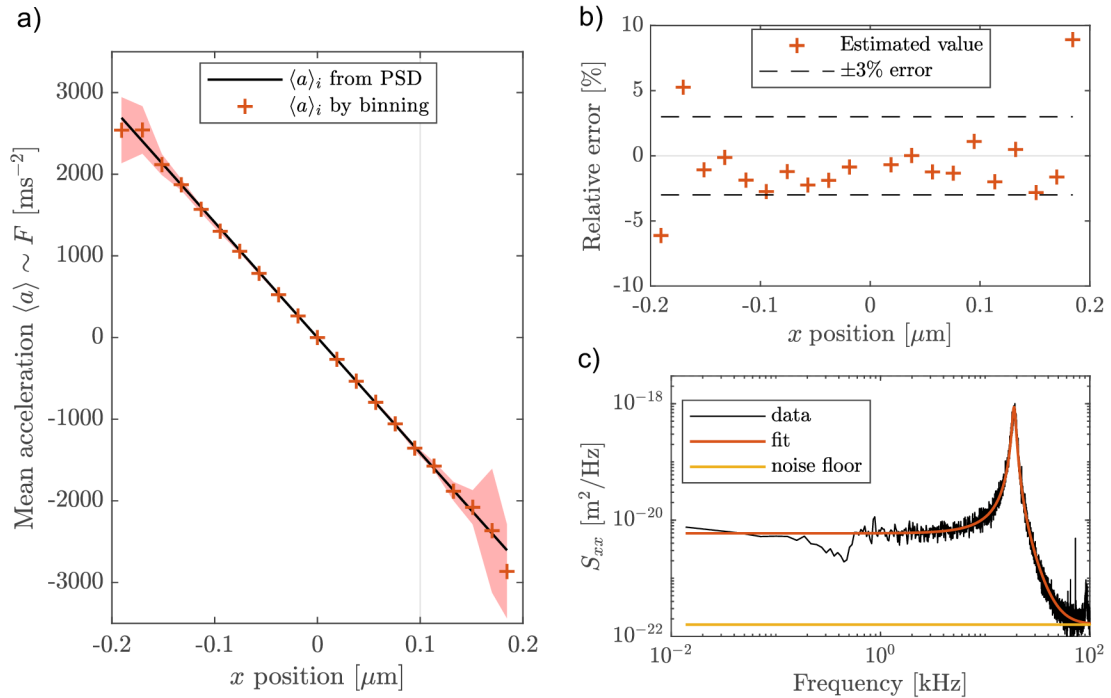


Fig. 5.3: Binning method performance on 1D experimental data. The trapping power was 175 mW and the motion was captured by videomicroscopy using fast camera with framerate of 200 000 fps. The recording was 0.7 s long and contained 138000 frames. The stochastic trajectory was tracked from the video recording by fitting 2D Gaussian distribution into the image of the trapped bead. The natural frequency of the oscillator  $\Omega_0$  was found by fitting the one-sided Power Spectral Density (PSD)  $S_{xx}$  by the theoretical function as described in Chapter 3, Supplementary note 5 (see Fig. 5.3c). Since the mass is not known, only the mean accelerations are plotted. (a) Black line - mean acceleration as suggested by the measured natural frequency of the oscillator. Orange crosses - mean accelerations estimated by binning. (b) Relative error of estimation. (c) One sided PSD function. Black curve - data. Red curve - theoretical fit. Yellow curve - position measurement noise floor.

measurements of particles motion in standing wave of counter-propagating beams published in our previous paper [83] (Chapter 3). The obtained value  $\frac{\Omega_0}{2\pi} = 18.9$  kHz was used for construction of the expected mean acceleration function  $\langle a_x \rangle = -\Omega_0^2 x$  which is plotted as the black line in Fig. 5.3a). The mean acceleration values obtained by binning are depicted in Fig. 5.3a) by orange crosses and the coincidence with the expected values is very good. The light red area in the figure represents the uncertainty of the estimated value defined by  $\langle a_x \rangle \pm \sigma$  with  $\sigma$  being the standard error of the mean calculated across the respective bin samples. As shown in Fig.

5.3b), the relative error is as small as 3% for majority of the bins. The error gets higher only for the outer bins, where the number of samples taking part in the averaging is very low (typically units of samples) and the uncertainty is high. Still, even though the statistics is so poor for these bins, the relative error is less than 10%. In this case, the precision of force measurement would be limited mainly by the precision of position detection calibration and the precision of knowledge of mass  $m$ .

### 5.3 Non-conservative force field - 2D case

The force field generated by optical trap can be in general non-conservative, for example due to the intrinsic properties of optical tweezers or bad alignment of a trap. A non-conservative force field can also be introduced on purpose by design of the trap itself in order to generate and study the non-equilibrium dynamics of the trapped bead. In either case, it is useful to have a method for characterization of the resulting force  $\mathbf{F}(\mathbf{r})$ , as introduced in eq. (5.1).

If a particle is subjected to a non-conservative force field, in general it does not reach thermal equilibrium with the surrounding gas. Instead it can reach a steady state, but this state is not described by the Gibbs-Boltzmann distribution anymore. It follows that mean velocity across one bin  $\langle \mathbf{v} \rangle_i$  does not need to be zero and the full version of equation (5.7) must be used. So if the force is estimated in 2D grid (illustrated in Fig. 5.4) of bins  $\mathbf{b}_i = (b_{x,i}, b_{y,i})$ , the estimated force becomes

$$\langle \mathbf{F} \rangle_i = \langle \mathbf{F} \rangle_i^{acc} + \langle \mathbf{F} \rangle_i^{vel} \quad (5.16)$$

with  $\langle \mathbf{F} \rangle_i^{acc} = m \langle \mathbf{a} \rangle_i$  being the mean acceleration part and  $\langle \mathbf{F} \rangle_i^{vel} = \gamma \langle \mathbf{v} \rangle_i$  the mean velocity part. We have shown experimentally in our recent publication [83] that such

$\mathbf{b}_1$	$\mathbf{b}_2$	$\mathbf{b}_3$	$\mathbf{b}_4$
$\mathbf{b}_5$	...	...	...
...	...	$\mathbf{b}_i$	...
...	...	...	...

Fig. 5.4: Illustration of labeling of bins  $\mathbf{b}_i$  in 2D grid.

out of equilibrium steady state can be reached in optical trap formed by circularly polarized counter-propagating beams in low pressure. In such trap the force field

is composed of strong radial component  $F_\rho$  generated by gradient forces and much weaker azimuthal component  $F_\phi$  generated mainly by spin force, which is connected to the circular polarization. The total force field have cylindrical symmetry. Since the stochastic motion remains restricted on one standing wave fringe in the axial direction, we performed 2D simulation of the stochastic trajectories in the radial plane and use them to investigate the binning method performance.

As mentioned earlier, the force value can be estimated only in bins, which are visited by the bead several times during its motion. For a certain trapping power  $P$  the motional steady state is realised by motion close to a stable orbital trajectory of radius  $\alpha$  and space further away or closer to the trap center is not reached at all. In order to explore the whole trap we performed simulations of 24 stochastic trajectories, each for different trapping power ranging from 25 mW to 105 mW. The radial span of trajectory for certain  $P$  overlaps with radial spans of trajectories for different  $P$ .

The optical force field was estimated in the following manner:

1. calculate the 2D force field in 2D rectangular mesh of bins for each trajectory separately, the position bins are the same for all trajectories. For each trajectory some bins remain blank since they are not visited by the bead
2. decompose the force field into radial  $\mathbf{F}_i^\rho(\rho)$  and azimuthal  $\mathbf{F}_i^\phi(\rho)$  component
3. calculate the radial  $F_\rho(\rho)$  and azimuthal  $F_\phi(\rho)$  component as a function of only radial position  $\rho$  by averaging across all bins, whose radial distance from trap center is in the interval  $(\rho; \rho + d\rho)$
4. divide the force components by the corresponding trapping power  $P$  to get the normalized optical force  $f = F/P$
5. average  $f_\rho(\rho)$  and  $f_\phi(\rho)$  to get the final normalized force components

The mean acceleration and mean velocity parts of the estimated force are depicted in figures 5.5a and 5.5b. In the figures, the black arrows denote the local force direction, the pseudocolor map encode the local force magnitude. At first glance it might seem that the mean acceleration part constitutes a curl-free radial field and the non-conservativeness is manifested only in the mean velocity part. But at closer look this impression proves wrong. Although the azimuthal component  $f_\phi$  is made up mainly by the mean velocity part (see Fig. 5.5d, black diamonds), the mean acceleration part also contributes to the total azimuthal force (red dots) by its nonzero component (Fig. 5.5d, blue dots). So the parts  $\langle \mathbf{F} \rangle^{acc}$  and  $\langle \mathbf{F} \rangle^{vel}$  cannot be considered the curl-free and solenoidal parts of the total force vector field in the sense of Helmholtz decomposition.

The estimated force values are compared to the original force used in simulation in Fig. 5.5c for the radial component and in figure 5.5d for the azimuthal component.

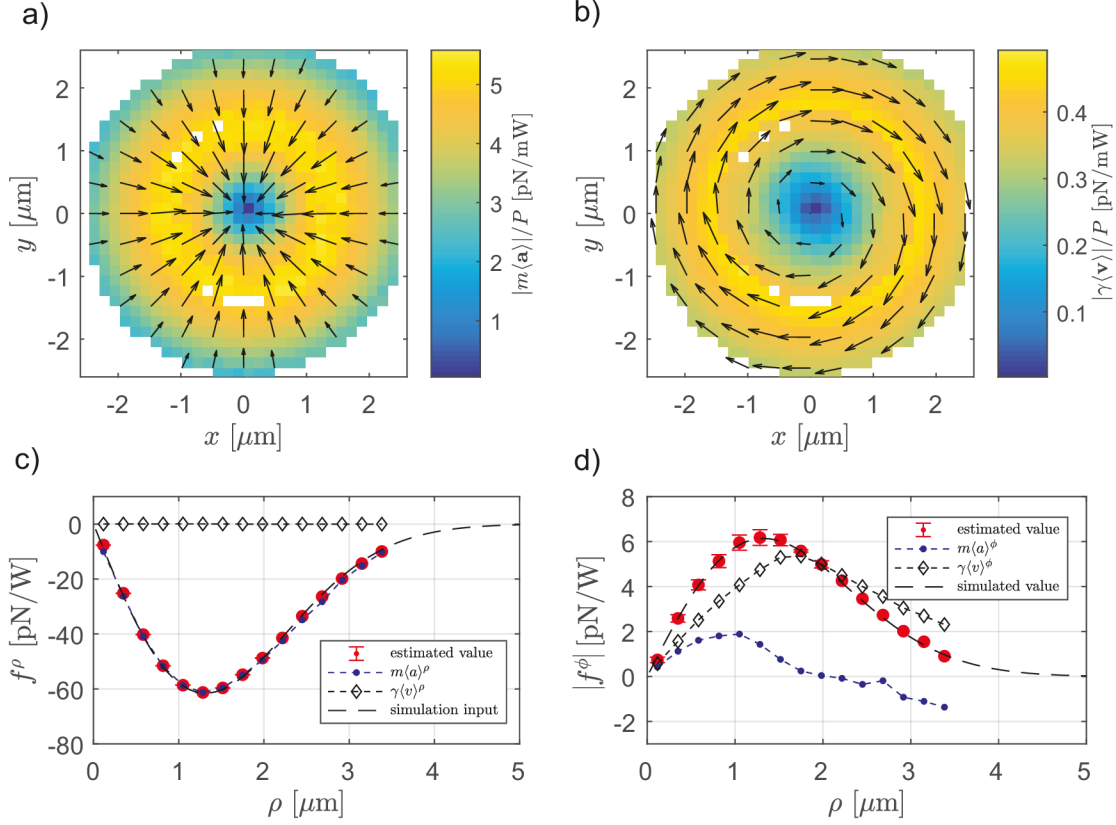


Fig. 5.5: Non-conservative 2D force field estimation from simulated stochastic trajectories. (a) Force field component corresponding to the mean acceleration  $m\langle\mathbf{a}\rangle$ . (b) Force field component corresponding to the mean acceleration  $\gamma\langle\mathbf{v}\rangle$ . (c) Normalized radial component of force field: black dashed curve - input force profile used in simulation. Red dot - estimated force value. Blue dot - radial component of  $m\langle\mathbf{a}\rangle$  part. Black diamond - radial part of  $\gamma\langle\mathbf{v}\rangle$  part. (d) Normalized azimuthal component of force field: black dashed line - force profile used in simulation. Red dot - estimated force value. Blue dot - azimuthal component of  $m\bar{\mathbf{a}}$  part. Black diamond - azimuthal part of  $\gamma\langle\mathbf{v}\rangle$  part.

The agreement of the estimation with the original force profile is again very good.

In order to show the performance of the method on experimental data we applied it on the measurements published in [[83]] and compared the force obtained by binning to the force published in the paper in Fig. 3c (Chapter 3 of this thesis).

Although the force field should be centrally symmetric, the estimated field is rather deformed. Which is expected since the observed orbital trajectories are not precisely circular and shows that the method is capable of mapping the real field instead of relying on some parametric approximate model. When we choose cer-



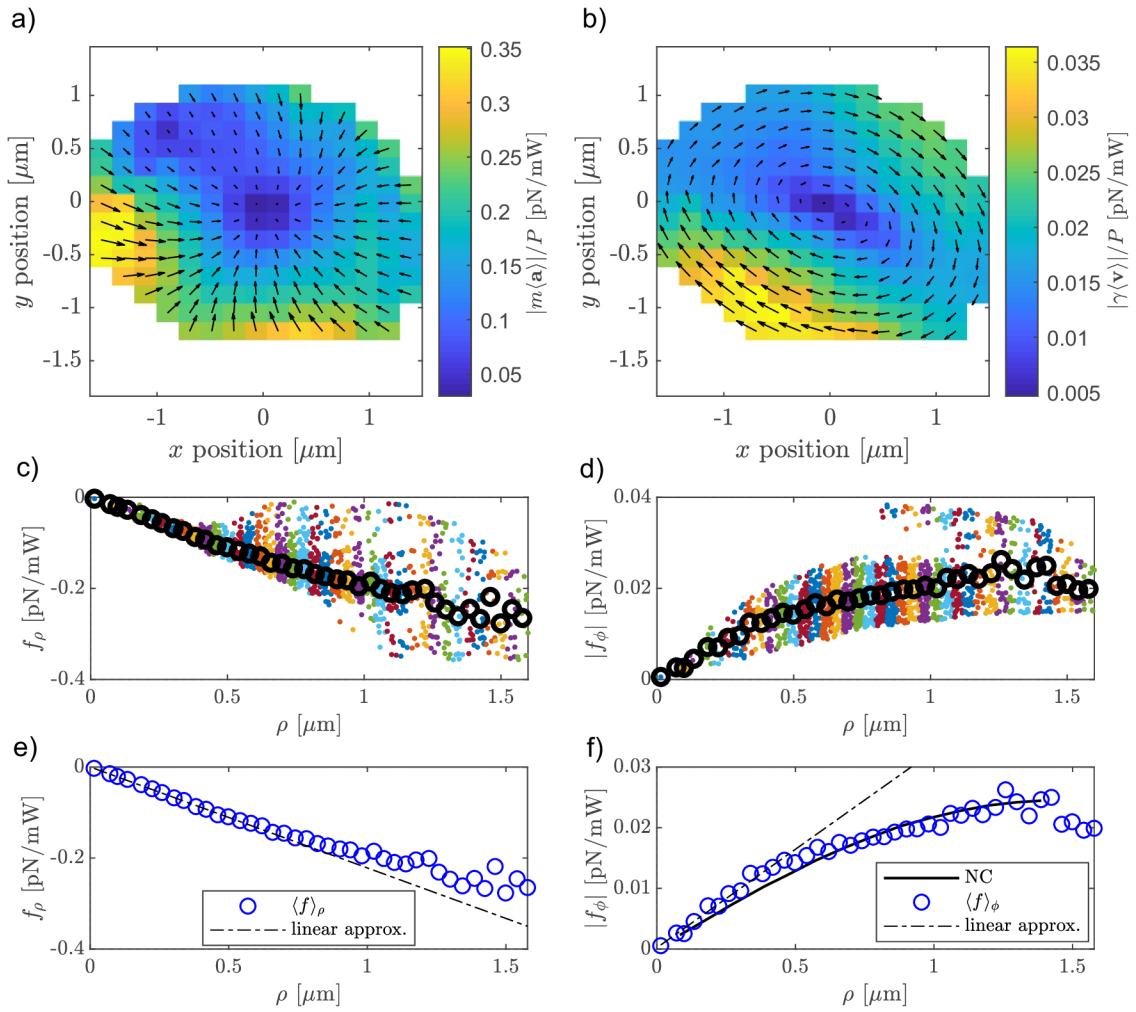


Fig. 5.6: Non-conservative force field estimation from experimental stochastic trajectories. (a) Mean acceleration component. (b) Mean velocity component. (c) Radial component of total force. The different color of datapoints indicate the different azimuthal positions across which the mean force  $f_\rho(r)$  (circles) is calculated. (d) Azimuthal component of total force. The color encoding is the same as in (c). (e) Estimated radial profile of the force field - radial component. (f) Estimated radial profile of the force field - azimuthal component. NC stands for data published in [83].

tain radial distance  $\rho$  from the trap axis the distribution of magnitude of the force components is quite broad for that  $\rho$  because of the force field asymmetry (see Fig. 5.6c,d). Nevertheless, taking the average values across the azimuthal coordinate produces the average radial force profile very similar to that shown in Chapter 3.

In Fig. 5.6f, there is the estimated azimuthal component (circles) which fits nicely the profile (solid black curve, NC) taken from Ref.[83]. We also fit the radial and azimuthal components by linear function for small radial displacement and express it in terms of radial stiffness  $k_\rho$  and azimuthal stiffness  $k_\phi$  and compare it to the values presented in Chapter 3 (see Tab. 5.1). The stiffnesses obtained by binning are very similar to those previously published, they only differ by units of percent.

Quantity	Binning	NatComm
$k_\phi$ [N/Wm]	$3.17 \times 10^{-5}$	$3.30 \times 10^{-5}$
$k_\rho$ [N/Wm]	$2.22 \times 10^{-4}$	$2.38 \times 10^{-4}$
$k_\rho/k_\phi$	0.146	0.138

Tab. 5.1: Comparison of stiffnesses obtained by binning method and those published in Ref. [83] (see Chapter 3).

In conclusion, the binning method provides correct force field estimate even for the non-conservative case as proved on 2D simulated trajectories. It proved itself also on experimental data where it reproduced the force field determined beforehand by different method. The presented binning method seems to fill the gap among the force measurement methods as listed in the beginning of this chapter.

## 5.4 Distortion of the estimated force caused by additive noise in position measurement

So far we silently assumed that the stochastic trajectories represent the stochastic motion precisely. It means, for example, that the quantization error caused by numerical representation of the position in numerical simulations is negligible. Or the error made in the position measurement process is also negligible. But this condition is rarely met in real world measurements.

The trapped beads position is most often measured using optical interferometric methods which lead to the instantaneous light intensity measurement. If the laser light used for detection suffers from intensity noise, this noise results in errors in the position measurement. Errors in position measurement are also caused by the electronic noise in the signal acquisition process and by the quantization of the analog signal into discrete values during digitization. We model all these effects by white noise term  $\zeta(t)$  added to the original stochastic trajectory. So the measured signal is given by the sum of the correct position  $x$  and a random noise value  $\zeta$ .

$$s(t) = x(t) + \zeta(t). \quad (5.17)$$

The noise process is characterized by single-sided PSD of value  $S_{\zeta\zeta}$  defined such that  $\int_0^\infty S_{\zeta\zeta}(\omega)d\omega = \sigma_\zeta$ . If the bandwidth of the position measurement is  $B = \frac{f_s}{2}$ , with  $f_s$  being the sampling frequency, the standard deviation of the noise values is  $\sigma_\zeta = \sqrt{BS_{\zeta\zeta}}$ .

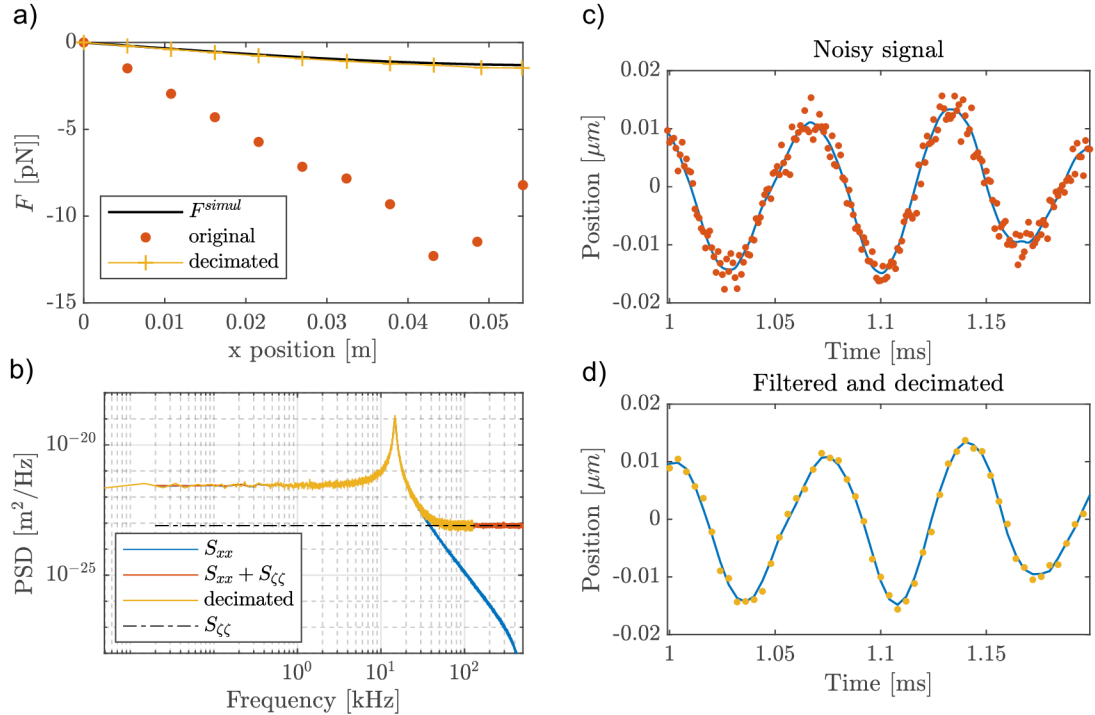


Fig. 5.7: Effect of additive white noise in position detection on the force estimation. (a) Black line is the simulated force profile which should be reproduced by the binning method. Orange dots - binning estimate from noisy trajectory, yellow crosses - binning estimate from noisy trajectory which was low-pass filtered and decimated. (b) PSDs of different position signals. Red - PSD of noisy signal, yellow - PSD of filtered and decimated signal, blue - PSD of the motion itself, black dashed line - additive noise floor. (c) Original noisy signal (orange dots) compared to the real trajectory (blue line). (d) Filtered signal (yellow dots) compared to the original trajectory.

Throughout this section we demonstrate the effects on the same simulated trajectory as was used in section 5.2, Fig. 5.2. The standard deviation of the beads position is  $\sigma_x = 12$  nm, the standard deviation of the added position white noise was  $\sigma_\zeta = 2$  nm.

In Fig. 5.7a we show the outcome of the binning procedure applied on a trajectory with additive noise (red dots). The estimated force values are several times lower than the real force profile (black curve), the relative error is in the order of

hundreds of percent. The situation can be elucidated a little by examining the PSD of noisy signal  $S_{xx} + S_{\zeta\zeta}$  compared to the original  $S_{xx}$  (Fig 5.7b). The high frequency end of the  $S_{rr}$  is constituted mainly by noise, it carries little information about the beads motion itself and including it into the binning procedure corrupts the estimation. In order to exclude this high frequency noise from the estimation we do the following operations on the experimental signal  $s(t)$ :

1. We perform zero-phase digital low-pass filtering. Namely we employ zero-phase low-pass IIR filtering procedure using 'filtfilt' function provided by Matlab.
2. We reduce the sampling rate of  $s(t)$  by an integer factor  $M$ , that means we keep only every  $M^{th}$  sample. We call this process *decimation*. So decimation by factor 5 means we keep every 5<sup>th</sup> sample, thus reducing the sample rate by a factor of 5.

So filtering out the high frequencies and decimating the signal should lower the error caused by noise. The output of binning performed on filtered and decimated data is shown in Fig. 5.7a (yellow crosses), the PSD in Fig. 5.7b (yellow) curve. The estimated values are significantly closer to the real value, but still the error is close to 10%.

The estimation could be improved further by setting the filter cut-off frequency even lower but for arbitrary force field and arbitrary PSD of motion it is not obvious, how to choose the right cut-off frequency to get rid of the noise and not to lose much information about the real motion. This is where the correction method, we propose in the following text, should be employed.

Let us now show, how the outcome of binning method is affected by the introduced noise. Firstly, the added noise changes the values of instantaneous velocity and acceleration, because these are calculated from the corrupted trajectory. Because differentiation is a linear transformation, the calculated velocity and acceleration waveforms become

$$v_n \equiv \dot{s}_n = \dot{x}_n + \dot{\zeta}_n \quad (5.18a)$$

$$a_n \equiv \ddot{s}_n = \ddot{x}_n + \ddot{\zeta}_n. \quad (5.18b)$$

Secondly, by adding the noise term, the way how are individual samples sorted into the bins - the  $I(\mathbf{b}_i, \mathbf{r}_n)$  function - is changed. For example, with zero noise the sample  $s_n = x_n$  would fall into the 10th bin  $b_{10}$ . But the noise term added to the real position can make the measured value bigger such that now the sample  $s_n = x_n + \zeta_n$  skips the bin edge and is wrongly included into the 11th bin  $b_{11}$ . The total effect is such that if we look at the samples falling into one certain bin  $b_i$ , some samples are included correctly, some samples are missing because they "leaked" into the surrounding bins and some sample are included incorrectly because they "leaked" into  $b_i$  from the surrounding bins.

There are five ways in which can certain sample be sorted into the bins due to the misclassification caused by noise. We will call these five ways the "processes".

1. Process I - the samples that leaked into  $b_i$  from bins of higher position coordinate, i.e. from bins  $b_j, j > i$
2. Process II - the samples that leaked from  $b_i$  into higher coordinate bins, i.e. into bins  $b_j, j > i$
3. Process III - the samples that leaked into  $b_i$  from bins of smaller position coordinate, i.e. from bins  $b_j, j < i$
4. Process IV - the samples that leaked from  $b_i$  into smaller coordinate bins, i.e. into bins  $b_j, j < i$
5. Process V / the samples that are classified correctly

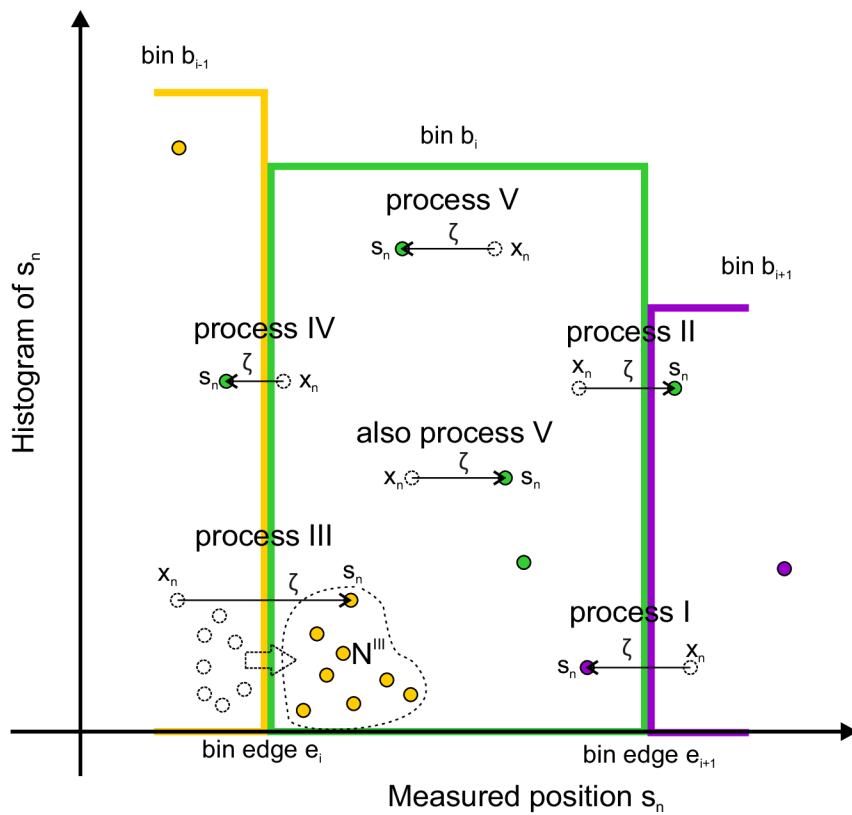


Fig. 5.8: Additive noise causes erroneous classification of measured position samples into bins.

For bin  $b_i$  we denote  $N_i^\alpha$  the number of samples taking part in process  $\alpha = I, II, III, IV, V$ . The symbol  $\sum X_i^\alpha$  means sum of quantity  $X$  (position, velocity, acceleration...) across the samples taking part in process  $\alpha$  in position bin  $b_i$ , e.g.  $\sum \ddot{\zeta}_5^{III}$  is the sum of second derivative of noise across samples involved in process III in bin  $b_5$ . The symbol  $\langle X \rangle_i^\alpha = \frac{\sum X_i^\alpha}{N_i^\alpha}$  means the mean value of quantity  $X$  calculated across

samples taking part in process  $\alpha$  in bin  $b_i$ .

With no noise in the measurement, there is only process V in all bins and the mean acceleration  $\langle a \rangle_i$  is given by

$$\langle a \rangle_i = \frac{\sum \ddot{x}_i^V}{N_i^V}. \quad (5.19)$$

If the noise is added, only samples of processes I, III and V are included, samples of process II and IV are missing and are not included into the averaging. The mean acceleration becomes

$$\langle a \rangle_i = \frac{\sum \ddot{r}_i^I + \sum \ddot{r}_i^{III} + \sum \ddot{r}_i^V}{N_i^I + N_i^{III} + N_i^V}. \quad (5.20)$$

and after plugging in equations (5.18)

$$\langle a \rangle_i = \frac{\sum \ddot{x}_i^I + \sum \ddot{x}_i^{III} + \sum \ddot{x}_i^V + \sum \ddot{\zeta}_i^I + \sum \ddot{\zeta}_i^{III} + \sum \ddot{\zeta}_i^V}{N_i^I + N_i^{III} + N_i^V}. \quad (5.21)$$

But the right mean value should be

$$\langle \ddot{x} \rangle_i = \frac{\sum \ddot{x}_i^{II} + \sum \ddot{x}_i^{IV} + \sum \ddot{x}_i^V}{N_i^{II} + N_i^{IV} + N_i^V}. \quad (5.22)$$

Therefore the experimental mean value  $\langle a \rangle_i$  is corrupted by all the extra noise terms and also by the  $\ddot{x}_i^I$  and  $\ddot{x}_i^{III}$  terms in equation (5.21). At the same time  $\ddot{x}_i^{II}$  and  $\ddot{x}_i^{IV}$  terms in equation (5.21) are missing. If we take  $\mathcal{N}_i = N_i^I + N_i^{III} + N_i^V$  and  $\mathcal{M}_i = N_i^{II} + N_i^{IV} + N_i^V$ , the experimental mean value can be written using the mean values calculated across the respective processes

$$\langle a \rangle_i = \frac{N_i^I}{\mathcal{N}_i} \langle \ddot{x} \rangle_i^I + \frac{N_i^{III}}{\mathcal{N}_i} \langle \ddot{x} \rangle_i^{III} + \frac{N_i^V}{\mathcal{N}_i} \langle \ddot{x} \rangle_i^V + \frac{N_i^I}{\mathcal{N}_i} \langle \ddot{\zeta} \rangle_i^I + \frac{N_i^{III}}{\mathcal{N}_i} \langle \ddot{\zeta} \rangle_i^{III} + \frac{N_i^V}{\mathcal{N}_i} \langle \ddot{\zeta} \rangle_i^V. \quad (5.23)$$

If we could estimate the mean values of second derivatives  $\langle \cdot \rangle_i^\alpha$  across all the processes, the experimental mean value would be corrected by adding and subtracting the mean values properly weighted by the number of samples  $N_i^\alpha$  taking part in the processes. The wanted true mean acceleration is

$$\langle \ddot{x} \rangle_i = \frac{1}{\mathcal{M}_i} \left( N_i^{II} \langle \ddot{x} \rangle_i^{II} + N_i^{IV} \langle \ddot{x} \rangle_i^{IV} + N_i^V \langle \ddot{x} \rangle_i^V \right). \quad (5.24)$$

Using equation (5.23) the last term can be expressed as

$$N_i^V \langle \ddot{x} \rangle_i^V = \mathcal{N}_i \langle a \rangle_i - \left[ N_i^I \left( \langle \ddot{x} \rangle_i^I + \langle \ddot{\zeta} \rangle_i^{II} \right) + N_i^{III} \left( \langle \ddot{x} \rangle_i^{III} + \langle \ddot{\zeta} \rangle_i^{III} \right) + N_i^V \langle \ddot{\zeta} \rangle_i^V \right] \quad (5.25)$$

The required mean values can be found provided the noise is white, additive and uncorrelated with the position  $x(t)$ . We will show the procedure for bin  $b_i$  and process III, the adaptation for other processes is straightforward. First, we calculate the mean value of the noise term, which is given by

$$\langle \ddot{\zeta} \rangle = \int_{-\infty}^{\infty} \ddot{\zeta} \cdot p(\ddot{\zeta} | s \in b_i) d\ddot{\zeta} \quad (5.26)$$

The function  $p(\ddot{\zeta}|s \in b_i)$  is the conditional probability density function of the second derivative of noise having the value  $\ddot{\zeta}$ , provided the additive noise caused particular sample to be included into the bin  $b_i$  instead of a bin  $b_j$  of lower index  $j < i$  (Process III). According to the law of total probability, this conditional probability can be written as the product of conditional probability of getting  $\ddot{\zeta}$  provided the noise value is  $\zeta$ , i.e.  $p(\ddot{\zeta}|\zeta)$ , and  $p(\zeta|s \in b_i)$  the probability of noise value being  $\zeta$  provided the measured position falls into the respective bin. The product then has to be integrated over all possible noise values

$$p(\ddot{\zeta}|s \in b_i) = \int_{-\infty}^{\infty} p(\ddot{\zeta}|\zeta) p(\zeta|s \in b_i) d\zeta. \quad (5.27)$$

The second order difference  $\ddot{\zeta}$  is calculated by three-point central formula stated in equation (5.5). The conditional probability  $p(\ddot{\zeta}|\zeta)$  is given by the marginal probability  $p(\zeta)$  of noise value being  $\zeta$  and the joint probability  $p(\zeta, \ddot{\zeta})$  of getting noise value  $\zeta$  and second-order difference  $\ddot{\zeta}$  at the same time, i.e.  $p(\ddot{\zeta}|\zeta) = \frac{p(\zeta, \ddot{\zeta})}{p(\zeta)}$ . It can be shown that joint probability is of the form

$$p(\ddot{\zeta}, \zeta) = \left(\frac{1}{\sqrt{2}}\right) \left(\frac{\Delta^2}{2\pi\sigma_\zeta^2}\right) \exp\left[-\frac{1}{2\sigma_\zeta^2} \left(3\ddot{\zeta}^2 + 2\ddot{\zeta}\Delta^2\zeta + \frac{1}{2}\Delta^4\zeta^2\right)\right], \quad (5.28)$$

if the noise values in the three consecutive time instants  $\zeta_{n-1}$ ,  $\zeta_n$  and  $\zeta_{n+1}$  are considered independent, normally distributed random variables (white noise), with identical mean values  $\mu_{n-1} = \mu_n = \mu_{n+1} = 0$  and standard deviations  $\sigma_{n-1} = \sigma_n = \sigma_{n+1} = \sigma_\zeta$ . The conditional probability  $p(\zeta|s \in b_i)$  is found by employing the Bayes theorem [114]

$$p(\zeta|s \in b_i) = \frac{p(s \in b_i|\zeta)p(\zeta)}{p(s \in b_i)} \quad (5.29)$$

so, the probability of noise having certain value  $\zeta$  provided the measured position value falls into  $b_i$  is derived by answering the inverse question, i.e. finding the probability that the measured position value falls into  $b_i$  provided the noise value is  $\zeta$ , which is straight forward. This inverse conditional probability is exactly the probability, that the sum of position coordinate and noise value  $s = x + \zeta$  falls into bin interval  $s \in (e_i; e_{i+1})$ , where  $e_i$  and  $e_{i+1}$  indicate the edges of bin  $b_i$  (see Fig. 5.1b). In another words, it is the probability of  $x \in (e_i - \zeta; e_{i+1} - \zeta)$

$$p(s \in b_i|\zeta) = \int_{e_i - \zeta}^{e_{i+1} - \zeta} p_i^{III}(x) dx. \quad (5.30)$$

Let us stress here that we are investigating specifically the process III for  $b_i$ , which can be realized only by samples fulfilling  $x_n < e_i$  and positive values of noise. This property is treated by defining

$$p_i^{III}(x) = \begin{cases} p(x), & \text{if } x \in (-\infty, e_i). \\ 0, & \text{otherwise,} \end{cases} \quad (5.31)$$

where  $p(x)$  is the probability density function of the bead having position  $x$  (see Fig. 5.9). This definition has to be changed accordingly for different process.

Here we would like to stress, that the probability density function of position,  $p(x)$ , is not known in general case. In the procedure we approximate it by the probability density function of the measured noisy signal  $s$ :

$$p(x) \approx p(s), \quad (5.32)$$

where  $p(s)$  is estimated as the properly normalized histogram of  $s_n$  values (see Fig. 5.10a for comparison of  $p(x)$  and  $p(s)$  ).

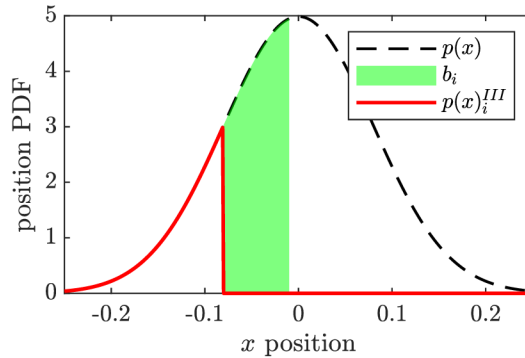


Fig. 5.9: Definition of quantity  $p_i^{III}(x)$  (red line) which is used in calculation of the probability of sample being misclassified into bin  $b_i$  instead of some lower index bin due to process III.

The white noise probability density function is a normal distribution with zero mean and standard deviation  $\sigma_\zeta$

$$p(\zeta) = \frac{1}{\sigma_\zeta \sqrt{2\pi}} e^{-\frac{\zeta^2}{2\sigma_\zeta^2}}. \quad (5.33)$$

Finally the term  $p(s \in b_i)$  in (5.29) is found by realizing that  $s$  is the sum of two independent random variables  $x$  and  $\zeta$ , so the probability density of getting  $s$  is the product of the two respective PDFs as  $p(s) = p(x + \zeta) = p(x)p(\zeta)$  and denominator of eq. (5.29) is calculated by integration over the domain fulfilling  $s \in b_i$

$$p^{III}(s \in b_i) = \int_{\zeta=-\infty}^{\zeta=\infty} \int_{e_i-\zeta}^{e_{i+1}-\zeta} p_i^{III}(x)p(\zeta)dx d\zeta. \quad (5.34)$$

The last ingredient missing is the number of samples taking part in the process  $\mathcal{N}_i^{III}$ . This number is given by the total number of samples  $\mathcal{N}$  and the probability that a sample is taking part in process III for bin  $b_i$ , which is given by  $p(s \in b_i)$  as defined by equation (5.34). So the searched number of samples is

$$\mathcal{N}_i^{III} = \mathcal{N}p(s \in b_i). \quad (5.35)$$



In this manner, all the noise contributions in equation (5.21) can be calculated and subtracted. From our experience just subtracting the noise contributions  $\ddot{\zeta}_i^\alpha$  provides substantial error reduction and such corrected mean acceleration (force) profile provides the initial estimate in the following steps. We label these corrected values  $\langle \ddot{x} \rangle_i^{sc}$ . To improve the correction even more the contributions containing the means of second derivative of position  $\langle \ddot{x} \rangle_i^\alpha$  are needed. These values cannot be calculated using some universal formula as it is for white noise (equation 5.28), but they are given by the force itself. We estimate the mean second derivatives as the value of  $\langle \ddot{x} \rangle_i^{sc}$  in position  $\langle x \rangle_i^\alpha$ . The value is obtained by linear interpolation between the neighboring values  $\langle \ddot{x} \rangle_i^{sc}$ . The mean coordinate  $\langle x \rangle_i^\alpha$  is given by

$$\langle x \rangle_i^\alpha = \int_{-\infty}^{\infty} xp^\alpha(x|s \in b_i)dx \quad (5.36)$$

where  $p^\alpha(x|r \in b_i)$  is the conditional probability that the position of the bead is  $x$  provided that the noisy signal is within the bin  $b_i$  and it is calculated for process  $\alpha$ .  $p^\alpha(x|r \in b_i)$  is calculated in the same manner as  $p(\zeta|r \in b_i)$  for the noise values defined by equation (5.29) and related. But again we stress that (5.29) shows the calculation for process III so  $p(\zeta|r \in b_i) \equiv p^{III}(\zeta|r \in b_i)$  in (5.29)).

Note that for the correction procedure the knowledge of the position probability density function  $p(x)$  is needed. But normally only the noisy measurement is available and only the probability density function of signal  $r$  can be estimated (for example by calculating the histogram). In our procedure we assume that the noise does not change  $p(x)$  much and we take  $p(x) \equiv p(r)$ . In Fig. 5.10a we show that it is the case for our example.

The correctness of the described procedure is shown here by performing it on a simulated stochastic trajectory with known added white noise. In such case the precise values of  $x_n$  and  $\zeta_n$  are known, the misclassification into bins and the resulting mean values can be precisely tracked, calculated and compared to the expected values described above. For this purpose we used the same simulated trajectory as was used in section 5.2, Fig. 5.2, the standard deviation of the added position white noise was  $\sigma_\zeta = 2$  nm. We show the results of this analysis for process III in Fig. 5.10. In Fig. 5.10b the theoretical number of samples taking part in process III is shown (solid curve) compared to the actual number of such samples (blue dots) as the process III was realized while evaluating the simulation with known noise values. In Fig. 5.10c the PDF of noise values realizing process III in bin 13 is plotted - the dashed line is the prediction according to equation (5.29), the orange dots represent the values as realized in the simulated case. Note that  $p(\zeta)^{III}$  is nonzero only for positive values of noise - this is consistent with the fact that process III is realized by datapoints leaking into  $b_{13}$  from places of smaller position coordinate by adding positive value of noise. In Fig. 5.10d we plot the PDF of the second derivative of

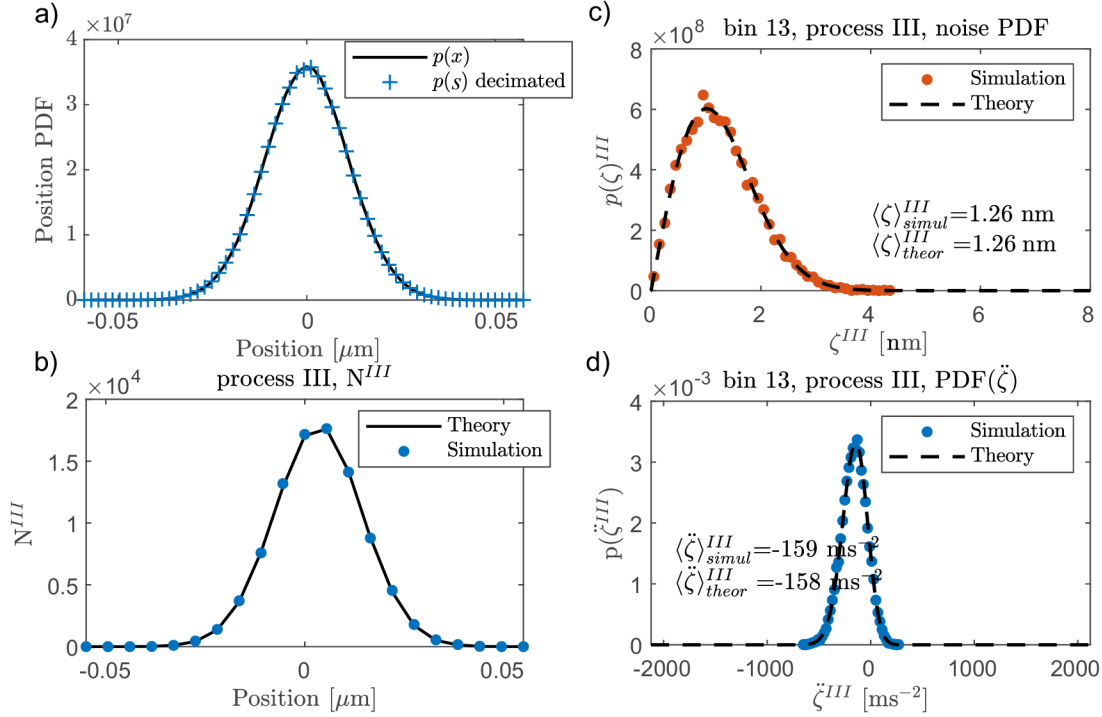


Fig. 5.10: Probability density functions used in correction procedure. (a) The original position PDF  $p(x)$  is practically identical to the approximate function  $p(r)$  estimated from noisy signal. (b) The expected number of samples (black curve) taking part in process III corresponds very well with simulation (blue dots). (c) Prediction of PDF of noise values taking part in process III in bin 13 as given by proposed calculation (dashed curve) corresponds well with the simulation (orange dots). (d) Prediction of PDF of the second derivative of noise values taking part in process III in bin 13 as given by proposed calculation (dashed curve) corresponds well with the simulation (blue dots).

noise taking part in process III as described by equation (5.27). The black dashed curve is the theoretical prediction, the blue dots are the values as realized in the simulation. All the theoretical PDFs and mean values fit the simulated analysis perfectly and so is the case for the rest of the bins which are not plotted here.

The corrected force profile is depicted in Fig. 5.11. Here the blue dots represent the original estimated profile after the trajectory was filtered and decimated by factor 4 (see Fig. 5.7a,b). The error is not as huge as without filtering, but it is still around 10% (see the inset in the figure). The corrected values (magenta crosses) are even closer to the simulated force profile and the estimation error is further reduced down to 3%.

In order to verify the correction procedure on experimental data we picked one

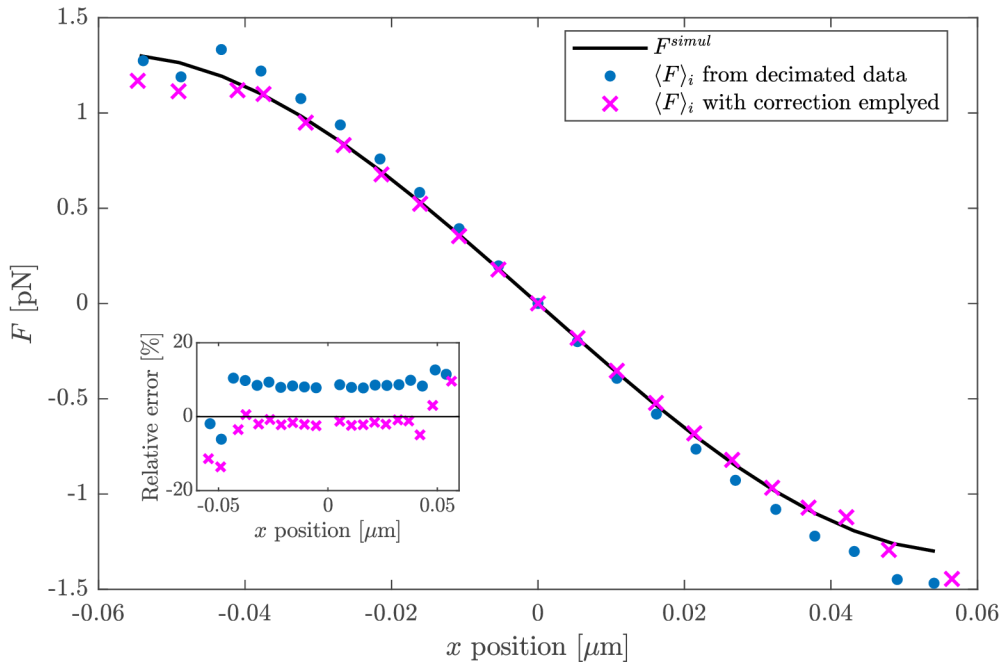


Fig. 5.11: Force profile estimated from simulated trajectory with additive noise without correction (blue dots) and when correction is employed (magenta crosses) compared to the original force profile (black curve). The inset depicts relative error of estimation.

experimental trajectory of beads motion in standing wave of counter-propagating beams optical trap similar to the one used in section 5.2, but in this case the trajectory was measured by back focal plane interferometry using quadrant photodiode. Here the position voltage signal is not calibrated so we used only the voltage signal  $q \propto s$  and its second derivative  $\ddot{q}$ . The PSD function of the voltage signal  $q$ ,  $S_{qq}$  has lorentzian shape typical for harmonic oscillator, but it settles to a flat plateau for frequencies over 70 kHz (see inset of Fig. 5.12). This means that for higher frequencies the measured signal is dominated by noise, but the same noise power is included in the whole frequency range, affecting the force estimation. Similarly to the simulated trajectory, most of the estimation error can be reduced by filtering and decimation of the stochastic trajectory to suitable sampling rate. We set the new sampling rate to frequency, for which the signal PSD  $S_{qq}$  is essentially equal to noise floor  $S_{\zeta\zeta}$  (see Fig. 5.12). This way we do not lose any information about the beads motion. In our case we filtered the signal by IIR filter of order 12 and half-power frequency  $f_{3dB} = 100$  kHz. Then we decimated the filtered signal by factor of 2 obtaining trajectory sampled with sampling frequency 100 kHz.

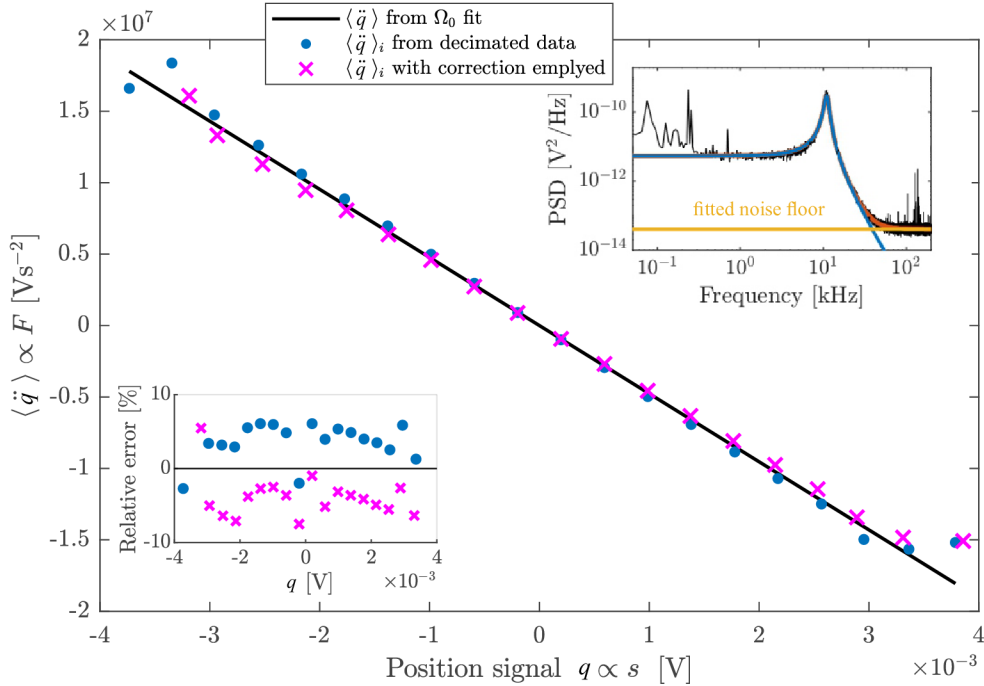


Fig. 5.12: Force profile estimated from experimentally measured trajectory with additive noise without correction (blue dots) and when correction is employed (magenta crosses) compared to the original force profile (black curve). Since particle mass and calibration are not known, only the mean second derivatives of signal in volts are plotted. The inset in lower left corner depicts relative error of estimation. The inset in upper right corner depicts the position signal PSD with black curve being the original data, blue curve the Lorentzian fit of  $S_{xx}$ , yellow curve the fitted noise floor  $S_{\zeta\zeta}$  and red curve the total fit of  $S_{xx} + S_{\zeta\zeta}$

In Fig. 5.12 the mean acceleration obtained by binning of the decimated data is shown (blue dots) and compared to the mean acceleration profile given by the oscillators natural frequency (black line) in the same manner as for the experimental data used in section 5.2. Using the filtered and decimated trajectory the binning method provides reasonably good estimation with positive relative error around 5%. The correction was performed also on decimated data, using  $\sigma_{\zeta}$  given by the noise floor estimated from the high frequency plateau of  $S_{qq}$ . The corrected mean acceleration values are depicted in Fig. 5.12 by magenta crosses. Compared to the uncorrected values, the correction shifts the mean acceleration closer to zero, but too much, ending up with negative relative error of about -5% and essentially not improving the estimation. This poor performance of the correction suggests that for

the used experimental trajectory the requirement of additive and white noise only is not met. It is apparent from the PSD of the signal (see inset of Fig. 5.12) that it contains substantial noise in the low frequency range (0-1 kHz). This noise is caused by surrounding acoustic noise and air drafts in the optical path of position detection beam. The effect of this low frequency noise on the binning procedure was not investigated so far and it is not incorporated into the correction procedure. We suspect this noise to corrupt the binning and correction procedure and limit the methods performance.

But even without correction, the error can still be reduced by improving the detection and reducing the additive noise. The method still keeps its priceless advantage of independence from the temperature  $T$  of the heat bath experienced by the bead. In real levitation experiments in vacuum this temperature is practically unknown and hard to measure. It was shown, that a bead levitated by laser beam absorbs some of the energy and gets hot. Depending on the pressure of the surrounding gas, the bead either heats up the gas in its near vicinity, or, in case of even lower pressure, it absorbs gas molecules of one (room) temperature, it heats them up and then desorbs those molecules of higher temperature [115]. Either way, the effective temperature is not the room temperature and it is not known.

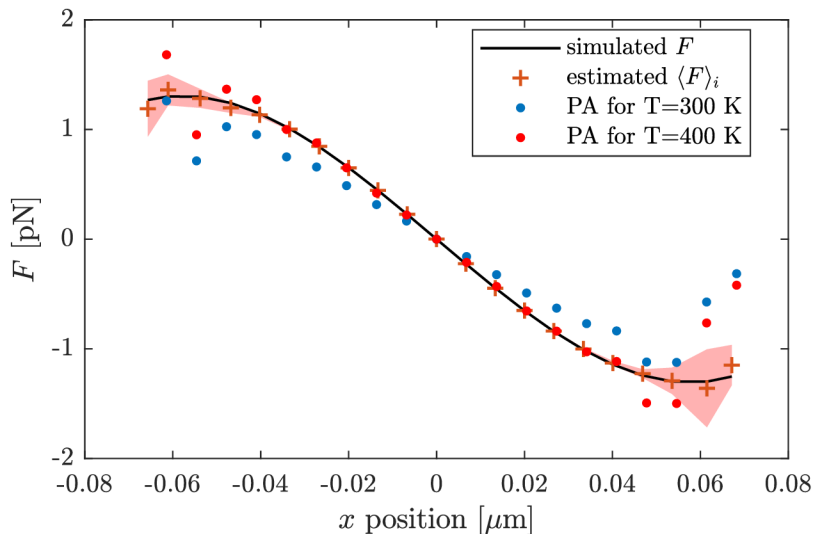


Fig. 5.13: Force profile estimated from stochastic trajectory simulated assuming the heat bath temperature  $T = 400K$ . The potential analysis (PA) performs well only if  $T$  is well known. The binning method does not use information about  $T$  at all.

One of the often used methods of trap calibration, the potential analysis, estimates the mechanical potential  $U(x)$  experienced by the bead as  $U(x) = -k_B T \log(p(x)) + U_0$  and the force is  $F = -\frac{dU(x)}{dt}$ . Here the error in  $F$  is proportional to the error in  $T$ .

This effect is illustrated in Fig. 5.13. Here, we used a stochastic trajectory, which was simulated assuming the heat bath temperature  $T = 400$  K. For this data, the potential analysis reproduces the force profile correctly, if the correct temperature is assumed (PA for  $T=400$  K). If room temperature is assumed wrongly (PA for  $T=300$  K) the error of force estimation is around 33%. On the other hand, the binning method performs great and even the 5% in this case would be better than potential analysis using wrong temperature.

## 5.5 Summary

In this chapter we introduced a powerful method for characterization of optical trap force fields acting on a probe particle. The method is based on analysis of the measured particles stochastic trajectory. Unlike other approaches, it does not assume special force field shape, conservativeness, thermal equilibrium steady state or certain temperature of the surrounding gas. The only assumption is under-damped dynamics of the trapped bead and knowledge of its mass and drag coefficient, thus making it ideal tool for characterization of optical traps in low pressure environment. The good performance of the proposed method was shown on both numerically simulated and experimental stochastic trajectories.

We also showed that additive white noise in position detection leads to an erroneous force estimation and that this error can be substantial even for relatively small noise levels. We showed that this error can be reduced significantly by proper low-pass filtering of the measured trajectory signal which cleans the signal of the frequency components that carry mostly noise and not much information about the probe particles motion. For 1D case, a correction procedure was presented which was shown to reduce the estimation error even more for simulated trajectory and exactly white noise. When used for experimental data, the correction procedure overestimated the error and did not improve the estimation which was caused, as we believe, by substantial low frequency  $1/f$  noise in the signal. In order to use the method correctly in experiment, one should pay attention to the position detection optimization. The  $1/f$  noise and white noise floor should be minimized while maximizing the signal. Also the measured signal should be appropriately low-pass filtered to get as precise estimate as possible.

In conclusion, we consider the proposed binning method a promising tool for characterization of complex 3D optical force fields. To our knowledge, it is the only method capable of estimation of non-conservative force fields from under-damped dynamics.

## 6 Conclusion

The presented doctoral thesis reports on development of experimental apparatus for optical trapping experiments at low pressure. Lowering the pressure enables us to reach under-damped regime of motion, control the stochastic forces acting on the particle or even minimize the coupling of the motion to the surrounding to the extent that quantum ground state of motion can be reached. Precisely engineering and controlling the optical trap allows to prepare and control out of equilibrium steady states of motion, making optical levitation suitable testbed for test of nonequilibrium thermodynamics. Levitated optomechanics is therefore very rapidly developing platform promising exciting discoveries not only in terms of fundamental questions classical and quantum physics, but mainly in terms of the transition between of those two. We believe the work presented in this thesis not only laid the foundations of experimental levitated optomechanics in the Institute of Scientific Instruments of the CAS, v.v.i., but also contributed experimentally to research of such phenomena as spin-force generated non-equilibrium states or optical binding in under-damped regime.

Since trapping in vacuum has never been realised before at the Institute of Scientific Instruments of the CAS, new optical trap and other necessary experimental methods such as optical setup adjustment, particle loading into the vacuum optical trap and tracking had to be developed. Chapter 2 shows how these issues were dealt with. We chose to implement dual-beam optical trap geometry due to its versatility. In the experiment we incorporated two particle position detection schemes - QPD detection and videomicroscopy. QPD provides us with real-time information of the position in 3D but it can be used for tracking only one particle. Also the determination of the calibration factor transforming the position signal from volts to meters is rather treacherous. Videomicroscopy on the other hand is able to capture position of several objects and the calibration is straightforward, but the information is extracted after measurement by postprocessing. Regarding the particle loading problem, two techniques were successfully developed. First technique uses an ultrasonic nebuliser for spraying little liquid droplets containing one particle into the trap under atmospheric conditions. Second technique, laser induced desorption, uses laser pulses to catapult particles from silicon wafer into the trap under vacuum conditions.

Chapter 3 presents our experimental observation of an optical force acting on trapped particle perpendicularly to light propagation direction which is generated by non-zero spin angular momentum of the optical field. The effect was shown by comparing the dynamics of probe particle trapped in linearly polarised (zero spin) and circularly polarised (maximal spin) light. We showed that spin force makes the

trapping force field non-conservative, it biases Brownian motion and drives it out of equilibrium. If the spin force is big enough, it induces orbital motion around optical axis and ultimately throws the probe particle from an optical trap.

Optical force fields are generally non-conservative, and their structure is derived from internal momentum flows. Measuring the trajectories of probe particles in vacuum can help us develop our understanding of optical momentum flows in structured light fields as well as the dynamics and thermodynamics associated with motion in potentially complex force fields. Some of these possibilities have previously been described by Berry and Shukla [116, 117].

Chapter 4 summarizes our recent effort in the field of optical binding. We successfully trapped two silica microspheres in free space dual-beam optical trap in vacuum, which is, to our knowledge, experimental arrangement never used before. In the under-damped motion of the trapped spheres we observed clear mode splitting proving the binding interaction between the particle. We also observed collisions of the spheres at pressures around 1 mbar suggesting that for reaching lower pressures, active feedback stabilization will be needed. Finally we introduced a method for characterization of the binding force based on calculation of local mean second derivative of the mode coordinate.

In chapter 5 the idea of binding force calculation was generalized to a method capable of calculating arbitrary optical force field using just the probe particles under-damped stochastic trajectory, mass and damping coefficient. We showed the performance of the method on both numerically simulated and experimental data. Although we admit that the method would need some mathematical polishing and detailed estimation error analysis, we believe that it can be useful tool for optical trap calibration, quality evaluation. For example, experiments studying thermodynamics could profit from this method since the work done along some trajectory is calculated from the knowledge of the local force.



## List of acronyms

<b>CCD</b>	charge-coupled device
<b>CMOS</b>	complementary metal-oxide-semiconductor
<b>DMD</b>	digital micro mirror device
<b>SLM</b>	spatial light modulator
<b>AOD</b>	acousto-optic deflector
<b>PSD</b>	power spectral density
<b>ACF</b>	auto-correlation function
<b>QPD</b>	quadrant photodetector
<b>SMOF</b>	single-mode optical fiber
<b>CAM</b>	camera
<b>COM</b>	center of mass (mode)
<b>BR</b>	breathing mode



# Bibliography

1. ASHKIN, A. Acceleration and Trapping of Particles by Radiation Pressure. *Phys. Rev. Lett.* 1970, **24**, 156–159.
2. MCGLOIN, D. Optical tweezers:20 years on. *Phil. Trans. R. Soc. A.* 2006, **364**, 3521–3537.
3. LANG, M. J.; BLOCK, S. M. Resource letter: LBOT-1: Laser-based optical tweezers. *Am. J. Phys.* 2003, **71**, 201–215.
4. MEHTA, A. D.; RIEF, M.; SPUDICH, J. A.; SMITH, D. A.; SIMMONS, R. M. Single-molecule biomechanics with optical methods. *Science.* 1999, **283**, 1689–1695.
5. BUSTAMANTE, C.; BRYANT, Z.; SMITH, S. B. Ten years of tension: single-molecule DNA mechanics. *Nature.* 2003, **421**, 423–427.
6. ASHKIN, A.; DZIEDZIC, J. M.; BJORKHOLM, J. E.; CHU, S. Observation of a single-beam gradient force optical trap for dielectric particles. *Opt. Lett.* 1986, **11**, 288–290.
7. GRIER, DG; ROICHMAN, Y. Holographic optical trapping. *Appl. Opt.* 2006, **45**(5), 880–887.
8. VISSCHER, K.; GROSS, S. P.; BLOCK, S. M. Construction of multiple-beam optical traps with nanometer-resolution position sensing. *IEEE J. Sel. Top. Quantum Electron.* 1996, **2**, 1066–1076.
9. BURNS, M. M.; FOURNIER, J.-M.; GOLOVCHENKO, J. A. Optical Matter: Crystallization and Binding in Intense Optical Fields. *Science.* 1990, **249**, 749.
10. CHIOU, A. E.; WANG, W.; SONEK, G. J.; HONG, J.; BERNS, M. W. Interferometric optical tweezers. *Opt. Commun.* 1997, **133**, 7–10.
11. CASABURI, A.; PESCE, G.; ZEMÁNEK, P.; SASSO, A. Two-and three-beam interferometric optical tweezers. *Opt. Commun.* 2005, **251**, 393–404.
12. ZEMÁNEK, P.; JONÁŠ, A.; ŠRÁMEK, L.; LIŠKA, M. Optical trapping of Rayleigh particles using a Gaussian standing wave. *Opt. Commun.* 1998, **151**, 273–285.
13. ZEMÁNEK, P.; JONÁŠ, A.; ŠRÁMEK, L.; LIŠKA, M. Optical trapping of nanoparticles and microparticles using Gaussian standing wave. *Opt. Lett.* 1999, **24**, 1448–1450.
14. ČIŽMÁR, T.; GARCÉS-CHÁVEZ, V.; DHOLAKIA, K.; ZEMÁNEK, P. Optical conveyor belt for delivery of submicron objects. *Appl. Phys. Lett.* 2005, **86**, 174101.

15. ČIŽMÁR, T.; ŠILER, M.; ZEMÁNEK, P. An optical nanotrap array movable over a millimetre range. *Appl. Phys. B*. 2006, **84**, 197–203.
16. KORDA, P. T.; TAYLOR, M. B.; GRIER, D. G. Kinetically locked-in colloidal transport in an array of optical tweezers. *Phys. Rev. Lett.* 2002, **89**, 128301.
17. MACDONALD, M. P.; SPALDING, G. C.; DHOLAKIA, K. Microfluidic sorting in an optical lattice. *Nature*. 2003, **426**, 421–424.
18. DHOLAKIA, K.; MACDONALD, M. P.; ZEMÁNEK, P.; ČIŽMÁR, T. Cellular and colloidal separation using optical forces. *Methods in Cell Biology*. 2007, **82**, 467–495.
19. ASHKIN, A.; DZIEDZIC, J. M. Optical levitation by radiation pressure. *Appl. Phys. Lett.* 1971, **19**, 283–285.
20. MCGLOIN, D.; BURNHAM, D. R.; SUMMERS, M. D.; RUDD, D.; DEWAR, N.; ANAND, S. Optical manipulation of airborne particles: techniques and applications. *Faraday Discuss.* 2008, **137**, 335–350.
21. BURNHAM, D. R.; MCGLOIN, D. Holographic optical trapping of aerosol droplets. *Opt. Express*. 2006, **14**, 4176.
22. SUMMERS, M. D.; BURNHAM, D. R.; MCGLOIN, D. Trapping solid aerosols with optical tweezers: A comparison between gas and liquid phase optical traps. *Opt. Express*. 2008, **16**, 7739.
23. MITCHEM, L.; HOPKINS, R. J.; BUJARERN, J.; WARD, A. D.; REID, J. P. Comparative measurements of aerosol droplet growth. *Chem. Phys. Lett.* 2006, **432**, 362–366.
24. KING, Martin D.; THOMPSON, Katherine C.; WARD, Andrew D.; PFRANG, Christian; HUGHES, Brian R. Oxidation of biogenic and water-soluble compounds in aqueous and organic aerosol droplets by ozone: a kinetic and product analysis approach using laser Raman tweezers. *Faraday Discuss.* 2008, **137**, 173–192. ISSN 1364-5498.
25. MITCHEM, L.; REID, J. P. Optical manipulation and characterisation of aerosol particles using a single-beam gradient force optical trap. *Chem. Soc. Rev.* 2008, **37**, 756–769.
26. ROOSEN, G.; IMBERT, C. Optical levitation by means of two horizontal laser beams: a theoretical and experimental study. *Phys. Lett.* 1976, **59A**, 6–8.
27. ROOSEN, G. A theoretical and experimental study of the stable equilibrium positions of spheres levitated by two horizontal laser beams. *Opt. Commun.* 1977, **21**, 189–194.

28. TAJI, K.; TACHIKAWA, M.; NAGASHIMA, K. Laser trapping of ice crystals. *Appl. Phys. Lett.* 2006, **88**, 141111.
29. PASTEL, R; STRUTHERS, A; RINGLE, R; ROGERS, J; ROHDE, C; GEISER, P. Laser trapping of microscopic particles for undergraduate experiments. *Am. J. Phys.* 2000, **68**(11), 993–1001. ISSN 0002-9505.
30. GUILLON, M.; MOINE, O.; STOUT, B. Longitudinal optical binding of high optical contrast microdroplets in air. *Phys. Rev. Lett.* 2006, **96**, 143902.
31. MILLEN, J.; DEESUWAN, T.; BARKER, P.; ANDERS, J. Nanoscale temperature measurements using non-equilibrium Brownian dynamics of a levitated nanosphere. *Nature Nanotechnology.* 2014, **9**, 425 EP –.
32. FRIMMER, Martin; GIESELER, Jan; IHN, Thomas; NOVOTNY, Lukas. Levitated nanoparticle as a classical two-level atom. *J. Opt. Soc. Am. B.* 2017, **34**(6), C52–C57.
33. RASHID, Muddassar; TUFARELLI, Tommaso; BATEMAN, James; VOVROSH, Jamie; HEMPSTON, David; KIM, M. S.; ULBRICHT, Hendrik. Experimental Realization of a Thermal Squeezed State of Levitated Optomechanics. *Phys. Rev. Lett.* 2016, **117**, 273601.
34. LI, Tongcang; KHEIFETS, Simon; RAIZEN, Mark G. Millikelvin cooling of an optically trapped microsphere in vacuum. *Nat. Phys.* 2011, **7**(7), 527–530.
35. GIESELER, Jan; DEUTSCH, Bradley; QUIDANT, Romain; NOVOTNY, Lukas. Subkelvin Parametric Feedback Cooling of a Laser-Trapped Nanoparticle. *Phys. Rev. Lett.* 2012, **109**(10).
36. DELIĆ, Uroš; REISENBAUER, Manuel; DARE, Kahan; GRASS, David; VULETIĆ, Vladan; KIESEL, Nikolai; ASPELMEYER, Markus. Cooling of a levitated nanoparticle to the motional quantum ground state. *Science.* 2020, **367**(6480), 892–895.
37. MAGRINI, Lorenzo; ROSENZWEIG, Philipp; BACH, Constanze; DEUTSCHMANN-OLEK, Andreas; HOFER, Sebastian G.; HONG, Sungkun; KIESEL, Nikolai; KUGI, Andreas; ASPELMEYER, Markus. Real-time optimal quantum control of mechanical motion at room temperature. *Nature.* 2021, **595**(7867), 373–377.
38. HOANG, Thai M.; MA, Yue; AHN, Jonghoon; BANG, Jaehoon; ROBICHEAUX, F.; YIN, Zhang-Qi; LI, Tongcang. Torsional Optomechanics of a Levitated Nonspherical Nanoparticle. *Phys. Rev. Lett.* 2016, **117**, 123604.

39. KUHN, Stefan; KOSLOFF, Alon; STICKLER, Benjamin A.; PATOLSKY, Fernando; HORNBERGER, Klaus; ARNDT, Markus; MILLEN, James. Full rotational control of levitated silicon nanorods. *Optica*. 2017, **4**(3), 356–360.
40. REIMANN, René; DODERER, Michael; HEBESTREIT, Erik; DIEHL, Rozenn; FRIMMER, Martin; WINDEY, Dominik; TEBBENJOHANNNS, Felix; NOVOTNY, Lukas. GHz Rotation of an Optically Trapped Nanoparticle in Vacuum. *Phys. Rev. Lett.* 2018, **121**, 033602.
41. GIESELER, Jan; NOVOTNY, Lukas; QUIDANT, Romain. Thermal nonlinearities in a nanomechanical oscillator. *Nature Physics*. 2013, **9**, 806 EP –. Article.
42. RICCI, F.; RICA, R. A.; SPASENOVIC, M.; GIESELER, J.; RONDIN, L.; NOVOTNY, L.; QUIDANT, R. Optically levitated nanoparticle as a model system for stochastic bistable dynamics. *Nature Communications*. 2017, **8**, 15141. Article.
43. ASPELMEYER, Markus; KIPPENBERG, Tobias J.; MARQUARDT, Florian. Cavity optomechanics. *Reviews of Modern Physics*. 2014, **86**, 1391–1452.
44. ROMERO-ISART, Oriol; JUAN, Mathieu L; QUIDANT, Romain; CIRAC, J Ignacio. Toward quantum superposition of living organisms. *New Journal of Physics*. 2010, **12**(3), 033015.
45. ROMERO-ISART, O.; PFLANZER, A. C.; JUAN, M. L.; QUIDANT, R.; KIESEL, N.; ASPELMEYER, M.; CIRAC, J. I. Optically levitating dielectrics in the quantum regime: Theory and protocols. *Phys. Rev. A*. 2011, **83**, 013803.
46. RANJIT, Gambhir; CUNNINGHAM, Mark; CASEY, Kirsten; GERACI, Andrew A. Zeptonewton force sensing with nanospheres in an optical lattice. *Phys. Rev. A*. 2016, **93**, 053801.
47. XU, Zhujing; LI, Tongcang. Detecting Casimir torque with an optically levitated nanorod. *Phys. Rev. A*. 2017, **96**, 033843.
48. HOANG, Thai M.; PAN, Rui; AHN, Jonghoon; BANG, Jaehoon; QUAN, H. T.; LI, Tongcang. Experimental Test of the Differential Fluctuation Theorem and a Generalized Jarzynski Equality for Arbitrary Initial States. *Phys. Rev. Lett.* 2018, **120**, 080602.
49. BÉRUT, Antoine; ARAKELYAN, Artak; PETROSYAN, Artyom; CILIBERTO, Sergio; DILLENCHNEIDER, Raoul; LUTZ, Eric. Experimental verification of Landauer’s principle linking information and thermodynamics. *Nature*. 2012, **483**(7388), 187–189.

50. SCHMIEDL, T.; SEIFERT, U. Efficiency at maximum power: An analytically solvable model for stochastic heat engines. *EPL (Europhysics Letters)*. 2007, **81**(2), 20003.
51. DHOLAKIA, Kishan; ZEMÁNEK, Pavel. Colloquium: Grippled by light: Optical binding. *Reviews of modern physics*. 2010, **82**(2), 1767.
52. ARNDT, Markus; HORNBURGER, Klaus. Testing the limits of quantum mechanical superpositions. *Nature Physics*. 2014, **10**(4), 271–277. ISSN 1745-2481.
53. ASHKIN, A.; DZIEDZIC, J. M.; BJORKHOLM, J. E.; CHU, S. Observation of a Single-Beam Gradient Force Optical Trap for Dielectric Particles. *Opt. Lett.* 1986, **11**(5), 288–290.
54. HARADA, Y.; ASAKURA, T. Radiation forces on a dielectric sphere in the Rayleigh scattering regime. *Opt. Commun.* 1996, **124**, 529–541.
55. ASHKIN, A.; DZIEDZIC, J. M. Optical Levitation by Radiation Pressure. *Appl. Phys. Lett.* 1971, **19**(8), 283.
56. ASHKIN, A.; DZIEDZIC, J. M.; BJORKHOLM, J. E.; CHU, Steven. Observation of a single-beam gradient force optical trap for dielectric particles. *Opt. Lett.* 1986, **11**(5), 288–290.
57. ROOSEN, G.; IMBERT, C. Optical levitation by means of two horizontal laser beams: A theoretical and experimental study. *Physics Letters A*. 1976, **59**(1), 6–8.
58. ZEMÁNEK, Pavel; JONÁŠ, Alexandr; ŠRÁMEK, Libor; LIŠKA, Miroslav. Optical trapping of nanoparticles and microparticles by a Gaussian standing wave. *Opt. Lett.* 1999, **24**(21), 1448–1450.
59. ZEMÁNEK, Pavel; JONÁŠ, Alexandr; LIŠKA, Miroslav. Simplified description of optical forces acting on a nanoparticle in the Gaussian standing wave. *J. Opt. Soc. Am. A*. 2002, **19**(5), 1025–1034.
60. ČIŽMÁR, T.; ŠILER, M.; ZEMÁNEK, P. An optical nanotrap array movable over a millimetre range. *Applied Physics B*. 2006, **84**(1), 197–203.
61. ŠILER, M.; ČIŽMÁR, T.; ŠERÝ, M.; ZEMÁNEK, P. Optical forces generated by evanescent standing waves and their usage for sub-micron particle delivery. *Appl. Phys. B*. 2006, **84**, 157–165.
62. ŠILER, Martin; ČIŽMÁR, Tomáš; JONÁŠ, Alexandr; ZEMÁNEK, Pavel. Surface delivery of a single nanoparticle under moving evanescent standing-wave illumination. *New. J. Phys.* 2008, **10**, 113010:1–16.

63. PRALLE, A.; PRUMMER, M.; FLORIN, E.L.; STELZER, E.H.K.; HÖRBER, J.K.H. Three-dimensional high-resolution particle tracking for optical tweezers by forward scattered light. *Microsc. Res. Tech.* 1999, **44**(5), 378–386.
64. GITTES, Frederick; SCHMIDT, Christoph F. Interference model for back-focal-plane displacement detection in optical tweezers. *Opt. Lett.* 1998, **23**(1), 7–9.
65. ROHRBACH, Alexander; STELZER, Ernst H. K. Three-dimensional position detection of optically trapped dielectric particles. *Journal of Applied Physics.* 2002, **91**(8), 5474–5488.
66. TAY, Jian Wei; HSU, Magnus T. L.; BOWEN, Warwick P. Quantum limited particle sensing in optical tweezers. *Phys. Rev. A.* 2009, **80**, 063806.
67. TOLIĆ-NØRRELYKKE, Simon F; SCHÄFFER, Erik; HOWARD, Jonathon; PAVONE, Francesco S; JÜLICHER, Frank; FLYVBJERG, Henrik. Calibration of optical tweezers with positional detection in the back focal plane. *Rev. Sci. Instrum.* 2006, **77**(10), 103101.
68. HEBESTREIT, Erik; FRIMMER, Martin; REIMANN Renéand Dellago, Christoph; RICCI, Francesco; NOVOTNY, Lukas. Calibration and energy measurement of optically levitated nanoparticle sensors. *Review of Scientific Instruments.* 2018, **89**(3), 033111.
69. CHEONG, Fook Chiong; KRISHNATREYA, Bhaskar Jyoti; GRIER, David G. Strategies for three-dimensional particle tracking with holographic video microscopy. *Opt. Express.* 2010, **18**(13), 13563–13573.
70. LEE, Sang-Hyuk; GRIER, David G. Holographic microscopy of holographically trapped three-dimensional structures. *Opt. Express.* 2007, **15**(4), 1505–1512.
71. KRISHNATREYA, Bhaskar Jyoti; COLEN-LANDY, Arielle; HASEBE, Paige; BELL, Breanna A.; JONES, Jasmine R.; SUNDA-MEYA, Anderson; GRIER, David G. Measuring Boltzmann’s constant through holographic video microscopy of a single colloidal sphere. *American Journal of Physics.* 2014, **82**(1), 23–31.
72. MOYSES, Henrique W.; KRISHNATREYA, Bhaskar J.; GRIER, David G. Robustness of Lorenz-Mie microscopy against defects in illumination. *Opt. Express.* 2013, **21**(5), 5968–5973.
73. FORTES, F.J.; LASERNA, J.J. Characteristics of solid aerosols produced by optical catapulting studied by laser-induced breakdown spectroscopy. *Applied Surface Science.* 2010, **256**(20), 5924 –5928.



74. KONONENKO, T. V.; ALLONCLE, P.; KONOV, V. I.; SENTIS, M. Laser transfer of diamond nanopowder induced by metal film blistering. *Applied Physics A*. 2009, **94**(3), 531–536.
75. DOW, Alex R.; WITTRIG, Ashley M.; KENTTÄMAA, Hilka I. Laser-Induced Acoustic Desorption Mass Spectrometry. *European Journal of Mass Spectrometry*. 2012, **18**(2), 77–92.
76. BEKSHAEV, Aleksandr; BLIOKH, Konstantin Y.; SOSKIN, Marat. Internal flows and energy circulation in light beams. *J. Opt.* 2011, **13**(5), 053001.
77. BERRY, M. V. Optical currents. *J. Opt. A*. 2009, **11**(9), 094001.
78. BLIOKH, Konstantin Y.; BEKSHAEV, Aleksandr Y.; NORI, Franco. Extraordinary momentum and spin in evanescent waves. *Nat. Commun.* 2014, **5**, 3300.
79. NEUGEBAUER, Martin; BAUER, Thomas; AIELLO, Andrea; BANZER, Peter. Measuring the Transverse Spin Density of Light. *Phys. Rev. Lett.* 2015, **114**(6). ISSN 0031-9007.
80. BETH, RA. Mechanical detection and measurement of the angular momentum of light. *Phys. Rev.* 1936, **50**(2), 115–125. ISSN 0031-899X. Available from DOI: 10.1103/PhysRev.50.115.
81. BARNETT, Stephen M.; ALLEN, L.; CAMERON, Robert P.; GILSON, Claire R.; PADGETT, Miles J.; SPEIRITS, Fiona C.; YAO, Alison M. On the natures of the spin and orbital parts of optical angular momentum. *J. Opt.* 2016, **18**(6), 064004.
82. BLIOKH, Konstantin Y.; BEKSHAEV, Aleksandr Y.; NORI, Franco. Dual electromagnetism: helicity, spin, momentum, and angular momentum. *New. J. Phys.* 2013, **15**, 033026. ISSN 1367-2630.
83. SVAK, V.; BRZOBOHATÝ, O.; SILER, M.; JÁKL, P.; KANKA, J.; ZEMÁNEK, P.; SIMPSON, S. H. Transverse spin forces and non-equilibrium particle dynamics in a circularly polarized vacuum optical trap. *Nature Communications*. 2018, **9**(1), 5453.
84. ANTOGNOZZI, M.; BERMINGHAM, C. R.; HARNIMAN, R. L.; SIMPSON, S.; SENIOR, J.; HAYWARD, R.; HOERBER, H.; DENNIS, M. R.; BEKSHAEV, A. Y.; BLIOKH, K. Y.; NORI, F. Direct measurements of the extraordinary optical momentum and transverse spin-dependent force using a nano-cantilever. *Nat. Phys.* 2016, **12**(8), 731–735.

85. LIU, Lulu; DI DONATO, Andrea; GINIS, Vincent; KHEIFETS, Simon; AMIRZHAN, Arman; CAPASSO, Federico. Three-Dimensional Measurement of the Helicity-Dependent Forces on a Mie Particle. *Phys. Rev. Lett.* 2018, **120**(22), 223901.
86. ALBALADEJO, Silvia; MARQUES, Manuel I.; LAROCHE, Marine; SAENZ, Juan Jose. Scattering Forces from the Curl of the Spin Angular Momentum of a Light Field. *Phys. Rev. Lett.* 2009, **102**(11), 113602. ISSN 0031-9007.
87. SIMPSON, Stephen H.; HANNA, Simon. Orbital motion of optically trapped particles in Laguerre–Gaussian beams. *J. Opt. Soc. Am. A.* 2010, **27**(9), 2061–2071.
88. JONES, Philip H.; MARAGÒ, Onofrio M.; VOLPE, Giovanni. *Optical Tweezers: Principles and Applications*. Cambridge University Press, 2015.
89. BEKSHAEV, A Ya. Subwavelength particles in an inhomogeneous light field: optical forces associated with the spin and orbital energy flows. *Journal of Optics*. 2013, **15**(4), 044004.
90. THIRUNAMACHANDRAN, T. Intermolecular interactions in the presence of an intense radiation field. *Molecular Physics*. 1980, **40**, 393–399.
91. BURNS, M. M.; FOURNIER, J.-M.; GOLOVCHENKO, J. A. Optical Binding. *Phys. Rev. Lett.* 1989, **63**, 1233–1236.
92. TATARKOVA, S. A.; CARRUTHERS, A. E.; DHOLAKIA, K. One-Dimensional Optically Bound Arrays of Microscopic Particles. *Phys. Rev. Lett.* 2002, **89**, 283901.
93. SINGER, W.; FRICK, M.; BERNET, S.; RITSCH-MARTE, M. Self-organized array of regularly spaced microbeads in a fiber-optical trap. *J. Opt. Soc. Am. B.* 2003, **20**, 1568–1574.
94. KARÁSEK, V; ČIŽMÁR, T; BRZOBOHATÝ, O; ZEMÁNEK, P; GARCÉS-CHÁVEZ, V; DHOLAKIA, K. Long-range one-dimensional longitudinal optical binding. *Physical review letters*. 2008, **101**(14), 143601.
95. SIMPSON, Stephen H; ZEMÁNEK, Pavel; MARAGÒ, Onofrio M; JONES, Philip H; HANNA, Simon. Optical binding of nanowires. *Nano letters*. 2017, **17**(6), 3485–3492.
96. ARITA, Yoshihiko; WRIGHT, Ewan M.; DHOLAKIA, Kishan. Optical binding of two cooled micro-gyroscopes levitated in vacuum. *Optica*. 2018, **5**(8), 910–917.

97. BYKOV, Dmitry S.; XIE, Shangran; ZELTNER, Richard; MACHNEV, Andrey; WONG, Gordon K. L.; EUSER, Tijmen G.; RUSSELL, Philip St J. Long-range optical trapping and binding of microparticles in hollow-core photonic crystal fibre. *Light: Science & Applications*. 2018, **7**(1), 22.
98. BRZOBOHATÝ, Oto; CHVÁTAL, Lukáš; ZEMÁNEK, Pavel. Optomechanical properties of optically self-arranged colloidal waveguides. *Opt. Lett.* 2019, **4**(3), 707–710.
99. SVAK, Vojtěch; FLAJŠMANOVÁ, Jana; CHVÁTAL, Lukáš; ŠILER, Martin; JONÁŠ, Alexandr; JEŽEK, Jan; SIMPSON, Stephen H.; ZEMÁNEK, Pavel; BRZOBOHATÝ, Oto. Stochastic dynamics of optically bound matter levitated in vacuum. *Optica*. 2021, **8**(2), 220–229.
100. SINGH, Rajesh; GHOSH, Dipanjan; ADHIKARI, R. Fast Bayesian inference of the multivariate Ornstein-Uhlenbeck process. *Phys. Rev. E*. 2018, **98**, 012136.
101. RICHLY, Maximilian; TÜRKCAN, Silvan; LE GALL, Antoine; FISZMAN, Nicolas; MASSON, jean-baptiste; WESTBROOK, Nathalie; PERRONET, Karen; ALEXANDROU, Antigoni. Calibrating optical tweezers with Bayesian inference. *Optics express*. 2013, **21**, 31578–90.
102. EL BEHEIRY, Mohamed; TÜRKCAN, Silvan; RICHLY, Maximilian; ANTOINE, Triller; ALEXANDROU, Antigoni; DAHAN, Maxime; MASSON, jean-baptiste. A Primer on the Bayesian Approach to High-Density Single-Molecule Trajectories Analysis. *Biophysical Journal*. 2016, **110**, 1209–1215.
103. BERA, Sudipta; PAUL, Shuvojit; SINGH, Rajesh; GHOSH, Dipanjan; KUNDU, Avijit; BANERJEE, Ayan; ADHIKARI, Ronojoy. Fast Bayesian inference of optical trap stiffness and particle diffusion. *Scientific Reports*. 2017, **7**, 41638.
104. PÉREZ GARCÍA, Laura; DONLUCAS PÉREZ, Jaime; VOLPE, Giorgio; V. ARZOLA, Alejandro; VOLPE, Giovanni. High-performance reconstruction of microscopic force fields from Brownian trajectories. *Nature Communications*. 2018, **9**(1), 5166.
105. WU, Pinyu; HUANG, Rongxin; TISCHER, Christian; JONAS, Alexandr; FLORIN, Ernst-Ludwig. Direct Measurement of the Nonconservative Force Field Generated by Optical Tweezers. *Phys. Rev. Lett.* 2009, **103**, 108101.
106. VOLPE, Giovanni; HELDEN, Laurent; BRETTSCHEIDER, Thomas; WEHR, Jan; BECHINGER, Clemens. Influence of Noise on Force Measurements. *Phys. Rev. Lett.* 2010, **104**, 170602.

107. BRETTSCHEIDER, Thomas; VOLPE, Giovanni; HELDEN, Laurent; WEHR, Jan; BECHINGER, Clemens. Force measurement in the presence of Brownian noise: Equilibrium-distribution method versus drift method. *Phys. Rev. E*. 2011, **83**, 041113.
108. GIESELER, Jan; GOMEZ-SOLANO, Juan Ruben; MAGAZZÙ, Alessandro; CASTILLO, Isaac Pérez; GARCÍA, Laura Pérez; GIRONELLA-TORRENT, Marta; VIADER-GODOY, Xavier; RITORT, Felix; PESCE, Giuseppe; ARZOLA, Alejandro V.; VOLKE-SEPULVEDA, Karen; VOLPE, Giovanni. *Optical Tweezers: A Comprehensive Tutorial from Calibration to Applications*. 2020. Available from arXiv: 2004.05246 [physics.optics].
109. PARK, Haesung; LEBRUN, Thomas W. Parametric Force Analysis for Measurement of Arbitrary Optical Forces on Particles Trapped in Air or Vacuum. *ACS Photonics*. 2015, **2**(10), 1451–1459.
110. RICCI, F.; CUAIRAN, M. T.; CONANGLA, G. P.; SCHELL, A. W.; QUIDANT, R. Accurate Mass Measurement of a Levitated Nanomechanical Resonator for Precision Force-Sensing. *Nano Letters*. 2019, **19**(10).
111. GRØNBECH-JENSEN, Niels; FARAGO, Oded. A simple and effective Verlet-type algorithm for simulating Langevin dynamics. *Molecular Physics*. 2013, **111**(8), 983–991.
112. GRØNBECH-JENSEN, Niels; HAYRE, Natha Robert; FARAGO, Oded. Application of the G-JF discrete-time thermostat for fast and accurate molecular simulations. *Computer Physics Communications*. 2014, **185**(2), 524–527. ISSN 0010-4655.
113. BERG-SØRENSEN, K.; FLYVBJERG, H. Power spectrum analysis for optical tweezers. *Rev. Sci. Instrum.* 2004, **75**, 594–612.
114. LEE, Peter M. *Bayesian Statistics: An Introduction, 4th Edition*. Wiley, 2012.
115. MILLEN, J.; DEESUWAN, T.; BARKER, P.; ANDERS, J. Nanoscale temperature measurements using non-equilibrium Brownian dynamics of a levitated nanosphere. *Nature Nanotech.* 2014, **9**, 425–429.
116. BERRY, M. V.; SHUKLA, Pragma. Physical curl forces: Dipole dynamics near optical vortices. *J. Phys. A*. 2013, **46**(42), 422001.
117. BERRY, M. V.; SHUKLA, Pragma. Curl force dynamics: Symmetries, chaos and constants of motion. *New J. Phys.* 2016, **18**, 063018. ISSN 1367-2630.

## LIST OF PUBLICATIONS AND OTHER OUTPUTS

### Publications related to this thesis

- SVAK, V., BRZOBOHATÝ, O., SILER, M., JÁKL, P., KANKA, J., ZEMÁNEK, P., SIMPSON, S. H.: Transverse spin forces and non-equilibrium particle dynamics in a circularly polarized vacuum optical trap. *Nature Communications*. 2018, **9**(1), 5453. ISSN 2041-1723. (IF=14.919, cited 35×)  
Available from DOI: 10.1038/s41467-018-07866-8
- SVAK, V.; FLAJŠMANOVÁ, J.; CHVÁTAL, L.; ŠILER, M.; JONÁŠ, A.; JEŽEK, J.; SIMPSON, S. H.; ZEMÁNEK, P.; BRZOBOHATÝ, O.: Stochastic dynamics of optically bound matter levitated in vacuum. *Optica*. 2021, **8**(2), 220–229. (IF=11.104, cited 1×)  
Available from DOI: 10.1364/OPTICA.404851

### Other publications

- DONATO, Maria G., BRZOBOHATÝ, Oto, SIMPSON, Stephen H., IRRERA, Alessia, LEONARDI, Antonio A., LO FARO, Maria J., SVAK, VOJTĚCH, MARAGÓ, Onofrio M., ZEMÁNEK, Pavel: Optical Trapping, Optical Binding, and Rotational Dynamics of Silicon Nanowires in Counter-Propagating Beams. *Nano Letters*. 2019, **19**(1), 342-352. (IF=11.189, cited 38×)  
Available from DOI: 10.1021/acs.nanolett.8b03978

### Conference proceedings

- BRZOBOHATÝ, O., DAMKOVÁ, J., SVAK, V., ŠILER, M., JÁKL, P., SIMPSON, S., MARAGÓ, O., DONATO, M. G., FILIP, R., and ZEMÁNEK, P.: Vacuum optomechanics of optically levitated objects. *J. Phys.: Conf. Ser.*, 1461:012199, 2020.  
<https://iopscience.iop.org/article/10.1088/1742-6596/1461/1/012199>
- SVAK, V., ARITA, Y., SIMPSON, S. H., BRZOBOHATÝ, O., ŠILER, M., JÁKL, P., KAŇKA, J., ZEMÁNEK, P. and DHOLAKIA, K.: Non-conservative instabilities in optical vacuum traps. *Proc. SPIE*. 11297:112970F, 2020  
10.1117/12.2545948
- ŠILER, M., FLAJŠMANOVÁ, J., SVAK, V., JÁKL, P., SIMPSON, S., H., FILIP, R., BRZOBOHATÝ, O., ZEMÁNEK, P.: Vacuum optomechanics of optically levitated objects: determination of nonlinear properties of the optical trap. *Proc. SPIE*, 11297:112970I, 2020.  
<https://doi.org/10.1117/12.2546009>

- BRZOBOHATÝ, O., SIMPSON, S., SILER, M., JAKL, P., DAMKOVA, J., SVAK, V., AZOLA, A., VOLKE-SEPULVEDA, K., FILIP, R., and ZEMANEK, P.: Underdamped and overdamped dynamics of objects in nonlinear optical potentials. *Proceedings SPIE*. 2018, 10712.  
10.1117/12.2319285
- DAMKOVÁ, J., CHVÁTAL, L., BRZOBOHATÝ, O., SVAK, V., ŠILER, M., SIMPSON, S., and ZEMÁNEK, P.: Characterizing Particle Pairs Optically Bound in “Tractor Beam”. *Proceedings SPIE*. 2016, 9922.  
10.1117/12.2237572

### Conference contributions

- WE Heraeus Seminar on Levitated Optomechanics, Bonn, Germany. Poster: Optical binding of microparticles levitated in counter-propagating beams optical trap in vacuum. 2019
- Quantum Engineering of Levitated Systems, Benasque, Spain. Talk: Orbital motion from optical spin: the extraordinary momentum of circularly polarised light beams. 2018
- CPS, Lednice, Czech Republic. Talk: Orbital motion from optical spin: the extraordinary momentum of circularly polarised light beams. 2018
- ICN+T, Brno, Czech Republic. Talk: Optical spin driven dynamics of microparticle optically trapped in vacuum. 2018
- Recent trends, Skalský dvůr, Czech Republic. Talk: Orbital motion from optical spin: the extraordinary momentum of circularly polarised light beams. 2018
- Laser57, Třešť, Czech Republic. Poster: Optical spin driven dynamics of microparticle optically trapped in vacuum. 2017
- Quantum Nanophotonics, Ascona, Switzerland. Poster: Optical spin driven dynamics of microparticle optically trapped in vacuum. 2017
- SCP, Jasná, Slovakia. Talk: Optical trapping of a nanoparticle in air. 2016

## MY CONTRIBUTIONS TO THE PRESENTED WORK

### **Transverse spin forces and non-equilibrium particle dynamics in a circularly polarized vacuum optical trap**

- design, building and alignment of the experimental setup
- development of control software in LabView
- performing all measurement
- data processing - tracking particles motion from video, part of analysis of trajectories (PSD, variances)
- discussion on the results together with other group members, participation on manuscript preparation

### **Stochastic dynamics of optically bound matter levitated in vacuum**

- design, building and alignment of the first experimental setup
- first preliminary experiments with two, three and four optically bound particles
- measurement of particle collision
- data processing - tracking particles motion from video, part of analysis of trajectories (PSD, variances)
- participation in development of the theoretical models
- discussion on the results together with other group members

### **Force estimation from stochastic trajectory**

- extension of the original 1D idea into functional 2D method
- testing of the additive position noise effect
- original idea for correction of estimated force profile corrupted by additive position noise
- development of Matlab scripts performing the method
- testing the method on simulated and experimental data